National Library of Australia
Cataloguing-in-Publication entry

Green, Martin A.

Includes index.
ISBN 0 7334 0994 6

1. Solar cells. 2. Photovoltaic power generation.
I. University of New South Wales II. Title

All rights reserved. No part of this book may be reproduced in any form or by any means without permission from the author.

Publisher: Centre for Photovoltaic Devices and Systems
University of New South Wales
Sydney, N.S.W. 2052

March, 1995

Printed by Bridge Printery Pty. Ltd., 29-35 Dunning Avenue, Rosebery, N.S.W., 2018

SILICON SOLAR CELLS
Advanced Principles & Practice

Martin A. Green

HANWHA 1045

To Judy, Brie and Morgan

TABLE OF CONTENTS

Chapter 1: INTRODUCTION 1

Chapter 2: CRYSTAL STRUCTURE AND ENERGY BANDS 4

2.1 INTRODUCTION 4
2.2 CRYSTAL STRUCTURE 4
2.3 SCHRÖDINGER WAVE EQUATION 6
2.4 RECIPROCAL LATTICE 7
2.5 ENERGY BANDS 10
2.6 DENSITY OF STATES & OCCUPATION PROBABILITY 13
2.7 MOMENTUM AND EFFECTIVE MASS 16

Chapter 3 PHONONS, PHOTONS & EXCITONS 21

3.1 INTRODUCTION 21
3.2 PHONONS 22
3.3 PHOTONS 24
3.4 RAMAN SCATTERING 25
3.5 EXCITONS 28

Chapter 4 OPTICAL PROPERTIES 32

4.1 INTRODUCTION 32
4.2 LIGHT ABSORPTION IN PURE SILICON 32
4.2.1 General 32
4.2.2 Phonon-Assisted Absorption 34
4.2.3 Absorption Edge 37
4.2.4 Wavelength Modulation Spectroscopy 39
4.2.5 Multiple Phonon Processes 40
4.2.6 Direct Absorption 43
4.2.7 Free Carrier and Lattice Absorption 46
4.3 REFRACTIVE INDEX 48
4.4 TEMPERATURE DEPENDENCIES 49
4.5 HEAVILY DOPED SILICON 51
4.6 OTHER ABSORPTION PROCESSES 54

Chapter 5 GENERATION, RECOMBINATION, CARRIER TRANSPORT 57

5.1 GENERAL EQUATIONS 57
5.2 GENERATION 59
5.3 RECOMBINATION 61
5.3.1 General 61
5.3.2 Radiative Recombination 61
5.3.3 Band-to-Band Auger Recombination 63
5.3.4 Recombination Through Defect Levels 66
5.4 CARRIER TRANSPORT 72
5.4.1 Drift and Diffusion 72
5.4.2 Boltzmann Transport Equation 73
5.4.3 Majority and Minority Carrier 75
5.4.4 High Injection Mobilities 80
5.4.5 Excitonic Transport 81
5.4.6 Heavy Doping 83

Chapter 6 LIGHT TRAPPING 92

6.1 INTRODUCTION 92
6.2 RANDOMIZING SCHEMES 93
6.3 GEOMETRICAL LIGHT TRAPPING 97
6.3.1 Introduction 97
6.3.2 Two Dimensional Geometries 98
6.3.3 Three Dimensional Geometries 100
6.4 Experimental Results 106
6.5 CONCENTRATED LIGHT 109
6.6 Light Trapping 111

Chapter 7 FUNDAMENTAL EFFICIENCY LIMITS 117

7.1 INTRODUCTION 117
7.2 PHOTON-GENERATED CURRENT LIMITS 118
7.3 OPEN-CIRCUIT VOLTAGE LIMITS 122
7.3.1 General 122
7.3.2 Low Injection Conditions 122
7.3.3 Narrow Base, High Injection Limits 127
7.4 FILL FACTOR 130
7.5 EFFICIENCY LIMITS 131
7.5.1 Non-Concentrating Cells 131
7.5.2 Concentrating Cells 132
7.6 MATERIAL REQUIREMENTS 135
7.7 POTENTIAL FOR EXCEEDING LIMITS 140

Chapter 8 SUB-THRESHOLD CARRIER GENERATION 145

8.1 INTRODUCTION 145
8.2 GERMANIUM ALLOYS 147
8.3 IMPURITY PHOTOVOLTAIC EFFECT 148
8.3.1 Introduction 148
8.3.2 Optical Capture Cross Sections 149
8.3.3 Design Philosophies 150
8.3.4 Indium Case Study 153
8.3.5 Other Impurities 157
8.3.6 Detailed Balance 158
8.4 OTHER SUGGESTED SCHEMES 160
8.4.1 Implanted Defect Layer 160
8.4.2 Delta Doping 161
8.5 TANDEM CELLS 162

Chapter 9 SURFACE, CONTACT AND BULK PROPERTIES 166

9.1 INTRODUCTION 166
9.2 SURFACE RECOMBINATION 166
9.2.1 Interface States and Oxide Traps 166
9.3 RECOMBINATION AT INTERFACE STATES 173
9.3.1 Independent, Discrete Interface States 173
9.3.2 Independent, Continuous States 173
9.3.3 Equal Capture Cross-Sections 174
9.3.4 Constant Capture Cross-Sections 174
9.3.5 Experimental Interface Densities and Capture Cross-Sections 175
9.4 CONTACT RECOMBINATION 181
9.5 BULK RECOMBINATION 186
9.6 GETTERING 192
9.7 DEFECT PASSIVATION 195

Chapter 10 EVOLUTION OF SILICON SOLAR CELLS 201

10.1 INTRODUCTION 201
10.2 EARLY SILICON CELLS 202

10.3 CONVENTIONAL SPACE CELLS....205
10.4 BACK SURFACE FIELD....207
10.5 VIOLET CELLS....207
10.6 BLACK CELLS....209
10.7 OXIDE SURFACE PASSIVATION....212
10.8 CONTACT PASSIVATION....213
10.9 TOP SURFACE PASSIVATED CELLS....215
10.10 TOP AND REAR PASSIVATED CELLS....218
10.11 PERL CELL DESIGN....221
10.11.1 Optical features....221
10.11.2 Electronic Features....223
10.11.2.1 Bulk Recombination....223
10.11.2.2 Surface Recombination....224
10.11.2.3 Contact Area Recombination....226
10.11.2.4 Present Recombination Relativities....227
10.12 SUMMARY....227

Chapter 11 SCREEN-PRINTED AND BURIED CONTACT CELLS....234

11.1 INTRODUCTION....234
11.2 SCREEN-PRINTED CELLS....235
11.2.1 Structure....235
11.2.2 Typical Performance....237
11.2.3 Improved Technology....238
11.3 BURIED CONTACT SOLAR CELLS....239
11.3.1 Structure....239
11.3.2 Performance Analysis....241
11.3.3 Production Experience....242
11.3.4 Future Improvement....243

Chapter 12 HIGH PERFORMANCE CONCENTRATOR SOLAR CELLS....249

12.1 INTRODUCTION....249
12.2 CONVENTIONAL CELLS....250
12.2.1 Low Cost Approaches....250
12.2.2 High Efficiency Space Technology Cells....252
12.2.3 PESC and PERL Cells....253
12.2.4 V-Groove Silicon Cell....254
12.3 BACK SURFACE CONTACT CELLS....255
12.3.1 Interdigitated Back-Contact Cell....255
12.3.2 Front-Surface Field and Tandem Cells....257
12.3.3 Double-Sided and Polka-Dot Cells....258
12.4 VERTICAL JUNCTION CELLS....259
12.5 POINT CONTACT SOLAR CELL....260
12.5.1 Structure....260
12.5.2 Recombination Components....262
12.5.3 Photocurrent Collection....263
12.5.4 Experimental Results....264
12.5.5 Point Contact Cell Stability....268
12.5.6 Recent Developments....268
12.6 SUMMARY....269

Chapter 13 MULTICRYSTALLINE AND RIBBON SILICON....273

13.1 INTRODUCTION....273
13.2 HYDROGEN PASSIVATION....275
13.3 PHOSPHORUS TREATMENT....276
13.4 OTHER PASSIVATION APPROACHES....281
13.5 TEXTURING....281
13.6 ADVANCED CELL STRUCTURES....282

Chapter 14 THIN FILM POLYCRYSTALLINE AND MULTILAYER CELLS....288

14.1 INTRODUCTION....288
14.2 GRAIN BOUNDARIES....289
14.2.1 Physical Structure....289
14.2.2 Electronic Properties....291
14.2.3 Resistive Effects....294
14.2.4 Recombination Properties....296
14.2.4.1 Bulk Regions....296
14.2.4.2 Horizontal Grain Boundary in Depletion Region....303
14.2.4.3 Vertical Grain Boundaries....308
14.3 INTRAGRAIN PROPERTIES....311
14.4 SINGLE JUNCTION CELLS....314
14.5 MULTILAYER CELLS....318
14.6 SUMMARY....322

Chapter 15 CONCLUSION....326

Appendix A GREEK ALPHABET 329

Appendix B PHYSICAL CONSTANTS 330

Appendix C SPECTRAL DATA 331

Appendix D OPTICAL PROPERTIES OF SILICON 333

Appendix E QUASI-FERMI LEVELS 337

E.1 INTRODUCTION 337
E.2 THERMAL EQUILIBRIUM 337
E.3 NON-EQUILIBRIUM 338
E.4 INTERFACES 339
E.5 NON-EQUILIBRIUM P-N JUNCTION 340
E.6 USE OF QUASI-FERMI LEVELS 341

Appendix F REFLECTION CONTROL 345

F.1 ANTIREFLECTION COATINGS 345
F.2 SURFACE TEXTURING 345
F.2.1 Historical and Technological Perspective 345
F..2.2 Theory of Reflection Control by Texturing 347
F.2.2.A Feature Size 347
F.2.2.B Macroscopic Features 348
F.2.2.C Microscopic Features 353

Appendix G INFRARED SPECTRAL RESPONSE 357

INDEX 364

PREFACE

"In the history of technological development, there are past examples where an apparently mature technology blossoms into its full state of development only when facing the challenge from a newer technology. This appears to be happening in the case of bulk silicon solar cells. Since the early 1980's when thin film solar cell products first became available commercially, there have been quite remarkable improvements in bulk silicon cell performance. The exciting fact is that, despite the magnitude of recent improvements, it has become increasingly clear that there is plenty of potential for further increase".

So began the preface for the author's earlier research monograph "***High Efficiency Silicon Solar Cells***" which was stimulated by the first demonstration of 20% cell efficiency and the recognition of the potential for even further improvement. A decade further on, about half this potential has been realized in practice and some of the ideas , then at a laboratory stage, are now appearing in production and in field installations.

With the demonstration of viable production technology for obtaining 20% bulk cell efficiency, and the imminent explosion of interest in thin film and polycrystalline silicon cells, it seems appropriate to once again take stock of what we have learned and where we are heading. The present text includes some of the basic material incorporated into the earlier monograph previously mentioned, but reworked in a style which may make it also suitable as a graduate level textbook. It assumes a basic grounding in solar cell device operation, at the level of the author's text, "***Solar Cells: Operating Principals, Technology and Systems Application***" (also available from the author) as well as some familiarity with semiconductor physics at a slightly more advanced level.

It is a pleasure to acknowledge the contributions to many of the developments described within the book of past and present members of the Centre for Photovoltaic Devices and Systems. I would also like to thank those taking the graduate course ELEC9508 at the University of New South Wales during 1994, who provided feedback on an earlier draft of the book, and also Richard Corkish, Steve Robinson, Frans Saris and David Thorp for their detailed suggestions. I also thank Jenny Hansen for her untiring assistance in producing this book and its figures. Finally, I would also like to thank the authors and copyright holders who gave permission to reprint many of the figures liberally scattered through the text, including the Royal Radar Establishment for permission to reprint Figure 4.4 (Crown copyright material reproduced with the permission of the Controller of HMSO).

Martin A. Green
Centre for Photovoltaic Devices and Systems
University of New South Wales
Sydney, NSW, 2052
March, 1995

Chapter
1

INTRODUCTION

Over the last decade, there has been rapid improvement in silicon laboratory solar cell efficiency as shown in Fig. 1.1. Maximum demonstrated efficiencies have increased from about 17% in 1983 to above 24% in 1995.

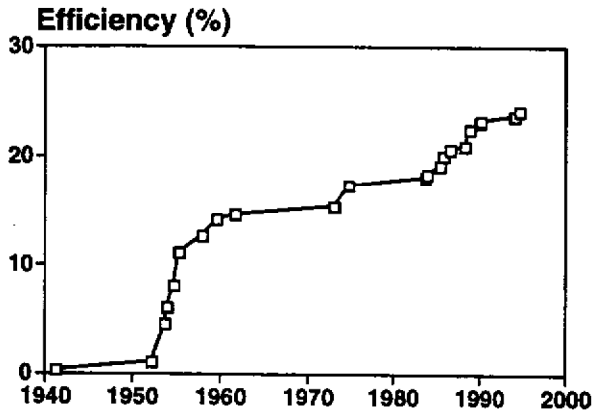


Figure 1.1: Evolution of Silicon Laboratory Cell Efficiency.

Importantly, some of these improvements are filtering through to commercial practice. For the 1993 World Solar Challenge, the solar car race across Australia from Darwin to Adelaide, several suppliers were able to provide silicon cells in kilowatt quantities of above 19% efficiency with two groups able to supply cells above 21% [1.1]. At

the same time, one company had produced close to a megawatt of large area cells of efficiency comparable to the best laboratory cells of only a decade earlier [1.2].

Without any major technical breakthroughs, the cost of silicon cells has also reduced quite markedly. Crystalline silicon technology has already reached all that was expected of it in the ambitious program of the US Government in the 1970's [1.3], only it has taken twice as long as originally planned [1.4]. The important point is that these cost reductions have not been driven by new technology, but by the economies of scale and the learning experience associated with an expanding industry [1.5]. Most of the laboratory improvements over the last decade have not yet made commercial impact.

An important aspect of the original thinking about photovoltaic development [1.3] was that, once benefits from improving crystalline silicon technology had been exhausted, there would be a second period of rapid cost reduction arising from a change from crystalline silicon to a thin film technology.

At the present time, it seems as if there are several ways in which this second phase of accelerated cost reduction could be realized. One might be just by the incorporation of the lessons learned in the laboratory in silicon cell design over the last decade into commercial practice, combined with increased investment in production technology. In this scenario, a 20% efficient photovoltaic panel based on a low-cost, high-efficiency sequence, such as the buried contact sequence described in Chapter 11, might be the final product, particularly if combined with stationary refractive concentrators to reduce the required cell area. Another possibility would be that this decrease in cost might come about by successful commercialization of a thin film technology. At the present point in time, thin film polycrystalline silicon appears one of the stronger candidates for the long term. Of other candidates, hydrogenated amorphous silicon cell development has not progressed at the rate anticipated in the mid-1980's. Casting a wider net, the photovoltaic community could be doing itself a disservice by promoting, as its ultimate solution, a technology such as cadmium telluride which generates legitimate environmental concerns. Similarly, the community could be accused of a certain lack of ambition in promoting copper indium gallium selenide as this final solution. given the limited contribution to global energy requirements able to be made by a technology dependent upon limited resources of indium and gallium [1.6].

Of technologies already identified, bulk silicon and thin film polycrystalline silicon cells remain key contenders for providing this long-term solution. By consolidating recent developments and outlining possible areas for future activity, the present book seeks to contribute to the development of these cells. The book is split roughly into two sections. The first treats the material parameters and basic mechanisms important in silicon photovoltaic energy conversion. It includes a thorough discussion of absorption processes in silicon, particularly sub-bandgap processes, and a detailed treatment of light trapping effects which will make sub-bandgap absorption more important in future generations of cells. Efficiency limits upon cell performance are discussed, as are the material properties required to reach these limits. The second half of the book deals with device structures. It includes an historical review of the evolution of cell design, as well as a detailed treatment of the device structures appropriate to the different areas of present and future interest: crystalline cells, concentrating cells, cells fabricated on ribbon and multicrystalline substrates, and thin film silicon cells, including the very promising multilayer devices [1.7].

REFERENCES

1.1 M.A. Green, "World Solar Challenge 1993: The Trans-Australian Solar Car Race", Progress in Photovoltaics, Vol. 2, pp. 73-79, 1994.

1.2 PV Insiders Report, June, 1994.

1.3 Final Report, Flat Plate Solar Array Project, Jet Propulsion Laboratory, E. Christensen (ed.,), October, 1985.

1.4 G. Landis, "Coal and Solar Futures", Progress in Photovoltaics, Vol. 1, pp. 319-320, 1993.

1.5 K.W. Mitchell, "The Reformation of CZ Si Photovoltaics", Conf. Record, First World Conference on Photovoltaic Energy Conversion, Hawaii, December, 1994.

1.6 M.A. Green, "Silicon Solar Cells: The Ultimate PV Solution?", Progress in Photovoltaics, Vol. 2, pp. 87-94, 1994.

1.7 S.R. Wenham, M.A. Green, S. Edmiston, P. Campbell, L. Koschier, C.B. Honsberg, A.B. Sproul, D. Thorpe, Z. Shi and G. Heiser, "Limits to the Efficiency of Silicon Multilayer Thin Film Solar Cells", Conf. Record, First World Conference on Photovoltaic Energy Conversion, Hawaii, December, 1994.

Chapter

2

CRYSTAL STRUCTURE AND ENERGY BANDS

2.1 INTRODUCTION

The optical and electronic properties of silicon important in solar cell operation are well explained by the electronic band theory of solids. This theory models a solid as an ideal periodic crystal with immobile atomic nuclei. The effects of vibrations of these nuclei about their equilibrium positions are decoupled by treatment as perturbations. The "many-electron" problem presented by an actual solid is reduced to the much simpler "one-electron" problem by describing the effect upon a single electron of all other electrons by an average periodic field. This chapter reviews this band theory by discussing the energy band structure resulting from silicon's crystalline nature.

2.2 CRYSTAL STRUCTURE

In the silicon lattice (Fig. 2.1), each silicon atom is covalently bonded to its four nearest neighbours. The angle between the bonds is 109° 28'. The lattice is equivalent to two interleaved face-centred cubic lattices. One is defined by the cube corresponding to the extremities of the unit cell (Fig. 2.1), while the second is displaced by one-quarter of the distance along the cube diagonal.

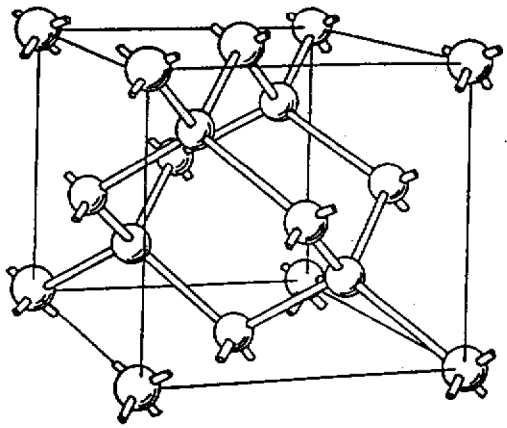


Figure 2.1: Lattice Structure of Silicon.

The **primitive cell** and **basis vectors**, $\boldsymbol{a}_i$, of the face-centred cubic lattice are shown in Fig. 2.2. The atoms on the corners of the primitive cell contribute a total of one atom to the cell. This cell remains a primitive cell of the silicon lattice, but has an extra atom located within it. Hence, the silicon lattice is technically a ***complex*** lattice [2.1]. It shares many of the symmetries of the face-centred cubic lattice, with some symmetries of the latter destroyed by the extra atom in the primitive cell.

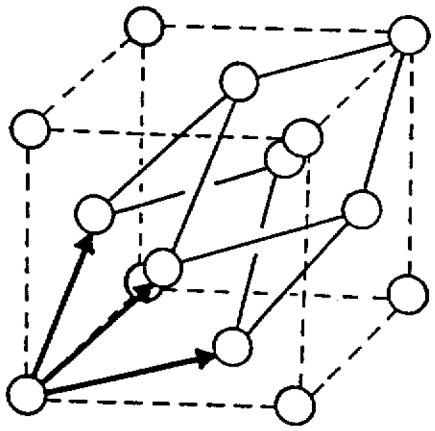


Figure 2.2: The Primitive Cell and the Basis Vectors of the Face-Centred Cubic Space Lattice

In the case of silicon, rather than working with the primitive cell shown in Fig. 2.2, it is more usual to work with the large cubic unit cell apparent in both Figs. 2.1 and 2.2. This contains a total of 8 silicon atoms. Use of this unit cell allows an orthogonal set of basis vectors to be chosen in the directions along the edges of the cube. The lattice constant, a, is the length of the side of the cube shown in Fig. 2.1.

2.3 SCHRÖDINGER WAVE EQUATION

Electron properties in a lattice of atoms are described by wave functions, ψ, which are solutions to the time-independent Schrödinger wave equation [2.2]:

$$-\frac{\hbar^2}{2m_0}\nabla^2\psi + V(\mathbf{r})\psi = E\psi \qquad (2.1)$$

where $\hbar$ is the reduced Planck constant, m_0 is the free electron mass, $\mathbf{r}$ is position within the lattice, $V(\mathbf{r})$ is the periodic crystal potential including the contributions from both lattice atoms and the other electrons in the crystal, and E is the electron energy.

"Where did we get that from? Nowhere. It is not possible to derive it from anything you know. It came out of the mind of Schrödinger" - Richard Feynman [2.3].

C.T. Sah [2.4], however, does a good job of explaining how the Schrödinger equation is a logical synthesis of two classical laws - the conservation of energy and Newton's force law, plus two quantum postulates, the Planck and de Broglie hypotheses. (Sah also gives an elementary treatment of band theory at a good level relative to that of Ref. [2.5]).

Techniques for solving Eq. (2.1) are now well developed. Due to the periodicity of $V(\mathbf{r})$, the solutions can be expressed in terms of Bloch functions:

$$\psi_n(\mathbf{k}, \mathbf{r}) = u_n(\mathbf{k}, \mathbf{r}) \exp(i\,\mathbf{k}.\mathbf{r}) \qquad (2.2)$$

where the wave vector $\mathbf{k}$ is introduced as a quantum mechanical indexing parameter, an extra variable of use in ordering the solutions

of Eq. (2.1). Equation (2.2) represents a plane wave, $\exp(i\mathbf{k}.\mathbf{r})$, modulated by the function, $u_n(\mathbf{k},\mathbf{r})$, which has the periodicity of the crystal lattice. For a crystal incorporating a large number of lattice sites, any value chosen for $\mathbf{k}$ will give allowed solutions of this form. For any chosen $\mathbf{k}$ value, there is an infinite number of possible wave functions of the form of Eq. (2.2), where each wave function corresponds to an allowed energy level, $E_n(\mathbf{k})$. The energy levels corresponding to different values of $\mathbf{k}$ and the same value of n constitute the n*th* energy band. Since $E_n(\mathbf{k})$ varies periodically in $\mathbf{k}$, with a periodicity determined by the lattice structure, all distinct values of $E_n(\mathbf{k})$ can be obtained by restricting $\mathbf{k}$ to values in the range:

$$-\pi < \mathbf{k}.\mathbf{a}_i < \pi \qquad (2.3)$$

where the $\mathbf{a}_i$ are the basis vectors of the primitive lattice.

2.4 RECIPROCAL LATTICE

Equation (2.3) suggests the use of a ***reciprocal lattice*** to describe equivalent values of $\mathbf{k}$.

In a general crystal lattice, any lattice site can be defined by the set of vectors:

$$\mathbf{R} = n_1\mathbf{a}_1 + n_2\mathbf{a}_2 + n_3\mathbf{a}_3 \qquad (2.4)$$

where the n_i are integers, and the $\mathbf{a}_i$ are the basis vectors of the primitive unit cell.

A set of reciprocal lattice vectors, $\mathbf{G}$, can be defined such that:

$$\mathbf{G}.\mathbf{R} = 2m\pi \qquad (2.5)$$

where m is an integer and where:

$$\mathbf{G} = g_1\mathbf{b}_1 + g_2\mathbf{b}_2 + g_3\mathbf{b}_3 \qquad (2.6)$$

The g_i are integers and $\mathbf{b}_i$ are the basis vectors of the reciprocal lattice given by:

$$\mathbf{b}_i = 2\pi\,(\mathbf{a}_j \times \mathbf{a}_k)/\Omega_0 \qquad (2.7)$$

where $i \neq j \neq k$ and Ω_0 is the volume in real space of the primitive unit cell of the crystal lattice, given by:

$$\Omega_o = \boldsymbol{a}_i \cdot (\boldsymbol{a}_j \times \boldsymbol{a}_k) \qquad (2.8)$$

The "volume" of the unit cell in reciprocal space formed by the basis vectors $\boldsymbol{b}_i$ is given by the same formula as Eq. (2.8) with $\boldsymbol{a}_m$ replaced by $\boldsymbol{b}_m$. This "volume" has the units of (length)$^{-3}$ and equals $(2\pi)^3/\Omega_o$. Applying Eq. (2.7) shows that the reciprocal lattice of a face-centred cubic lattice with lattice constant, a, is a body-centred cubic lattice with lattice constant, $4\pi/a$ [2.6].

Distinct values of $E_n(\boldsymbol{k})$ can be obtained by restricting $\boldsymbol{k}$ to the ***first Brillouin zone*** of the reciprocal lattice. This zone is defined as that space surrounding a lattice site ***in the reciprocal lattice*** which contains all points lying closer to this lattice site than to any other such lattice site. It can be simply constructed from planes which perpendicularly bisect the lines joining the selected lattice site to all other lattice sites. This construction is shown in Fig. 2.3 for the case of a body centred cubic reciprocal lattice. The smallest volume formed by these intersecting planes is the first Brillouin zone; commonly referred to simply as the Brillouin zone.

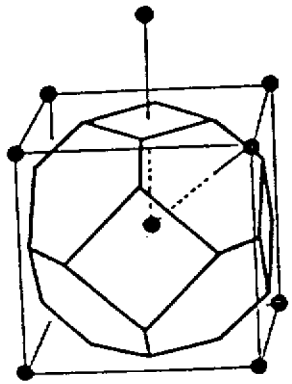


Figure 2.3: Construction of the truncated octahedron corresponding to the first Brillouin zone of the body centred cubic reciprocal lattice, showing its relationship to the cubic unit cell of this lattice.

The Brillouin zone for the silicon lattice is identical to that of the face-centred cubic lattice. Shown in Fig. 2.4 are important lines and points of symmetry within this zone. Very general conclusions about the properties arising from such symmetry can be made using ***group theory***, a branch of mathematics developed in the early 19th century [2.7]. Lines and points of symmetry are labelled according to a standard notation which identifies the type of symmetry of the particular point or line [2.8,2.9]. Some examples are the centre of the zone at $\Gamma(0,0,0)$, the $<111>$ axes (Λ), and their intersections with the zone edge at $L(\pi/a,\pi/a,\pi/a)$ and equivalent points, the $<100>$ axes (Δ) and their zone edge intersections $[X = (0,2\pi/a,0)]$ and equivalent points, and the $<110>$ axes (Σ) and their intersections $[K = (3\pi/2a,3\pi/2a,0)]$ and equivalent points.

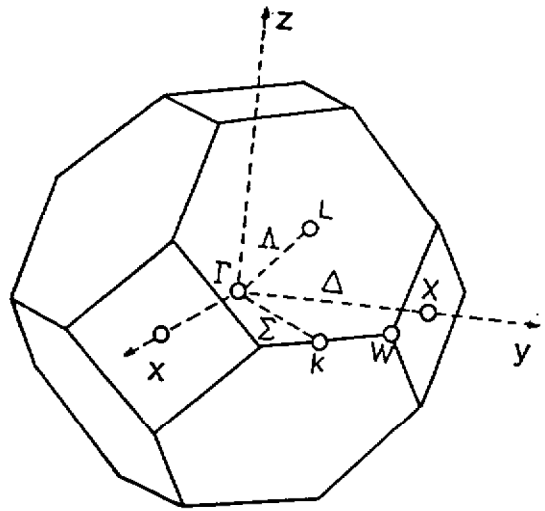


Figure 2.4: The First Brillouin Zone of the Reciprocal Lattice for Silicon.

At these points and along these lines, a great deal of information about the bands corresponding to the energies, $E_n(\boldsymbol{k})$, can be deduced directly from the symmetries involved. Due to this, and to the difficulty in graphically representing the variation of $E_n(\boldsymbol{k})$ as a function of the three-dimensional variable, $\boldsymbol{k}$, energy band relationship are generally shown only at the particular values of $\boldsymbol{k}$ which correspond to these symmetry points and lines (see Fig. 2.5(b)).

Various techniques exist for calculating the $E_n(\mathbf{k})$ relationships for real crystals such as silicon [2.10]. Due to the difficulties in quantitatively describing the periodic potentials affecting electrons in the crystal, these calculations generally involve parameters whose values can be adjusted to give a good fit between theory and experiment at selected points. By combining theory and experiment in this way, a good qualitative picture of the energy band structure of silicon has emerged, although quantitative uncertainties remain.

2.5 ENERGY BANDS

The band structure of silicon, as calculated using the empirical pseudopotential method [2.11], is presented in the normal manner in Fig. 2.5(b). Bands of allowed energy levels, $E_n(\mathbf{k})$, for values of $\mathbf{k}$ lying along lines of symmetry of Fig. 2.4 are shown. The zero of energy is arbitrarily chosen to correspond to the highest valence band energy. Hence, negative energies correspond to valence band states; positive energies to conduction band states. Both the conduction and the valence band are made up of several bands (branches of the $E_n(\mathbf{k})$ relationship) which are coincident for some symmetry lines and which cross (overlap) along others. The labelling of these bands and energy levels at the points of high symmetry corresponds to that of Fig. 2.4.

The point Γ at the centre of the Brillouin zone ($\mathbf{k} = 0$) is the point of highest symmetry, and the band structure displays several interesting features at this point. The valence band has its lowest energy level labelled Γ_1. The next highest energy for this value of $\mathbf{k}$ is the "triply degenerate" state (neglecting spin orbit splitting, Section 2.6) labelled Γ'_{25}. This state corresponds to the maximum valence band energy. Moving away from Γ towards points of lower symmetry, this degeneracy disappears, as demonstrated for $\mathbf{k}$ values along the Σ symmetry line. The four separate bands which make up the valence band are apparent in this direction. However, in the Λ and Δ directions, the uppermost band in each case (Λ_3 and Δ_5, respectively) remains doubly degenerate.

Returning to the Γ point, the next highest energy state is Γ_{15}, also triply degenerate. The energy difference, $\Gamma_{15} - \Gamma'_{25}$, gives the ***direct bandgap*** of silicon, with an experimentally determined value of 3.4 eV. Moving away from Γ in both the <100> (Δ) and <111> (Λ) directions in $\mathbf{k}$ space, the conduction band energy decreases. The lowest energy is reached 85% of the way towards the zone boundary along Δ. The energy above the valence band edge at this point is the minimum bandgap, the ***indirect bandgap*** of silicon. It plays a major role in determining electronic and photovoltaic properties. As apparent in Fig. 2.5(b), the energy levels are not appreciably higher than this minimum at the equivalent points, U and K, on the zone edge. A local minimum also occurs at the zone edge in the <111> direction. The bandgap corresponding to this minimum is frequently referred to as the ***second indirect bandgap.***

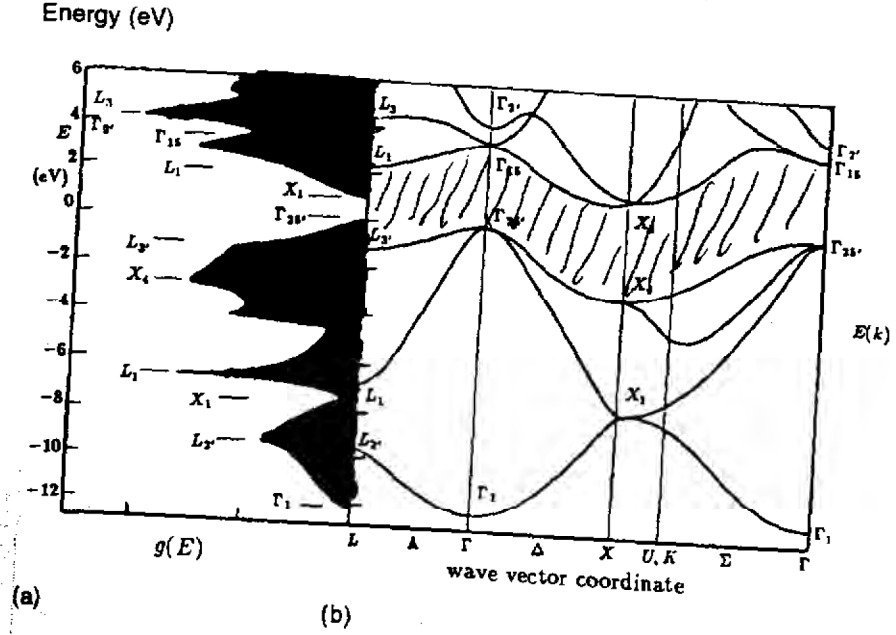


Figure 2.5: The energy band structure for silicon is shown in (b) as calculated using an empirical non-local pseudopotential scheme with the associated density of electron states $g(E)$ shown in (a) (after Chelikowsky and Cohen [2.11] and Böer [2.12]).

Returning again to the centre of the Brillouin zone (Γ), the second-lowest energy in the conduction band at this point corresponds to the non-degenerate, Γ'_2 state. The next-lowest state is several eV higher and is unlikely to influence photovoltaic properties.

A three-dimensional sketch of the results of the same calculation is also shown in Fig. 2.6(b). This shows the E-$\mathbf{k}$ (energy-momentum) relationship over a plane of high symmetry, rather than along individual lines. This plane is indicated in the Brillouin zone sketch of Fig. 2.6(a), which is rotated from that of Fig. 2.4. It contains all the symmetry points Γ, X, L, U and K of Fig. 2.5(b) and also all the symmetry lines including Δ, Λ and Σ, but shows how the relationships along these lines join together.

Note that, from Fig. 2.6(b), the valence and conduction bands are parallel over most of this plane except close to the Σ line connecting Γ to K.

Imagine a plane of constant energy intersecting the surfaces. of Fig. 2.6(b). For example, a plane of energy just above the conduction band minima near the X points would intersect the uppermost surface in ellipses near these minima. These ellipses could be transferred to Fig. 2.6(a). Repeating this exercise for other planes in the Brillouin zone would generate, in Fig. 2.6(a), six equivalent ellipsoidal constant energy surfaces near the six equivalent X points as shown in Fig. 2.7.

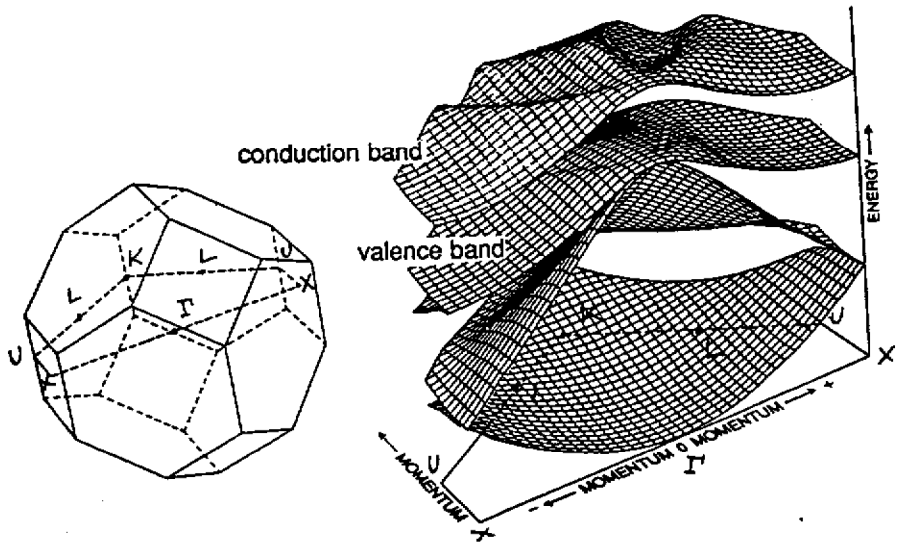


Figure 2.6: (a) Plane of high symmetry within Brillouin zone: (b) E-$\mathbf{k}$ relationships for $\mathbf{k}$ values lying on this plane.

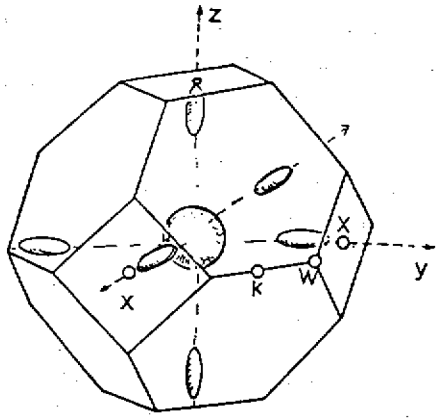


Figure 2.7: Constant energy surfaces within the Brillouin for an energy just above the conduction band minima (ellipsoids) and just below the valance band maximum (sphere).

For energies just below the uppermost valence band, the constant energy intersections near Γ will initially be circular but will become distorted to more closely resemble squares for larger energy departures. Constant energy surfaces in Fig. 2.6(a) correspondingly change from a generally spherical shape near the zone centre as also shown in Fig. 2.7, to a generally cubic shape as the energy below the valence band edge increases.

The calculations of Fig. 2.5 and Fig. 2.6 involve semi-empirically fitting predictions to experimental data at points where there is a high level of confidence in the latter. At points remote from those fitted, the calculated results for the energy levels are accurate to within about 0.5 eV [2.13].

2.6 DENSITY OF STATES & OCCUPATION PROBABILITY

Since electrons are ***fermions*** (quasiparticles with half integral "spin" [2.1]), the probability of occupation of allowed states, $f(E)$, is determined by Fermi-Dirac statistics [2.1]:

$$f(E) = \frac{1}{\exp\left[(E - E_f)/kT\right] + 1} \qquad (2.9)$$

where E_f is the Fermi level and kT is the ***thermal energy*** (which has a value of 25.85 meV at 300K). Since E_f generally lies in the bandgap away from the band edges by more than the thermal energy, this function (or its difference from unity) often can be replaced by a rapidly decaying exponential for energies lying within the bands.

To be able to make use of this function to calculate the number of electrons within each band, the densities of allowed states for electrons as a function of electron energy must be known.

These densities of states can be calculated from very general principles. For a large number of lattice atoms (approaching infinity), it was noted earlier that the wave-vector $\boldsymbol{k}$ could have any chosen value. For a finite number of lattice atoms, however, boundary conditions at the crystal extremities determine what values of $\boldsymbol{k}$ are allowed. It would seem reasonable that, as the crystal size increases, the precise form of the boundary conditions should have a decreasing influence on the internal properties of the crystal.

For mathematical convenience, cyclic boundary conditions are chosen whereby wave functions repeat themselves at the opposite edges of the volume being considered. From Eq. (2.2), this means that:

$$\exp(i\boldsymbol{k} \cdot N_i\boldsymbol{a}_i) = 1 \qquad (2.10)$$

or,

$$\boldsymbol{k} \cdot \boldsymbol{a}_i = 2\pi m/N_i \ (m = 0, \pm1, \pm2, \ldots) \qquad (2.11)$$

where $\boldsymbol{a}_i$ is a basis vector of the primitive cell and N_i is the number of atoms traversed along the direction of this vector.

It can be seen that only discrete values of $\boldsymbol{k}$ are allowed, distributed in a uniform pattern through $\boldsymbol{k}$ space, although the allowed values approach a continuum as the number of atoms in the volume becomes large. By comparing with Eq. 2.3, it can be seen that the total number of allowed $\boldsymbol{k}$ values within the Brillouin zone equals the product $N_1N_2N_3$. There is therefore one distinct value of $\boldsymbol{k}$ within the Brillouin zone for each primitive unit cell within the crystal volume. The "volume" of the Brillouin zone equals $(2\pi)^3/\Omega_0$ where Ω_0 is the volume of the primitive unit cell. This gives the number of allowed

states per unit "volume" within the Brillouin zone as $V/(2\pi)^3$ where V is the crystal volume.

The number of allowed states up to a certain energy can therefore be found merely by finding the volume contained within the constant energy surfaces in $\boldsymbol{k}$ space and multiplying by $V/(2\pi)^3$. To find the ***incremental*** density of states per unit energy, the volume between two constant energy surfaces drawn for two energies close to each other has to be found. Mathematically:

$$g(E) = \frac{2}{(2\pi)^3} \oint \frac{dS_E}{|\nabla_k E|} \qquad (2.12)$$

where $g(E)$ is the density of states per unit energy and per unit volume of the crystal and the integral is conducted over the surface, S_E, of the constant energy surface of energy E. The factor of 2 is introduced since each state may be occupied by two electrons, each of opposite spin.

This calculation becomes trivial for simple constant energy surfaces such as in Fig. 2.7. For the spherical constant energy surfaces near the valence band edge, the surface area S_E equals $4\pi k^2$ and symmetry gives:

$$g(E) = \frac{2}{(2\pi)^3} \times 4\pi k^2 / |dE/dk| \qquad (2.13)$$

The E-$\boldsymbol{k}$ relationship in this region near the valence band edge can be approximated by the isotropic effective mass approximation:

$$E = \hbar^2 k^2 / 2m^* \qquad (2.14)$$

where E is energy below the valence band edge, giving:

$$|dE/dk| = \hbar^2 k / m^* \qquad (2.15)$$

and

$$g(E) = \frac{m^* \sqrt{2m^* E}}{\pi^2 \hbar^3} \qquad (2.16)$$

For more complicated surfaces, such as away from the band edges, numerical approaches are required. Figure 2.5(a) shows the calculated densities of states for the band structure calculations of Figs. 2.5(b) and 2.6(b). The integrand of Eq. (2.12) will be large where $\nabla_k E_n(\mathbf{k})$ approaches zero, i.e. where the E-$\mathbf{k}$ relationship is flat. Such points are called critical points and densities of states generally have a maximum near such points. However $g(E)$ drops to zero at the band edge since S_E drops to zero here. Experimental measurements are in reasonable agreement with the calculations of Fig. 2.5(a) [2.14].

2.7 MOMENTUM AND EFFECTIVE MASS

The velocity, $\boldsymbol{v}_{n\mathbf{k}}$, of an electron in band n with wave vector $\mathbf{k}$, as evaluated as the group velocity of a wave packet centred at $\mathbf{k}$ or as the expectation value of a quantum mechanical velocity operator [2.6], is given by:

$$\boldsymbol{v}_{n\mathbf{k}} = \frac{1}{\hbar} \nabla_{\mathbf{k}} E_n(\mathbf{k}) \tag{2.17}$$

The velocity is normal to the constant energy surface at the appropriate $\mathbf{k}$ and is therefore parallel to $\mathbf{k}$ only in special cases. Note that the denominator of Eq. (2.12) can be simplified using the above expression to give the following expression for the density of electron states (per unit energy and volume) contributed by band n:

$$g_n(E) = \frac{2}{\hbar(2\pi)^3} \oint \frac{dS_E}{|\boldsymbol{v}_{n\mathbf{k}}|} \tag{2.18}$$

An external force $\boldsymbol{F}$ acting on the electron, prior to any collisions and assuming $\boldsymbol{F}$ is not so large as to cause excitations between bands, will cause $E_n(\mathbf{k})$ to increase. The conservation of energy implies:

$$\frac{dE_n(\mathbf{k})}{dt} = \boldsymbol{v}.\boldsymbol{F} \tag{2.19}$$

However, mathematically:

$$\frac{dE_n(\mathbf{k})}{dt} = \nabla_{\mathbf{k}} E_n(\mathbf{k}) \cdot \frac{d\mathbf{k}}{dt} \tag{2.20}$$

Equations (2.17), (2.19) and (2.20) give the result:

$$\boldsymbol{F} = \frac{d(\hbar\mathbf{k})}{dt} \tag{2.21}$$

The quantity $\hbar\mathbf{k}$ in a crystal therefore plays the role of momentum in free space and is called the ***crystal momentum***. Like momentum, it is conserved in interactions of electrons with other quasiparticles within the crystal. One obvious difference is apparent at silicon's conduction band minimum. From Eq. (2.17), $\boldsymbol{v}_{n\mathbf{k}}$ is here zero although the crystal momentum is finite.

The electron's acceleration is given by:

$$\boldsymbol{a} = \frac{d\,\boldsymbol{v}_{n\mathbf{k}}}{dt} \tag{2.22}$$

Dropping the velocity subscript and discussing in terms of vector components gives:

$$a_i = \frac{dv_i}{dt} = \frac{1}{\hbar}\frac{d}{dt}\left(\frac{\partial E_n}{\partial k_i}\right) = \frac{1}{\hbar}\sum_j \left(\frac{\partial^2 E_n}{\partial k_i \partial k_j}\right)\frac{dk_j}{dt}$$
$$= \sum_j \frac{1}{m^*_{ij}} F_j \tag{2.23}$$

The acceleration can therefore be described in general by an effective mass tensor with elements:

$$\frac{1}{m^*_{ij}} = \frac{1}{\hbar^2}\frac{\partial^2 E}{\partial k_i \delta k_j} \tag{2.24}$$

Near the conduction band minimum or valence band maximum, a Taylor series expansion about $\mathbf{k} - \mathbf{k}_o$ also involves terms of the same form:

$$E(\mathbf{k}) = E(\mathbf{k}_o) + \frac{1}{2}\sum_i \sum_j \left(\frac{\partial^2 E}{\partial k_i \partial k_j}\right)_{\mathbf{k}_o} \Delta k_i \Delta k_j \tag{2.25}$$

For the conduction band of silicon, constant energy surfaces are

ellipsoids with rotational symmetry (spheroids), as shown in Fig. 2.7, resulting in a diagonal effective mass tensor with only two different terms, the longitudinal and transverse effective masses. Off-diagonal terms in Eq. (2.24) and (2.25) are zero. At low temperatures, these effective masses have the values $0.92m_o$ and $0.18m_o$ respectively, and do not vary significantly with temperature [2.15].

The valence band case looks even simpler in Fig. 2.7 but is more complicated in practice. Shown in Fig. 2.7 is the spherical constant energy surface corresponding to the "uppermost" valence band in Fig. 2.6(b).

The actual silicon band structures differ from that shown in Figs. 2.5 and 2.6 due to effects known as ***spin-orbit splitting***. The Schrödinger Equation, Eq. (2.1), needs to be modified at high electron velocities where relativistic effects become important. These modifications are more important for the tightly bound core electrons than for the almost free conduction band electrons. In particular, the valence band structure of Fig. 2.6(b) is modified, particularly for the three valence bands which come together at $\mathbf{k} = 0$. As shown in Fig. 2.8, the uppermost valence band of Fig. 2.6(b), which is degenerate over most of the zone (i.e., consists of two superimposed bands), is split by spin-orbit effects into a ***heavy hole*** and a ***light hole*** band, each with different effective mass ($0.52\ m_o$ and $0.16\ m_o$) respectively. The second valence from the bottom in Fig. 2.6(b) becomes "split-off" at $\mathbf{k} = 0$ by these effects, lying 44 meV lower in energy at $\mathbf{k} = 0$ than the "light" and "heavy" bands. The corresponding effective mass near this point is $0.25\ m_o$. The two uppermost bands are important at low temperature (where the thermal energy, kT, is much less than 44 meV), while the "split-off" band becomes more important near room temperature when it is reasonably well populated by holes.

The departure of the constant energy surfaces from sphericity already mentioned becomes even more exaggerated when spin-orbit effects are taken into account.

The approach generally taken to overcome these complications is to undertake calculations assuming simple spherical constant energy surfaces. In more complex calculations involving the actual energy surfaces, an expression is then derived for what might be termed an "effective" effective mass which, when substituted into the simpler

analysis, gives the same numerical result. Hence, there are several types of effective mass required for silicon, e.g., the "density of states" effective mass, the "conductivity" effective mass, the "thermal velocity" effective mass, the "cyclotron" effective mass and so on, none of which need be equal to one another.

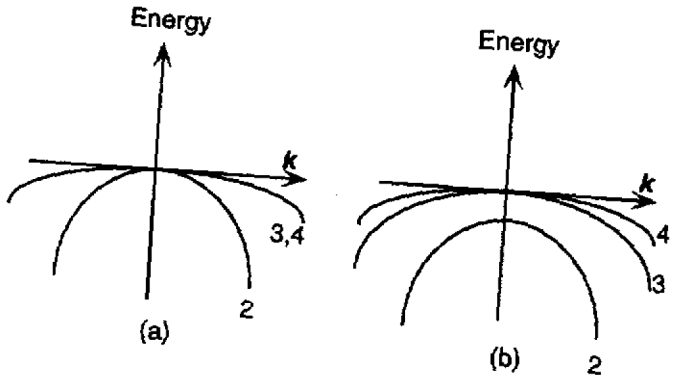


Figure 2.8: Effect of spin-orbit splitting on the three uppermost valence bands near k = 0: (a) without spin-orbit splitting; (b) with spin-orbit splitting.

REFERENCES

2.1 A. Anselm, "Introduction to Semiconductor Theory", Prentice Hall, New Jersey, 1981.

2.2 A.C. Smith, J.F. Janak and R.B. Adler, "Electronic Conduction in Solids", McGraw Hill, New York, 1967.

2.3 T. Hey and P. Walters, "The Quantum Universe", Cambridge University Press, Cambridge, 1987.

2.4 C.T. Sah, "Fundamentals of Solid-State Electronics", World Scientific, Singapore, 1991.

2.5 Martin A. Green, "Solar Cells: Operating Principles, Technology and System Applications", (Prentice-Hall, New Jersey, 1982). (Reprinted 1986, 1992 by the author).

2.6 P.T. Landsberg (ed.), "Solid State Theory: Methods and Applications", Wiley Interscience, London, 1969.

2.7 M. Tiukham, "Group Theory and Quantum Mechanics", McGraw-Hill, New York, 1964.

2.8 L.B. Bouckaert, R. Smoluchowski and E. Wigner, "Theory of Brillouin Zones and Symmetry Properties of Wave Functions in Crystals", Physical Review, Vol. 50, pp. 58-67, 1936.

Chapter

6

LIGHT TRAPPING

6.1 INTRODUCTION

To maximize the open-circuit voltage of a solar cell, recombination must be minimized throughout the cell, including recombination in the bulk of the cell. An effective way of reducing bulk recombination is to reduce the volume of the cell. It follows that, to obtain the best possible photovoltaic performance from silicon, every possible advantage must be taken of the light absorbing capabilities of a given cell volume. This means taking advantage of schemes which trap the light into the cell so that, if not absorbed during its first passage through the cell volume, light will have additional opportunities for absorption.

Such pathlength enhancement in the bulk regions of the cell is referred to as "light trapping". The same term is sometimes used to refer to the multiple reflections of externally incident light from the surface of a cell with surface texture, which reduce overall reflection loss. Reflection control in both unencapsulated and encapsulated cells is discussed in Appendix F. In the present chapter, such surface reflection will be assumed negligible and "light trapping" refers solely to bulk processes.

Figures 6.1(a) and (b) show two different types of light trapping schemes [6.1]. The first is based upon the randomization of the direction of light once it has been coupled into the semiconductor.

To be coupled out of the silicon, a light ray has to strike the surface of silicon within an angle to the normal equal to $arcsin(1/n)$ where n is the refractive index of silicon. This angle is only about 16 - 17° for silicon. The rest of the light is reflected by total internal reflection. This means that only a fraction of the light will escape from the silicon on each passage across it. In the second scheme, a regular geometrical structure is built into the bulk region to steer the light away from the normal to the front cell surface. This chapter describes the light-trapping properties of both the ***randomizing*** and ***geometrical*** schemes of Fig. 6.1.

6.2 RANDOMIZING SCHEMES

The light trapping properties of the randomizing or ***Lambertian*** scheme of Fig. 6.1(a) can be relatively simply analyzed [6.2]. The randomizing or Lambertian rear reflector is defined as reflecting light with uniform brightness (radiance) in all directions, regardless of the original angle of incidence. (Uniform "brightness" corresponds to a radiant intensity which varies as $cos\theta$ where θ is the angle between the direction of observation and the normal to the surface reflecting the light [6.2]).

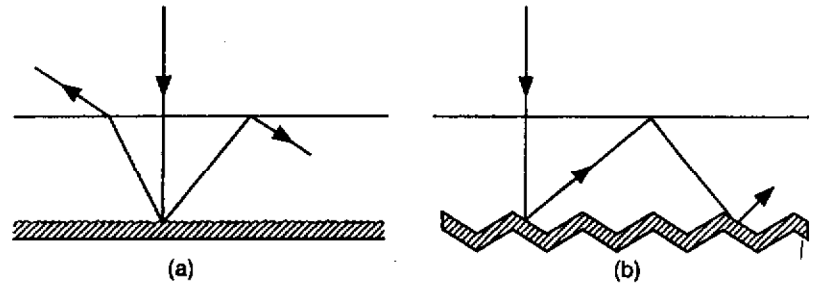


Figure 6.1: Two schemes for trapping light into a solar cell;(a) scheme based upon internal randomization of the light direction; (b) geometrically based scheme.

The key result of this analysis is that, in the case of weak absorption, a fraction of the light, equal to $1/n^2$, will be coupled out of the top surface after each reflection from the rear surface, assuming that the top surface has unity transmittivity for the light involved. The light coupled out will be that travelling in the cell in a direction close to the normal to the top surface. Its pathlength across the cell to this

surface will approximately equal the cell thickness. The light which is not coupled out will be reflected to the rear of the cell where its direction will be re-randomized. On each passage across the cell, this light travels an average distance which is equal to twice the cell thickness, due to its being oblique to the normal (a total of four cell thicknesses between rear surface reflections).

One possible figure of merit for a light trapping scheme is the pathlength enhancement which is possible in the limit of weakly absorbed light. This is the ratio of the average pathlength of such a light beam to the minimum possible pathlength, which equals the average cell thickness, W. By calculating the pathlength of the light which is coupled out after each successive rear reflection, the following power series can be constructed for the average pathlength of the scheme of Fig. 6.1(a).

$$\bar{P} = 2W/n^2 + 6W(n^2-1)/n^4 + 10W(n^2-1)^2/n^6 + \ldots \qquad (6.1)$$

The power series expansion:

$$1/(1-x) = 1 + x + x^2 + x^3 + x^4 + \ldots \qquad (6.2)$$

can be used to simplify Eq. (6.1) to give the following expression for the pathlength enhancement factor B:

$$B = 4n^2 - 2 \qquad (6.3)$$

This approximately equals the value of $4n^2$ which is also the approximate result of a more comprehensive analysis of this structure by Sheng [6.3], and that of a more general analysis by Yablonovitch and Cody [6.4] and Yablonovitch [6.5]. The value of the pathlength enhancement factor is close to 50 for silicon, indicating the substantial benefits which light trapping can provide.

The more general structures of Figs. 6.2(a) and (b) can be analyzed using a similar approach. The work of Yablonovitch and Cody [6.4] indicates that a fraction, $1/n^2$, of the randomized light striking the top surface will be coupled out even when it is randomly textured as in Fig. 6.2(a). This allows the same type of analysis as that above to be applied to this structure.

Such an analysis gives a pathlength enhancement equal to the previously mentioned value of $4n^2$. The structure of Fig. 6.2(b) also has the same value when an ideal reflector is used at the rear surface, either in intimate contact or detached, as shown. If no rear reflector is used, the pathlength enhancement factor has half of the previous value (assuming unity transmittivity for rays capable of escaping from the rear surface). This reduction by two would be expected from symmetry [6.4].

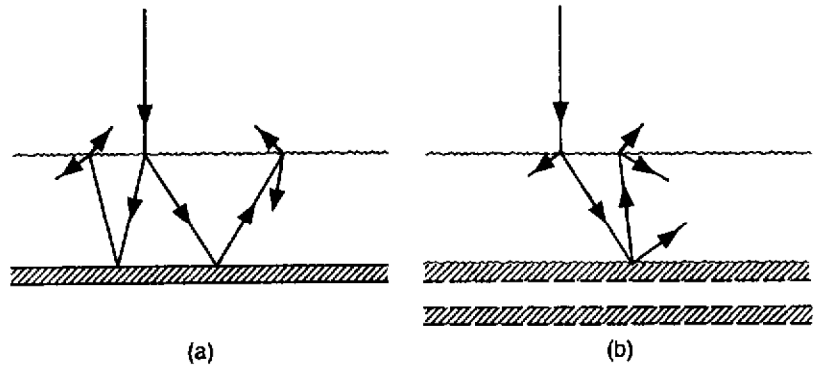


Figure 6.2: Other randomizing light trapping schemes; (a) planar rear surface; (b) both surfaces randomizing. The broken lines at the rear surface indicate two different locations of the rear reflector

The previous expressions assume perfect rear reflectors. With a variable rear surface reflectance, R, the expression for pathlength enhancement for the schemes of Figs. 6.2(a) and (b) becomes:

$$B = 2(1+R)/[1-R(1-1/n^2)] \qquad (6.4)$$

From this, the value of reflectance required to maintain more than a fraction, f, of the light trapping ability of the idealized case is found to be:

$$R > (2fn^2 - 1)/[2f(n^2-1) + 1 \qquad (6.5)$$

For silicon, the reflectance must be greater than 91% to do at least half as well as the idealized case. If a metal reflectance better than this cannot be obtained, it would be more effective to rely upon total internal reflection from the rear surface. Although previously stated

that this approach would give performance limited to half that of the idealized reflector case, the approach could do better than this in practice by designing for a lower than unity transmittivity of rays within the escape cone at the rear, or by using a simple detached rear reflector (Fig. 6.2(b)). The white polymer layer normally used at the rear of present solar cell modules could be used as such a detached reflector.

Experimentally, it is possible to obtain rear reflectance higher than the figure of 91% previously mentioned by interposing a dielectric layer between the metal and the silicon. Figure 6.3 shows the calculated reflectance, at a wavelength of 1.2 μm, from a rear Al layer separated by a variable thickness of SiO_2 from a polished silicon substrate, for various internal angles of incidence, θ, upon this combination.

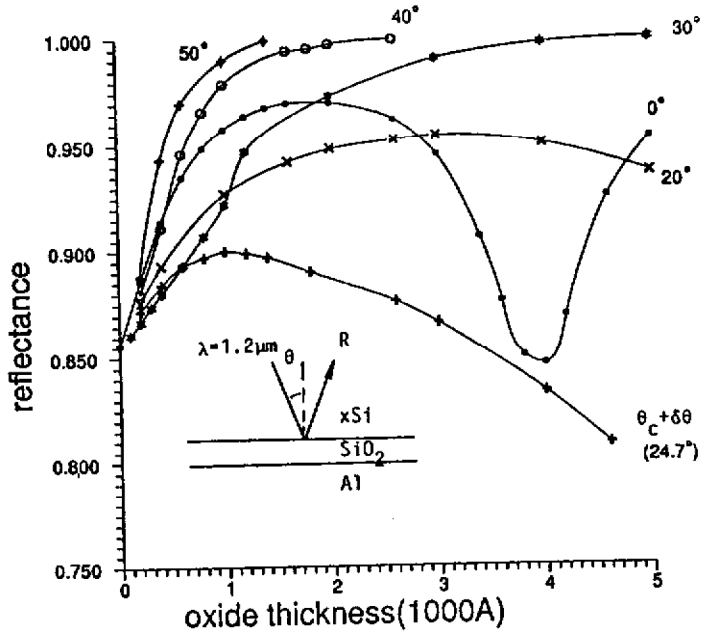


Figure 6.3: Calculated reflectance from a rear Al reflector at the rear of a silicon wafer as a function of the thickness for an intervening layer of SiO_2, for various internal angles of incidence. The reflectance for the $\theta_c + \delta\theta$ case reaches a minimum for about 1 mm oxide thickness (not shown), then increases towards unity (after Campbell [6.6]).

The combination of Fig. 6.2 is of interest for the high efficiency laboratory cells of Chapter 10. For angles of incidence below the critical angle for total internal reflection from the Si/SiO_2 interface (24.7°), cyclic interference effects predominate as the thickness of the oxide layer increases. Above the critical angle, reflectance approaches 100% as the oxide thickness increases and the detached reflector situation, described above, is approached. Reflectance is lowest near the critical angle. Just below the critical angle, the ray refracted at the Si/SiO_2 interface travels almost parallel to this interface, providing plenty of opportunity for energy transfer to the rear metal. More surprisingly, reflection is also low for angles of incidence just above the critical angle.

6.3 GEOMETRICAL LIGHT TRAPPING

6.3.1 Introduction

The levels of light trapping provided by the previous randomizing (Lambertian) schemes have sometimes been considered as limits on obtainable performance [6.7]. It appears that there may well be limits for cells with an ***isotropic*** response. (That is, for a cell which gives the same response, regardless of the angle of incidence of the light). However, the direction of most incident sunlight is predictable and, consequently, an isotropic response is not likely to be optimal. A cell design would be superior where the response at the less important oblique angles of incidence is traded off against the response for light incident at directions closer to the perpendicular.

Some ways of achieving such a trade-off for randomizing schemes are outlined in Section 6.6. Another possibility is that a geometrical light trapping scheme such as in Figure 6.1(b), designed for perpendicularly incident light, would also exhibit a superior performance to that of randomizing schemes for a range of angles of incidence close to the perpendicular.

The theory of geometrical light trapping is more difficult than that for randomizing approaches. However, such schemes can be analyzed on an individual basis by ray tracing.

6.3.2 Two Dimensional Geometries

The simple geometrical scheme of Fig. 6.1(b), proposed by Redfield [6.8], relies on reflection from an oblique rear surface such that the reflected light is totally internally reflected upon reaching the top surface. Due to the narrow escape cone from silicon, the required slope for the rear surface is quite small. However, one disadvantage is that, to maintain finite cell thickness, oppositely sloping surfaces are also required. While sequential incidence on surfaces of the same slope can build up increasingly oblique angles of incidence on the top surface, ensuring total internal reflection, incidence on oppositely sloping faces will decrease this obliqueness. In the worst case, perpendicularly incident light will have only four passes across the cell as for the ray shown dashed in Fig. 6.4. Much larger numbers of passes are possible for rays incident at other points, such as indicated by the solid line in Fig. 6.4.

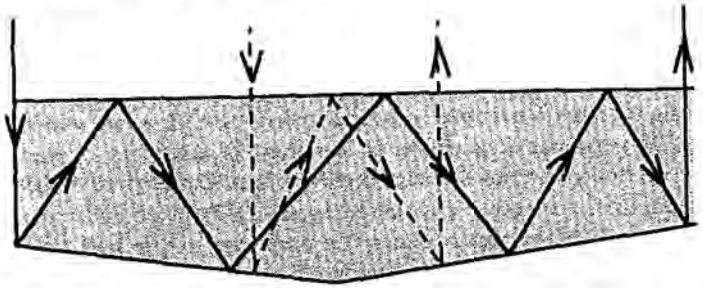


Figure 6.4: Good (solid line) and bad (dashed) ray paths for light trapping with rear surface slats.

The extent of light trapping thus depends upon the point of incidence along the surface. Some geometries give "sweet spots", namely localized areas where incident light will be guaranteed very long light trapping paths. However, the longer the pathlength, the smaller the area of the sweet spot. Certain geometries give pathlength enhancements approaching infinity for light incident on an infinitesimally small area. However, averaged over the total surface area, all designs perform relatively modestly. The number of passes when so averaged generally lies between 4 and 15, generally smaller than the effective value of the Lambertian schemes of Section 6.2.

Another two dimensional geometry which has received some attention is the case of slats (grooves) on the top surface, particularly when these slats are formed by intersecting (111) crystallographic planes (see Chapter 10). For upright slats, symmetry dictates that most light will have only two passes across the cell as shown in Figure 6.5(a). The only rays that do not escape after the first double pass across the cell are rays obstructed on their first passage across the cell by striking internally one of the faces of the slats. However, if this symmetry is destroyed by slightly tilting the slats, much better light trapping can result as shown in Fig. 6.5(b) [6.9, 6.10].

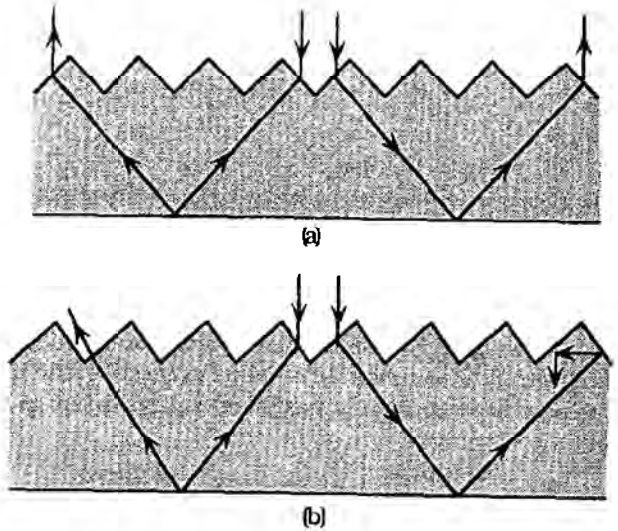


Figure 6.5: Light-trapping with top surface grooves formed by intersecting {111} equivalent planes: (a) untilted structure; (b) effect of a slight tilt.

Another two dimensional light trapping geometry depending on slats which has been suggested [6.11] is shown in Fig. 6.6. If the two sides of the cell are parallel, four passes across the cell are possible. However, if the two sides are not parallel, as indicated in Fig. 6.6, an increased number of passes become possible. The scheme would seem to have two advantages over the simpler scheme of Figs. 6.1(b)

and 6.4. One is that escaping rays can be recaptured. The second is that a smaller misorientation between front and rear sides of the cell is required to ensure total internal reflection. This is due both to the fact that most light will be incident obliquely as indicated, combined with the smaller range of angles each face of the cell would be required to accept.

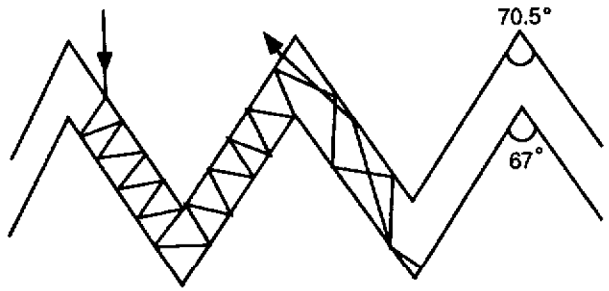


Figure 6.6: Near-parallel double-sided slat approach. Effective device thickness could best be defined as cells aperture area divided by volume [6.11].

Although a difficult structure to implement in crystalline silicon, for which the scheme was proposed [6.11], it may be well suited for thin film cells. These could be deposited nearly conformally onto an appropriately structured substrate or superstrate, with the difference between deposition rates near peaks or valleys used to prevent parallelism of cell surfaces.

Finally, another two dimensional approach is based on holographic gratings which have also been proposed for the rear of the cell to diffract light into oblique modes for effective light trapping [6.12]. However, the calculated pathlength advantages are quite modest.

6.3.3 Three Dimensional Geometries

The additional surface planes introduced by replacing grooves by three dimensional pyramids on the top surface reduce opportunities for escape [6.13]. These pyramids are readily formed by anisotropically etching (100) orientated starting wafers to expose four intersecting (111) equivalent planes (Chapter 10, Fig. 10.4). With a planar rear surface, an image region can be defined which describes the areas where the rays reflected from the rear surface re-emerge

internally on the surface pyramids (Fig. 6.7). The portion of the pyramid on which this image region lies depends on the particular geometry, specifically the ratio of the pyramid size to the width of the wafer for the regular geometry of Fig. 6.7. Light re-emerging on the side planes will be very effectively trapped into the cell, while that re-emerging on planes of opposite orientation to the plane of incidence will be coupled straight out as shown in Fig. 6.5(a).

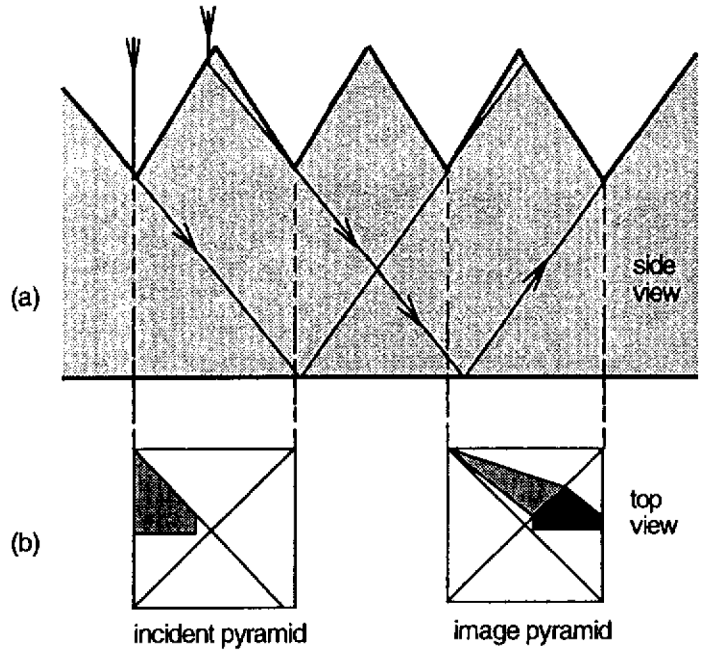


Figure 6.7: Major ray paths in regular pyramid layout: (a) side view; (b) "image region" where rays resurface.

Figure 6.8 shows the percentage of light remaining trapped as a function of the number of passes across the cell [6.13]. The performance of a regular pyramid layout depends on the precise geometry as indicated by the cross hatched region.

Random layouts of pyramids perform better than all but the most ideal of the regular pyramid layouts and would be preferable in practice, due to the difficulties in controlling the geometries involved. Inverted pyramids (Chapter 10) give slightly better performance than

the regular upright pyramid arrangements due to the higher possibility of re-entry of escaping rays. Smith and Roghati [6.14] compare the light trapping properties of regular layouts of upright and inverted pyramids, but without discussing the geometrical dependencies indicated above. Results for one particular geometry cannot be used to draw conclusions about more general geometries.

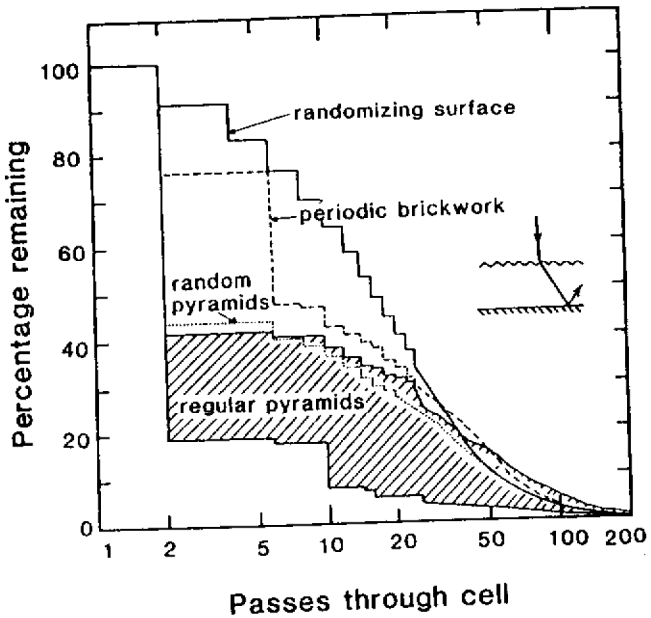


Figure 6.8: Fraction of rays remaining trapped in cell as a function of the number of passes across the cell for cells with top surface structure. The Lambertian case is shown for comparison. The "periodic brickwork" entry corresponds to the "Tilers pattern" of Fig. 6.9.

Three different approaches have been suggested to improve upon the light trapping ability of such pyramidal structures. One is to add surface structure to the rear of the wafer. The second is to design pyramid layouts so that the image pyramid falls into desired locations and the third is to tilt the pyramid structure.

The tiler's pattern of Fig. 6.9 has been suggested [6.13] to allow the re-emergence of the image region on optimal locations on the

pyramids. As seen in Fig. 6.8, the optimum tiler's pattern approaches the performance of the Lambertian scheme and is significantly better than either random or regular pyramids. However, in its worst possible configuration, performance equal to that of the worst regular pyramid geometry might be expected. Such Tiler's pattern layouts are used in the highest efficiency silicon cells fabricated to date (Chapter 10).

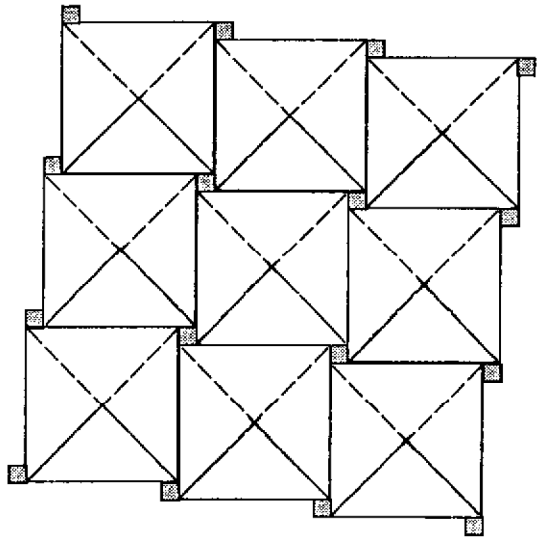


Figure 6.9: "Tiler's pattern" designed for favourable location of image region.

Even better performance, in principle, can be obtained with structure also on the rear of the cell. One of the early geometries suggested for obtaining such benefits was the perpendicularly grooved cell of Fig. 6.10 [6.15]. The perpendicular grooves on the rear encourage reflections into the third dimension, greatly limiting the potential for escape.

An analysis of this structure [6.13] shows that it can exceed the light trapping capabilities of the Lambertian scheme for perpendicularly incident light. It is of interest to see whether this improved light trapping performance comes at the expense of decreased angular sensitivity. The scheme was found not to be particularly angularly sensitive. Geometries optimized for perpendicular light remained

superior to the Lambertian approach for angles of incidence up to 45° [6.13].

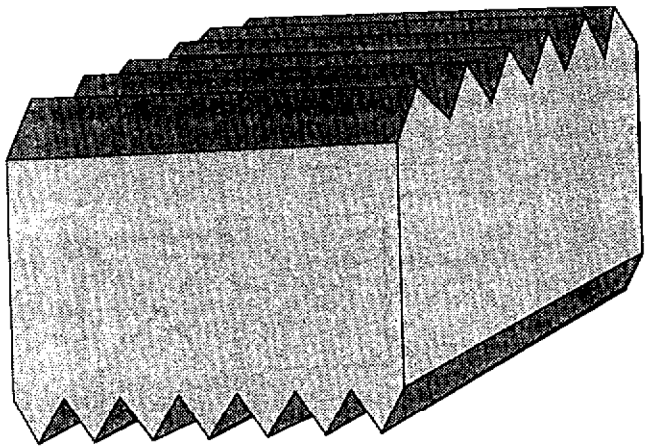


Figure 6.10: Perpendicular groove light-trapping scheme.

Other double sided cell structures also perform markedly superior to their single sided counterparts [Fig. 6.11]. However, the "double bounces", of benefit for coupling light into the cell with such surface structures (Chapter 10) can be detrimental to effective light trapping. With rear surface structures, light reflected from the rear surface will, in general, incur multiple reflections before being transmitted back across the cell. This reduces the effective reflectance of the rear surface. The increased surface area also makes surface passivation more challenging in practice. Given these limitations, schemes with top surface structure but with a planar rear surface are preferred in the highest performance experimental devices to date.

Good light trapping in this preferred configuration can be obtained by tilting the geometric structure on the top surface. In the same way as simple two dimensional tilting of slats improves light trapping (Fig. 6.5), tilting of both pyramids and slats into the third dimension can give even further benefits. Figure 6.12 shows the rays remained trapped after a given number of passes for both tilted grooves and pyramids showing that excellent light trapping can be obtained. The same conditions giving good light trapping in the cell also lead to greatly reduced surface reflection when the cells are encapsulated under glass.

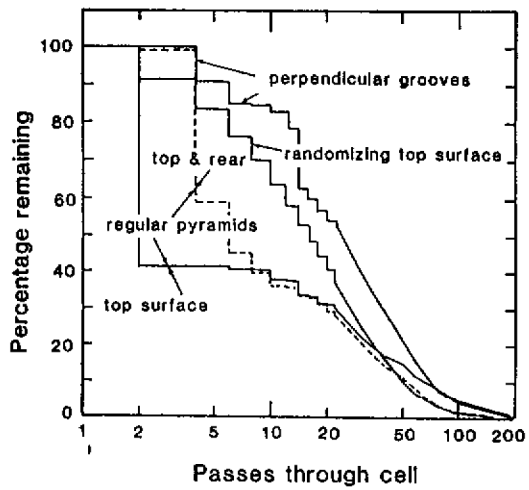


Figure 6.11: Light-trapping properties of double-sided light-trapping schemes involving structure on both cell surfaces. Shown is the fraction of light remaining trapped as a function of the number of passes across the cell.

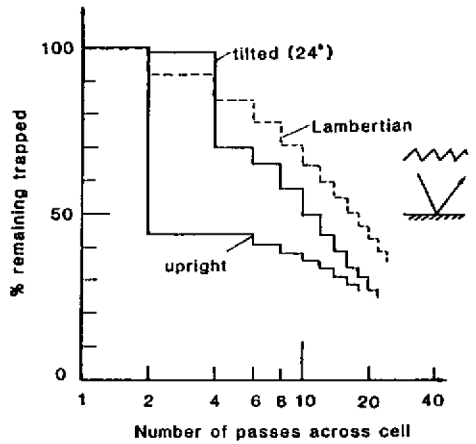


Figure 6.12: Light trapping properties of upright and tilted pyramids (random layout).

Figure 6.13 compares some of the light trapping schemes discussed above in terms of their most important property; their effect upon the short-circuit current of a silicon solar cell [6.13]. The perpendicular slats approach can perform better than Lambertain schemes. Schemes with pyramids on both surfaces also perform well in principle although there are practical constraints as previously outlined. Upright pyramids on one side only perform at a level intermediate between that of a polished wafer and a good double-sided structure. The "tilers pattern" layout or tilting of pyramids (not shown) would perform closer to the Lambertian reference.

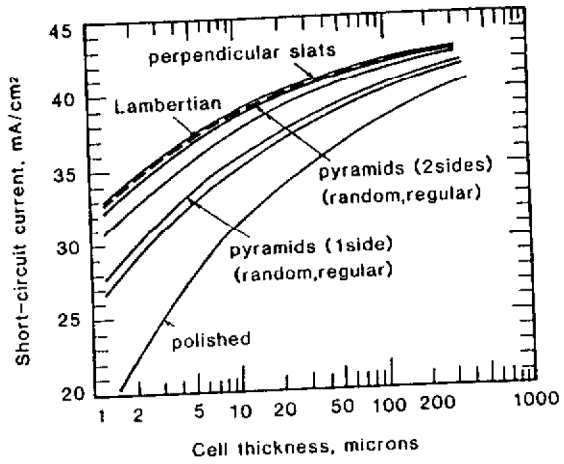


Figure 6.13: Calculated short-circuit current density as a function of silicon cell thickness for various light-trapping schemes (after Campbell & Green [6.13]). All schemes assume zero front surface reflection and a perfect rear reflector. (The illumination used was the global AM1.5 spectrum of Appendix H with a power density of 97 mW/cm^2).

6.4 Experimental Results

The increased absorption in a silicon wafer with one side flat and the other roughened was shown in one of the earlier theoretical papers on light trapping [6.4]. Good results were also reported for

amorphous silicon cells, beginning in 1982, with pathlength enhancement close to the theoretical limit reported [6.16]. Light trapping was shown to contribute to the long wavelength response of the improved crystalline silicon cells of the early 1980's [6.17]. Pathlength enhancement up to a factor of about 10 was demonstrated at long wavelengths [6.17]. Subsequently, greatly increased current output was demonstrated for cells with pyramidally textured top surface and a planar rear surface when compared to cells with a double layer antireflection coating on a planar top surface, due to light trapping differences [6.18]. Keavney et alia [6.19] describe early optical measurements. More recently, Basore [6.20] has described a technique for extracting light trapping parameters by analysis of a cell's wavelength response. This technique is able to distinguish between different light trapping schemes incorporated into experimental cells.

The internal quantum efficiency *(IQE)* of a cell is calculated at each wavelength from the measured spectral response, $SR(\lambda)$ (amps/watt), and the hemispherical reflectance, $R(\lambda)$, using:

$$IQE = SR \cdot (hc/q\lambda)/(1-R), \qquad (6.6)$$

where λ is the free-space wavelength.

Previously, *IQE* at infrared wavelengths had frequently been used to extract information about minority carrier diffusion lengths in the cell. Less frequently, it had been used to extract information about rear surface recombination velocity and light trapping properties [6.17]. The approach of Basore [6.20], however, allows these properties to be extracted routinely to an accuracy estimated elsewhere [6.20].

By plotting inverse *IQE* as a function of inverse absorption coefficient, α, characteristics such as shown in Fig. 6.14 are experimentally generated, with similar features also predicted by numerical device simulation programs. Two linear regions are observed characterized by the inverse slopes, L_{iqe} and W_{iqe}, and by the y-axis intercept, *Intcpt*. As shown by the analysis of Appendix G, L_{iqe} is related to the effective diffusion length, L_{eff}, in the cell (independent of light trapping properties), while the product W_{iqe}.*Intcpt* depends only on the optical properties of the cell and is

independent of the cell's electrical properties!

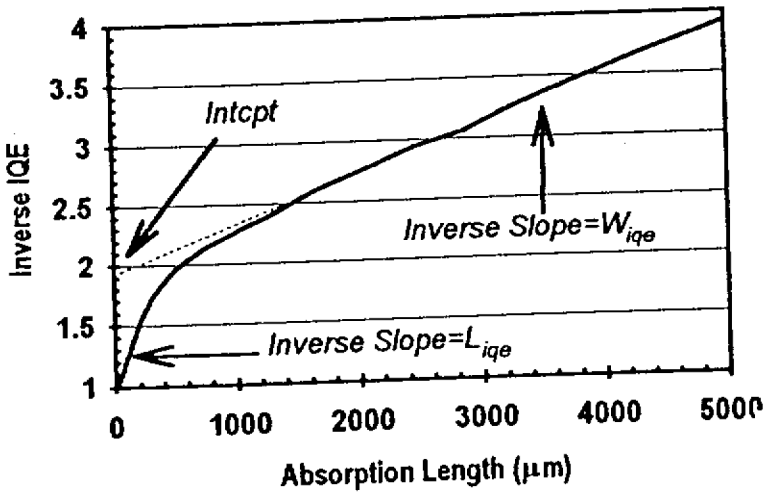


Fig. 6.14: Typical inverse internal quantum efficiency (*IQE*) data for an experimental cell (after Basore [6.20]).

Various information can be extracted by combining the three parameters extracted from plots corresponding to Fig. 6.14 with other measured or estimated parameters (see Fig. G.1) such as the cell thickness (W), the total front surface reflection at infrared wavelengths (R_{sub} and R_{fe} respectively), the angle of passage of light across the cell on first, second and subsequent passes (θ_1, θ_2 and θ_n respectively, with passes after the second assumed identical), and the corresponding back and front internal reflectances (R_{b1}, R_{f1}, R_{bn} and R_{fn} respectively). Information which can be extracted to varying accuracy [6.20] includes bulk diffusion length, rear surface recombination velocity, the bulk component of dark saturation current and light trapping parameters, particularly the rear surface reflectance, R_{bn}, and the pathlength enhancement factor, Z, defined in Appendix G. (Note that Z always larger than B of Section 6.2 in that parasitic absorption at the rear surface is excluded from the definition of Z).

The procedure for extracting this information is outlined elsewhere [6.20]. The starting point is the experimental value of the product

W_{iqe}.*Intcpt* which, as noted, depends only on the optical parameters. Sensitivity analysis [6.20] shows that the product is overwhelmingly sensitive to R_{bn}. By assuming reasonable values for the other optical parameters (R_{b1}, R_{f1}, R_{fn}, θ_1, θ_2, θ_n), values of R_{bn} can be deduced to about 5% accuracy, in general. Knowing this parameter, the long wavelength collection efficiency, η_c, can be deduced to a similar accuracy. Since both this parameter and L_{eff} depend on bulk diffusion length and surface recombination velocity, but in a different way, the two latter parameters can then, in principle, be deduced. Greatest accuracy is obtained when the effective diffusion length approximately equals the cell thickness [6.20].

6.5 CONCENTRATED LIGHT

As discussed in more detail in Chapter 12, photovoltaic systems based upon concentrated sunlight have been widely explored. Typically, sunlight is concentrated onto a cell using a Fresnel lens as in the widely deployed concentrating system of Fig. 6.15. Such systems can use only the direct component of the sunlight, and the range of angles which the cell must accept is very well defined. For example, for the system shown in Fig. 6.15, all of the rays from the lens which strike the cell must do so within an angle of 34° to the normal to the cell surface. This gives rise to potentially more effective light trapping schemes than possible in the case of non-concentrating cells.

Figures 6.16(a) and (b) show two ways in which this is possible using randomizing light trapping schemes [6.21]. Figure 6.16(a) shows a scheme in which the top contact is in the form of compound parabolic concentrators which focus light onto a fraction, $1/sin^2\theta$, of the top surface of the cell, where θ is the acceptance half-angle of the scheme. This limits the area of the surface of the cell available for the escape of light. Assuming that all of the metallic surfaces act as ideal reflectors, this boosts the path length enhancement available from the randomizing approach from $4n^2$ to $4n^2/sin^2\theta$. Schemes such as the prismatic cover approach, described in Chapter 12, which steer light from metallized regions of the cell to non-metallized, are also closely related to this approach.

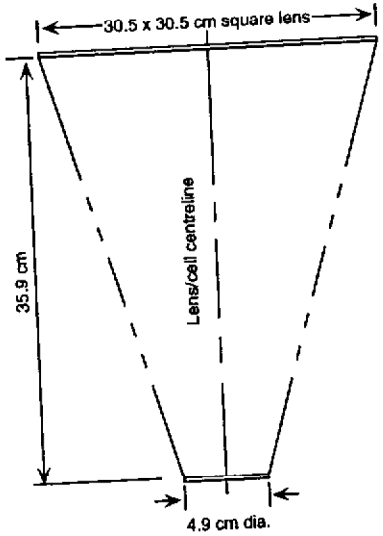


Figure 6.15: Typical arrangement of lens and cell in a photovoltaic concentration system.

The scheme shown in Fig. 6.16(b) relies upon an angularly selective anti-reflection coating. Rays which are incident at an angle which is within θ of the cell normal are coupled into the cell, whereas rays outside of this angle are reflected. Reciprocally, this acts to restrict the escape cone of light from within the cell to that of a material with a refractive index of $n/sin\theta$; again giving an idealized path length enhancement of $4n^2/sin^2\theta$. Such coatings have proved difficult to design [6.6].

The schemes of Fig. 6.16 boost the idealized path length enhancement factor to over 2 million for extreme cases under direct sunlight. However, the practical constraints of less than unity metal reflectance and the likely deviations of anti-reflection coating properties from the idealized one for the scheme of Fig. 6.16(b) will undoubtedly restrict experimental factors to much more modest values.

Although discussed in the context of concentrating cells, either of the previous schemes could be modified for use in non-concentrating systems where the ability to accept diffuse light, at least partially, is required.

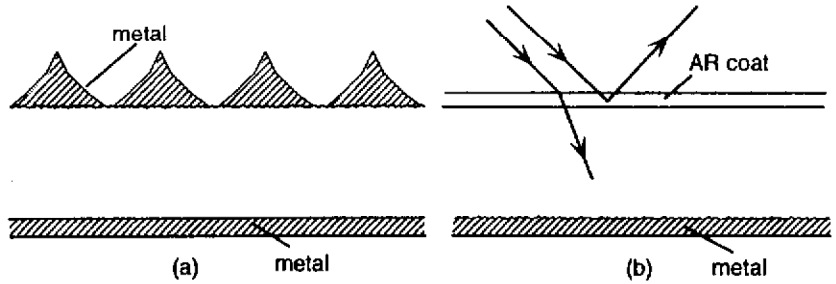


Figure 6.16: Two different schemes for enhancing light trapping for cells where a limited acceptance angle is adequate: (a) use of a secondary surface concentrator; (b) use of an anti-reflection coating with a high degree of angular selectivity.

6.6 Light Trapping In Encapsulation

Somewhat related to light trapping in cells is light trapping in cell encapsulation. Figure 6.17 demonstrates how this might occur even in a standard photovoltaic module. The "zero depth concentrator", which relies on light incident between cells being scattered from the white rear layer of the module, was well known in the late 1970's to be able to boost the short-circuit current of encapsulated cells by up to 20%.

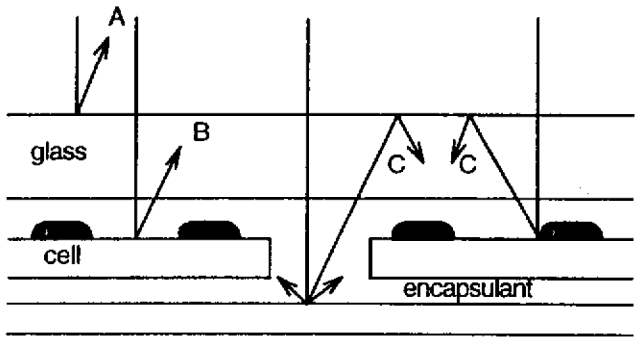


Figure 6.17: Reflections within a typical module.

Yablonovitch [6.5] included an analysis of such an effect in early work on light trapping. He showed that, using a rough cell surface, a scheme such as shown in Fig. 6.18 could reduce cell reflection from

31% prior to encapsulation to 11% after encapsulation, with a large portion of this reduction due to light trapping within the encapsulation layer [6.1].

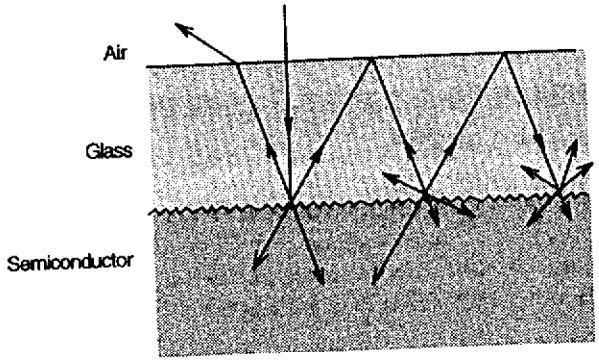


Figure 6.18: Reflection reduction from a scattering surface after encapsulation.

Subsequently, Wenham et alia [6.9] pointed out the benefits which could be obtained by geometrical schemes by considering cells with tilted pyramids on the cell surface. Such tilting can be readily achieved by cutting wafers slightly "off-axis" from the (100) orientation. A 20 kW photovoltaic system in California appears to use such an approach [6.1]. Figure 6.19 shows how benefits arise.

More recently, Blakers [6.22] has reported the results of an analysis for trapping of light reflected from metal fingers assuming cylindrical geometries and specular reflection from the metal. Extension to the calculation of the light trapping of light diffusely reflected would be straightforward.

Perhaps the ultimate development of this general approach is the static concentrator of Fig. 6.20 which uses light trapping in the glass and cells with a bifacial response to achieve effective concentration ratios of up to 4 [6.23].

Since light trapping within encapsulation schemes rely on total internal reflection from the encapsulant surface, the effect of dust accumulation on such surfaces is an important issue [6.23]. This effect appears to be only about half as severe as the normal effect of dust in reducing light transmission into the module [6.24].

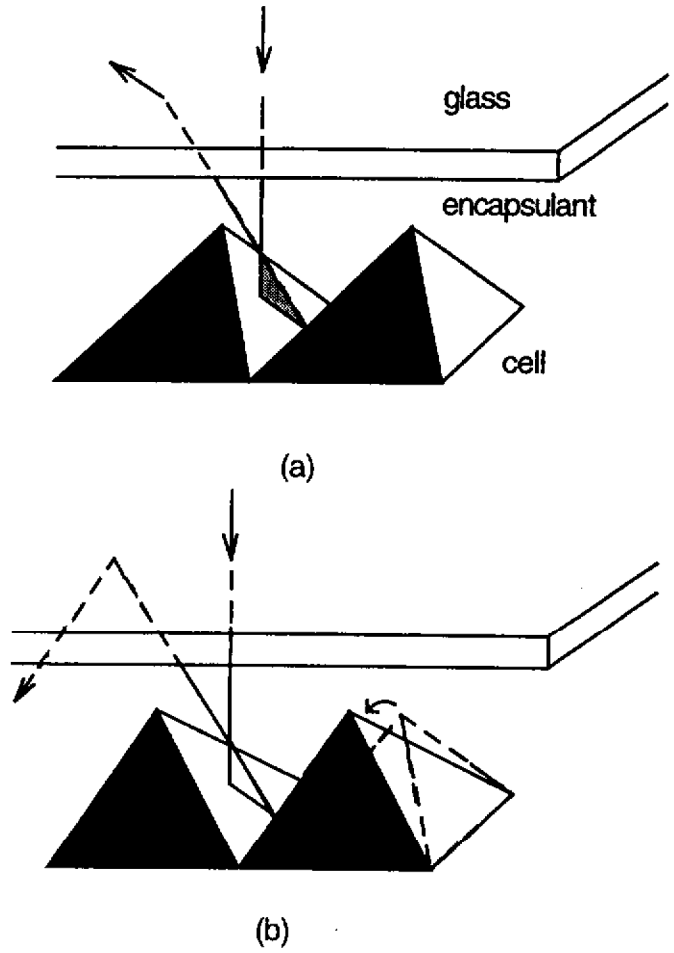


Figure 6.19: Ray paths for pyramidal surface features when encapsulated under glass: (a) normal pyramids; (b) pyramids symmetrically tilted towards one corner.

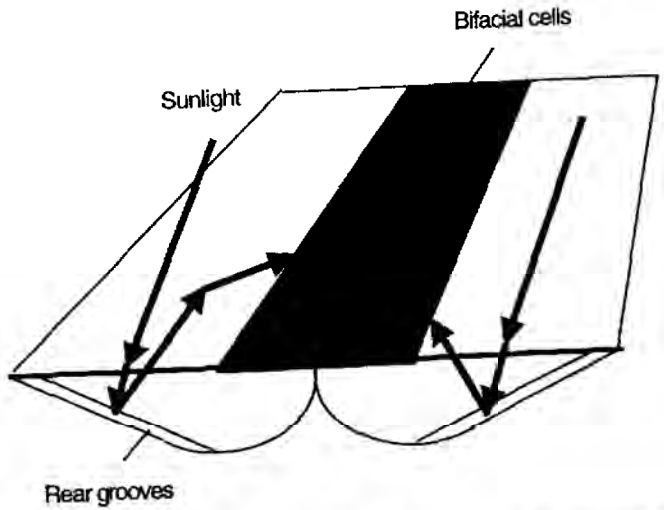


Figure 6.20: Simple static concentrator based on light trapping in "encapsulant".

REFERENCES

6.1 M.A. Green, "Surface Texturing and Patterning in Solar Cells", in Advances in Solar Energy, Vol. 8, M. Prince (editor), American Solar Energy Society, Boulder, 1993, pp. 231-269.

6.2 A. Goetzberger, "Optical Confinement in Thin Si Solar Cells by Diffuse Back Reflectors", 15th IEEE Photovoltaic Specialists Conference, Orlando, 1981, pp. 867-870.

6.3 P. Sheng, "Optical Absorption of a Thin Film on a Lambertian Reflector Substrate", IEEE Transactions on Electron Devices, Vol, ED-31, 1984, pp. 634-6.

6.4 E. Yablonovitch and G.D. Cody, "Intensity Enhancement in Textured Optical Sheets for Solar Cells ", IEEE Transactions on Electron Devices, Vol. ED-29, 1982, pp. 300-305.

6.5 E. Yablonovitch, "Statistical Ray Optics", J. Opt. Soc. Am., Vol. 72, pp. 899-907, 1982.

6.6 P.R. Campbell, "Light Trapping and Reflection Control in a Crystalline Silicon Solar Cell", PhD Thesis, University of New South Wales, June, 1989.

6.7 T. Tiedje, E. Yablonovitch, G.D. Cody and B.G. Brooks, "Limiting Efficiency of Silicon Solar Cells", IEEE Transactions on Electron Devices, Vol. ED-31, pp. 711-716, 1984.

6.8 D. Redfield, "Multiple-Pass Thin-Film Silicon Solar Cell", Appl. Phys. Lett., Vol. 25, pp. 647, 1974.

6.9 P. Campbell, S.R. Wenham and M.A. Green, "Improved Reflection and Light Trapping Using Tilted Pyramids and Grooves", Proceedings, 4th International Photovoltaic Science and Engineering Conf., Sydney, February, 1989, pp. 615-620.

6.10 S.R. Wenham and M.A. Green, "Improved Optical Properties of Solar Cells Using Tilted Geometrical Features", US Patent 5,080,725 (14th January 1992).

6.11 T. Uematsu, M. Ida, K. Hane, Y. Hayashi and T. Saitoh, "A New Light Trapping Structure for Very-Thin, High-Efficiency Silicon Solar Cells", Conf. Record, 20th IEEE Photovoltaic Specialists Conf., Las Vegas, September, 1988, pp. 792-795.

6.12 H. Kiess, J.E. Elper, M.T. Gale, R. Krausbauer, R. Morf and W. Rehwald, "Light Trapping with Submicron Gratings in Thin Crystalline Silicon Solar Cells", 10th E.C. Photovoltaic Solar Energy Conference, Montreux, April, 1991, pp. 19-22.

6.13 P. Campbell and M.A. Green,"Light Trapping Properties of Pyramidally Textured Surfaces", J. Appl. Physics, Vol. 62, pp. 243-249, 1987.

6.14 A.W. Smith and A. Rohatgi, "Ray Tracing Analysis of the Inverted Pyramid Texturing Geometry for High Efficiency Silicon Solar Cells", Solar Energy Materials and Solar Cell, Vol. 29, pp. 37-49, 1993.

6.15 G.A. Landis, "Cross-Grooved Solar Cell", US Patent 4,608,451 (issued August 26, 1986).

6.16 W.H. Deckman, C.R. Wronski, H. Witzke and E. Yablonovitch, "Optically Enhanced Amorphous Silicon Solar Cells", Appl. Phys. Lett., Vol. 42, pp. 968-970, 1983.

6.17 M.A. Green, A.W. Blakers and C.R. Osterwald, "Characterization of High Efficiency Silicon Solar Cells", J. Applied Physics, Vol. 58, pp.4 402-4408, 1985.

6.18 R.A. Sinton, Y. Kwark, P. Gruenbaum and S.M. Swanson, "Silicon Point Contact Concentrator Solar Cells", Conf. Record, 18th IEEE Photovoltaic Specialists Conference, Las Vegas, October 1985, pp. 61-65;

6.19 S.P. Tobin, C.J. Keavney, L.M. Geoffroy and M.M. Sanfacon, "Experimental Comparison of Light-Trapping Structures for Silicon Solar Cells", 20th IEEE Photovoltaic Specialists Conference, Las Vegas, 1988, pp. 545-548.

6.20 P.A. Basore, "Extended spectral Analysis of Internal Quantum

Chapter
9

SURFACE, CONTACT AND BULK PROPERTIES

9.1 INTRODUCTION

In Chapter 7, where bounds on the energy conversion efficiency of silicon solar cells were described, the importance of minimizing surface and bulk recombination became apparent. Experimental approaches to minimizing such recombination are discussed in the present Chapter, for the three types of region found in cells. The first type of region is the ***non-contacted surface***, where thermal oxide passivation has proved to be particularly effective. The second type is the ***contacted surface*** region, where the contacts to the cell are made. The third region is the ***bulk*** of the cell, where recombination rates depend upon both the initial quality of the silicon and subsequent processing.

9.2 SURFACE RECOMBINATION

9.2.1 Interface States and Oxide Traps

Surfaces and interfaces represent rather severe discontinuities in the crystalline structure of silicon. Consequently, high densities of allowed energy levels occur at the surface at energies corresponding to the forbidden gap. One reason for the success of silicon in microelectronics has been the ability to reduce such interface state densities to very low levels by growing a passivating oxide layer.

As the oxide grows, it consumes the underlying silicon. The interface between the oxide and the underlying silicon moves deeper into the bulk. This displacement of the interface to clean regions within the bulk is an important factor contributing to the high levels of passivation provided by this approach. The level of passivation provided, as determined by the density of interface states, can vary over several orders of magnitude depending upon the quality of the associated processing.

Many suggestions have been made as to the origin of the states at the oxide-silicon interface [9.1-9.6]. Since the atoms at this interface are generally well co-ordinated, the remaining structural or stoichiometric deviations lead to defect densities much smaller than the density of interface atoms. The latter ranges from 6.8×10^{14} atoms/cm^2 for a (100) surface to 7.9×10^{14} atoms/cm^2 for a (111) surface [9.7].

Due to statistical disorder, these remaining defects give rise to a quasi-continuous distribution of interface states. Figure 9.1 shows such a distribution broken down into possible components arising from specific defects [9.6].

Contributions to interface states at energies near the conduction and valence band edges are attributed to strained Si-Si bonds (U_T in Fig. 9.1). The other three contributions (U_m, P_L and P_H) are attributed to dangling (unsatisfied) bonds of different types, depending on the number of oxygen atoms involved in the remaining bonds. Different processing and operating conditions can change the relative contributions of the different groups and hence change the shape of the overall distribution, as subsequently discussed. Chemical impurities can also contribute to the interface state distribution. Some impurities, particularly H, Cl and F, are regarded as beneficial while others, such as dopant and metallic impurities, increase interface state densities.

Other defects give rise to allowed states (traps) within the forbidden gap of the oxide. This oxide is amorphous in structure, but is generally characterized in terms of a clearly defined forbidden gap of 9 eV, with the conduction band lying 3.2 eV above that of silicon at the interface and the valence band lying 4.7 eV below that of silicon (Fig. 9.2).

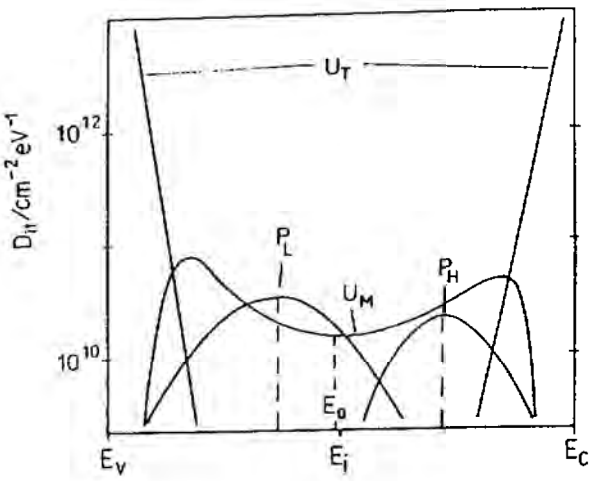


Figure 9.1: Groups of states at the Si/SiO_2 interface and their contribution to the interface state density, $D_{it}(E)$.

U_M - dangling bonds	$Si_3 \equiv Si\text{-}$	$\lvert E\text{-}E_i \rvert < 0.45$ eV
P_L - dangling bonds	$Si_2O \equiv Si\text{-}$	$E_L - E_i - 0.15$ eV
P_H - dangling bonds	$SiO_2 \equiv Si\text{-}$	$E_H - E_i + 0.15$ eV
U_T - strained bonds	$Si_3 \equiv Si - Si \equiv Si_3$	$\lvert E\text{-}E_{v,c} \rvert < 0.15$ eV

The oxide has a fixed positive charge associated with it. According to Ref. 9.6, this charge is related to allowed states in the oxide permanently charged by tunnelling. The sources of these states are localized close to the interface, although their atomic nature is still disputed [9.6]. The corresponding states lie in the upper half of the oxide bandgap. Oxygen vacancies cause hole traps about 6.3 eV above the oxide valence band [9.8].

For solar cell operation, as low an interface density as possible is desirable. The oxides in the best present laboratory silicon cells have densities comparable to gate-quality microelectronic oxides. Careful attention to processing conditions is essential to achieve such quality.

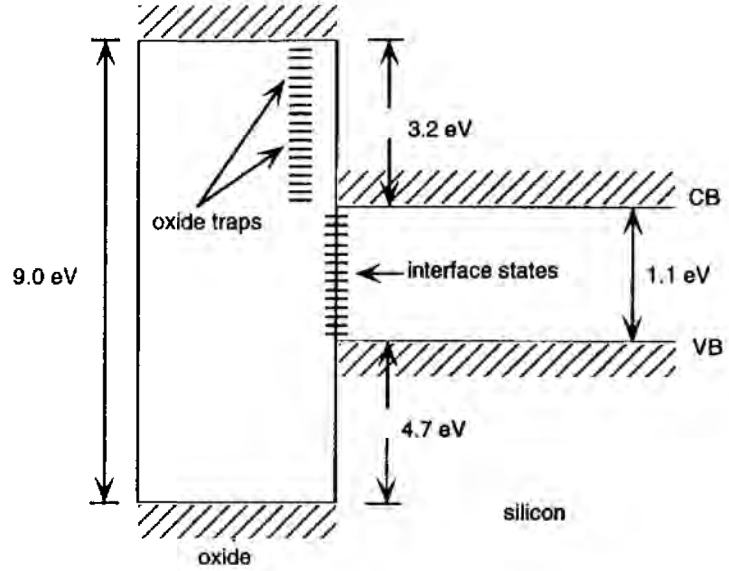


Figure 9.2: The oxide-silicon interface (not to scale; band-bending effects not shown).

Figure 9.3 demonstrates the importance of final processing steps. A good quality oxide was grown and annealed by capping with a layer of aluminium and heating at low temperature. This post-metal anneal (PMA) or ***"alneal"*** is a very effective step in reducing interface state densities. Atomic hydrogen is believed to be generated by the reaction of aluminium with hydroxyl ions in the oxide [9.9]. This hydrogen is then very effective in neutralizing residual defects at the interface [9.10].

In the case shown, the Al layer was either fully or partly removed after this PMA step [9.6], and the device subjected to a low temperature anneal (500°C) either in nitrogen or "forming gas" (FG), which consists of a H_2/N_2 mixture.

Interface state density increased in all cases, attributed to the loss of hydrogen. In the case where the Al was partly removed, this was attributed to loss of hydrogen at the Al edge. The forming gas anneal gives better results than nitrogen annealing. Changes could be reversed by replacing the rear Al and then annealing once more.

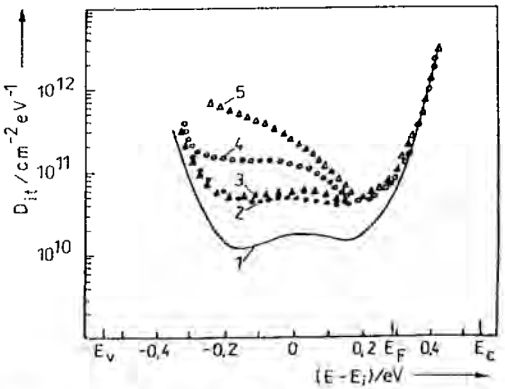


Figure 9.3: Degradation of the interface state density of Al/SiO_2/Si and SiO_2/Si structures by annealing treatments in forming gas (450°C, 30 min.) and dry N_2 (500°C, 5 min). The specimens (thermally oxidized n-Si(111), 10 Ωcm) were well stabilized by a PMA process before initial measurement (curve 1).
Al/SiO_2/Si - annealed in FG (curve 2); annealed in N_2 (curve 3);
SiO_2/Si - annealed in FG (curve 4); annealed in N_2 (curve 5).

Earlier steps in the processing sequence are also important in determining final oxide quality. For example, Eades and Swanson [9.11] report similar midgap interface densities as in the initial curve of Fig. 9.3 after a PMA anneal for oxides that are grown in oxygen and pulled from the furnace in the same ambient. Oxides annealed and pulled in argon after growth gave densities about ten times lower. Introduction of a small amount of chlorine (in the form of HCl in this case) into the oxygen stream also gave good results when pulled in argon.

Other papers compare the effectiveness of different chlorine-based compounds [9.12], while others explore processing optimizations for very thin oxides [9.13].

One issue which has arisen over recent years with these finely tuned oxides concerns their stability under exposure to sunlight, particularly

the ultraviolet component [9.14]. Experiments with UV light, soft x-rays and high energy electron beam irradiation are reported to produce similar results [9.6]:

(i) No degradation is observed at photon or particle energies lower than that required to produce free carriers in the bands of the oxide, either by electron-hole pair generation in the oxide or by excitation (injection) of carriers from the corresponding band in the semiconductor. Holes are much more effective in producing degradation.

(ii) Radiation causes an increase in interface state density as well as in positive oxide charge.

(iii) The increase in both is dependent on the photon or particle dose. The interface density eventually saturates.

(iv) The induced oxide charge decreases logarithmically with time after irradiation.

(v) Annealing in hydrogen can completely restore the interface density to its original value.

From these observations, it is concluded [9.6] that breaking of Si-H bonds is responsible for the interface state generation, in cases where the Si to which the hydrogen was originally attached is connected to three other Si atoms (U_M in Fig. 9.1) or to two Si and one oxygen atoms (P_L). The saturation density of the generated interface states therefore would be a measure of the total density of Si-H bonds at the unirradiated interface (estimated as 8.9×10^{12} states cm^{-2} eV^{-1} [9.6]).

Interestingly for solar cells, which frequently use textured surfaces, recent work suggests a direct correlation between interface density and the stress (or strain) in the grown oxide layer [9.15]. This stress arises from differential thermal contraction during cooling, and would be expected to have areas of concentration for a textured surface. Any additional elastic stress due to low temperature (<500°C) deposition and processing of metal or dielectric films after the high temperature (>800°C) oxidation and annealing was not found to influence the interface density [9.15]. It was concluded that the density of defects is associated with processes inherently non-elastic in nature, e.g., localized plastic deformation near the interface which can relax oxide

stress. Another recent development has been the correlation of interface density with the microroughness of the interface. One paper [9.16] suggests that micro-protrusions are reduced with appropriate oxide annealing conditions, while another [9.17] shows a strong correlation between final quality and initial microroughness.

Surface damage [9.18] or foreign impurities [9.19] can contribute additional interface states, often referred to as ***extrinsic interface states***. For example, Fig. 9.4 shows measured interface state densities as a function of surface dopant concentration, both before and after an "alnealing treatment" [9.20]. Interface state densities are low and virtually independent of the doping levels until these levels reach the 10^{16}-10^{17}/cm^3 range. They then increase with further increase in doping level as extrinsic states begin to dominate. More recent work [9.21] confirms this general trend.

Interestingly, from Fig. 9.4, "alnealing" produces beneficial results even for doped surfaces, although these benefits seem to be smaller for the highest phosphorus doping levels shown. Solar cells with phosphorus doped surfaces have been shown to be stable under UV radiation which would severely damage cells with only lightly doped surfaces. Since this UV damage is explained in terms of Si-H bonds, a lower sensitivity of the phosphorus doped surfaces to hydrogen would be consistent with their demonstrated stability to UV light exposure.

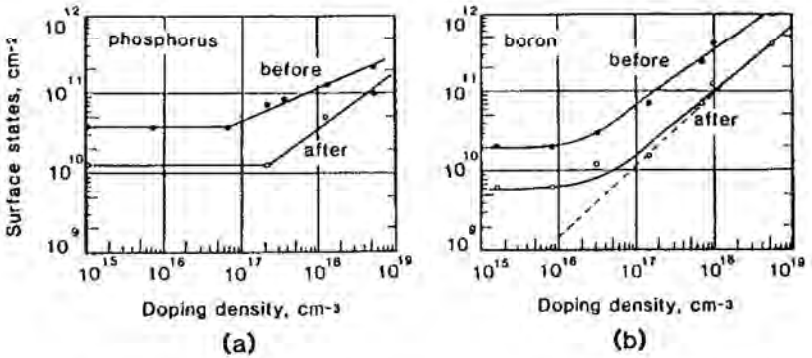


Figure 9.4: Surface state (interface trap) density versus doping level at an oxide passivated surface for (a) phosphorus-doped (n-type) and (b) boron-doped (p-type) surfaces. Results are shown before and after alnealing at 450°C (after Snel [9.20]).

9.3 RECOMBINATION AT INTERFACE STATES

9.3.1 Independent, Discrete Interface States

In the usual modelling of interface states, each state is associated with a single level in the forbidden gap, rather than with multiple levels associated with different charged states of the seminal defect [9.22]. Moreover, these levels are assumed independent, i.e., carriers can make transitions between these energy levels and the valence and conduction bands but not to other interface state levels [9.23]. This is a good approximation given the low density of interface states compared to surface atoms, as previously noted. This suggests that the seminal defects are physically well separated compared to the density of surface atoms. The theory of defect recombination, as given by Eq. (5.19), applied to this situation gives a recombination rate per unit area, U_A:

$$U_A = \frac{S_{no} S_{po} (n_s p_s - n_1 p_1)}{S_{no} (n_s + n_1) + S_{po} (p_s + p_1)} \qquad (9.1)$$

where $S_{no,po}$ are surface recombination velocity parameters given by:

$$S_{no,po} = \sigma_{n,p} \langle v_{th,tp} \rangle N_{it} \qquad (9.2)$$

N_{it} is the interface state density (states/cm^2), σ_n and σ_p are capture cross-sections for electrons and holes, n_s and p_s are carrier surface conçentrations and n_1 and p_1 depend on the energy level within the gap (Section 5.3.4) with $n_1 p_1 = n_i^2$ in general. (Optical generation through interface states can be treated as in this section, although this is assumed to be a weak process [9.24]).

9.3.2 Independent, Continuous States

The previous expression can be simply extended to a continuous distribution of states across the forbidden gap, if these are assumed independent. N_{it} in this case is replaced by D_{it} the density of states/unit area/unit energy (states/cm^2 - eV). U_A is

recombination/unit area/unit energy and must be integrated from E_V to E_C to find U_{AC}, the recombination rate/unit area.

9.3.3 Equal Capture Cross-Sections

When $\sigma_n = \sigma_p$, and assuming $v_{tn} = v_{tp}$, Eq. (9.1) for discrete states reduces to:

$$U_A = \frac{S_{no,po}(n_s p_s - n_1 p_1)}{(n_s + p_s + n_1 + p_1)} \tag{9.3}$$

Assuming $\sigma_n N_{it}$ (= $\sigma_p N_{it}$) does not vary as rapidly with energy as n_1 and p_1, i.e., not more rapidly than $(exp\ [\Delta E/kT])$, U_A will have its maximum value when n_1 and p_1 are both small, i.e., for states near mid-gap.

For continuous states under the same conditions with n_1 and p_1 small:

$$U_{AC} = \frac{S'(n_s p_s - n_i^2)}{(n_s + p_s)} \tag{9.4}$$

where

$$S' = \int \sigma_n \langle v_{tn} \rangle N_{it}\, dE \tag{9.5}$$

with the integral taken over all states where n_1 and p_1 are small (these will all lie within $\pm (kT/q) \ln ((n_s + p_s)/n_i)$ of the Fermi-level in intrinsic material, i.e., close to mid-gap).

For the $n_s p_s$ product fixed, (e.g., a given quasi-Fermi level separation or applied voltage), both Eqs. (9.3) and (9.4) predict a maximum recombination rate when $n_s = p_s$. This is the basis of a common assumption that peak surface recombination occurs when surfaces are depleted [9.25].

9.3.4 Constant Capture Cross-Section Ratio

When σ_n/σ_p is a constant at each energy within the forbidden gap, with otherwise the same assumptions as in the previous section, U_{AC} becomes:

$$U_{AC} = \frac{S'(n_s p_s - n_i^2)}{(n_s + \frac{\sigma_p}{\sigma_n} p_s)} \tag{9.6}$$

with S' defined as in Eq. (9.5) but the integral taken from $-(kT/q) \ln ((\sigma_n n_s/\sigma_p + p_s)/n_i)$ to $+(kT/q) \ln ((n_s + \sigma_p p_s/\sigma_n)/n_i)$ referred to the Fermi-level in intrinsic material. When the $n_s p_s$ product is fixed, this predicts a maximum in the recombination rate occurring when $n_s = (\sigma_p/\sigma_n) p_s$.

The corresponding offset can modify the argument that surface depletion increases surface recombination and that accumulation and inversion decrease recombination, although high levels of accumulation or depletion will remain the most desirable.

9.3.5 Experimental Interface Densities and Capture Cross-Sections

Experimental interface densities are very sensitive to processing conditions as previously mentioned, as are capture cross-sections.

Figure 9.5 shows experimental interface densities as measured for growth conditions producing laboratory cells of reasonable performance [9.26] while Fig. 9.6(a) shows the corresponding electron and hole capture cross-sections for energies where they can be measured (other growth conditions from those of Fig. 9.5 are also shown). Note that the electron capture cross-section is higher than the hole near the small range of energies where both can be measured. This is a common, but not universal result. Additional measurements for oxides grown in other laboratories shown are in Fig. 9.6(b).

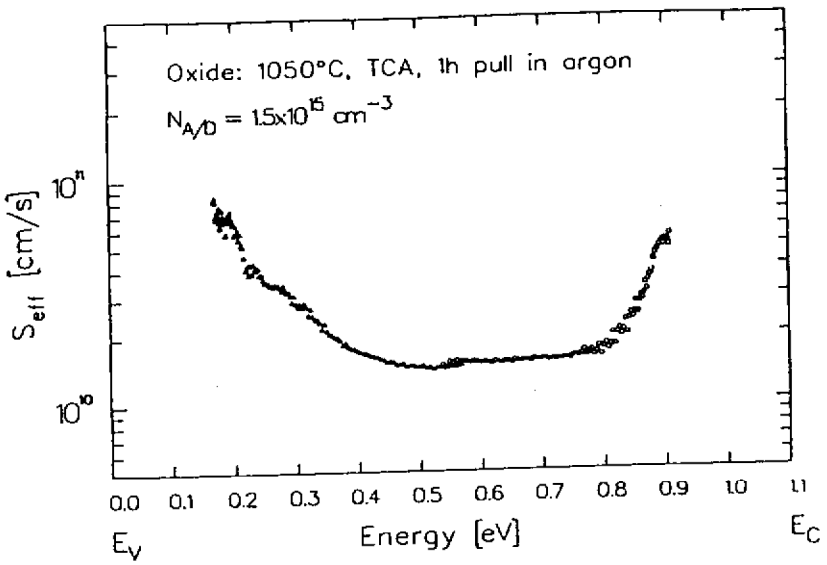


Figure 9.5: Interface state density at the Si-SiO_2 interface measured on p-type (lower half of the gap) and n-type (upper half) MOS samples. (Dry oxidation at 1050°C, 2% TCA, 1 h post-oxidation anneal in argon, Al-metallization, post-oxidation anneal in forming gas) (after [9.26]).

Combining the distribution of Fig. 9.5(a) with capture cross-sections such as in Fig. 9.6(a) allows calculation of the surface recombination velocity as a function of different surface conditions, in principle, as described elsewhere [9.26, 9.27]. One problem with this approach is that it assumes that, for each energy level within the gap, there is only one type of state with its distinctive capture cross-section values. From Fig. 9.1, it is apparent that, at any given energy, there may be states arising from different physical sources which may have different capture cross-sections. The techniques for measuring capture cross-sections used to deduce figures such as Figs. 9.6(a) and (b) do not distinguish between these possibly different states. Figure 9.7 shows the measured value of surface recombination velocity as a function of injection level for high quality oxides compared to values calculated in the way described.

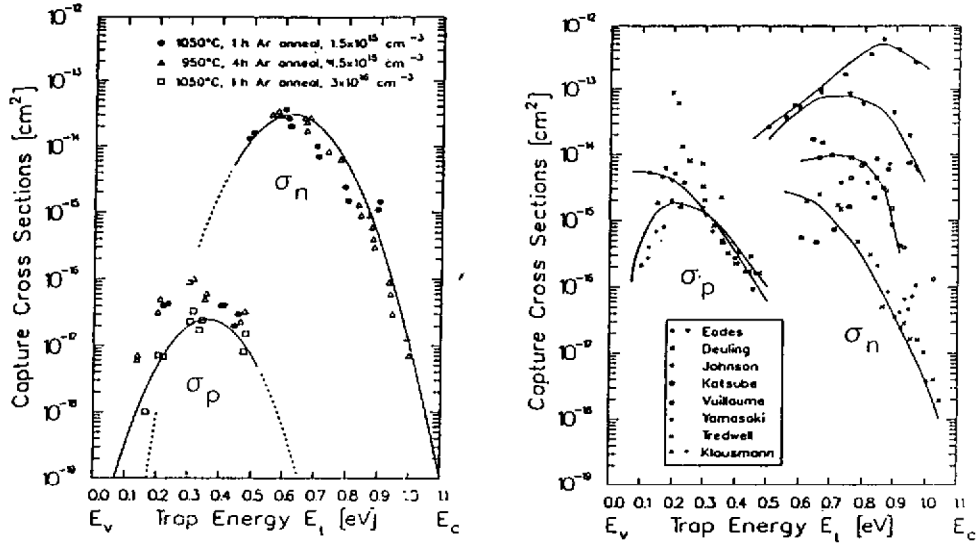
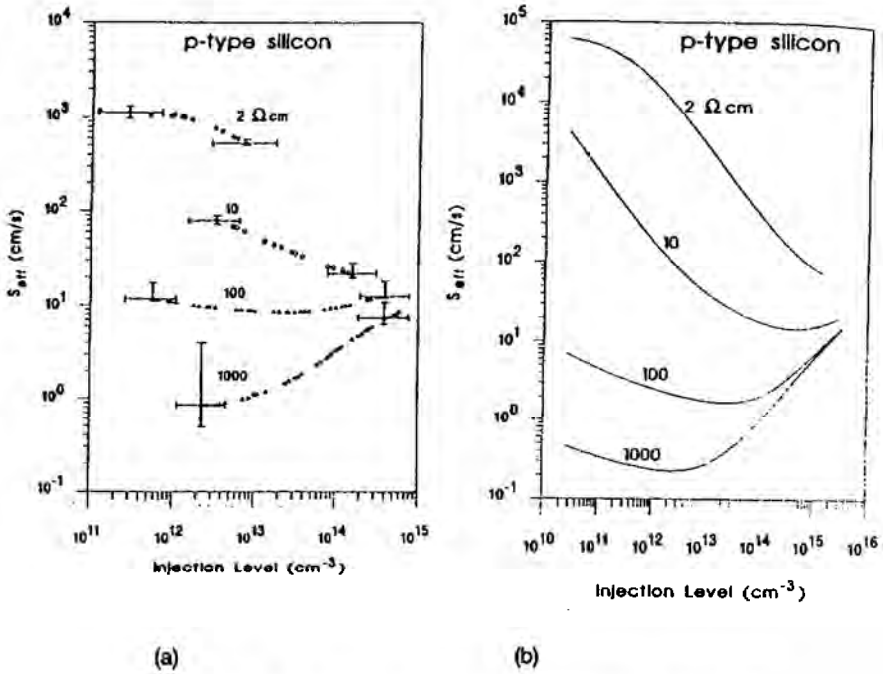


Figure 9.6: (a) Electron and hole capture cross-sections at the Si-SiO_2 interface measured by small pulse DLTS for different oxidation schedules and doping densities; (b) Survey of published data for the electron and hole capture cross-sections at the Si-SiO_2 interface. The solid lines are guides to the eye (Eades [9.27], Deulin [9.28], Johnson [9.29], Katsube [9.30], Vuillaume [9.31], Yamasaki [9.32], Tredwell [9.33], Klausmann [9.34]) (after [9.26]).

An interesting set of results has been generated in an experiment where the injection level was held constant and the electrostatic conditions at the surface were varied. These results are shown in Fig. 9.8. This shows the effective surface recombination velocity as a function of the surface electron concentration (n_s) divided by the corresponding surface hole concentration (p_s), a measure of the electrostatic conditions at the surface [9.36].



(a) (b)

Figure 9.7: (a) Measured surface recombination velocity for oxidized p-type wafers of different resistivity as a function of injection level; (b) corresponding calculated values.

The effective surface recombination velocity is very low when the surface electron concentration is low, corresponding to accumulation at the surface. At the other extreme of very high electron surface concentration, corresponding to inversion, the effective surface recombination velocity is also very low. A peak in effective surface recombination velocity is reached at surface conditions intermediate between these extremes.

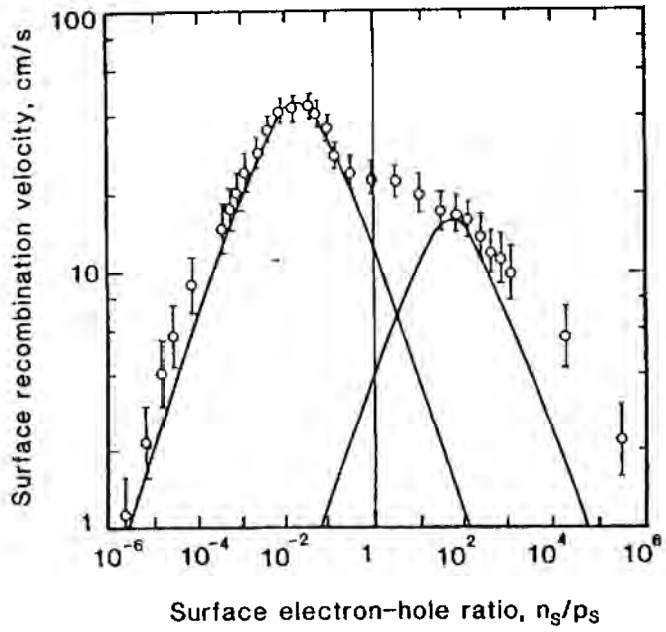


Figure 9.8: Measured effective surface recombination velocity for p-type silicon-oxide interface as a function of surface potential as given by the surface electron/hole ratio (n_s/p_s). The bulk injection level was such that n_b was equal to $3 \times 10^{16}/cm^3$ and p_b was equal to $5.5 \times 10^{16}/cm^3$. The surface recombination velocity is that referred to n_b rather than n_s. The solid lines are theoretical curves for states with two different capture cross-section ratios (σ_n/σ_p) (after Yablonovitch et al. [9.36]).

An understanding of these results can be obtained by referring to the analysis of Section 9.3.4. Here, it is shown that a constant ratio of capture cross-section should produce a surface recombination rate (and hence effective surface recombination velocity) which peaks at an n_s/p_s ratio corresponding to the ratio of capture cross-sections. The experimental curves of Fig. 9.8 can be roughly broken down into two sub-curves as indicated by the solid lines, each sub-curve corresponding to a set of surface states with a given capture cross-section ratio. This suggests that recombination at the surface studied

was dominated by two groups of states, one with the electron capture cross-section about 100 times that of holes, with the other component of the distribution due to states with hole capture cross-sections about 100 times that of electrons. Electrostatically charged states typically have this large difference between electron and hole capture cross-sections, suggesting that the first group of states might well be positively charged and attractive to electrons (donors) while the second group may be negatively charged and attractive to holes (acceptors). Alternatively, but less likely, the states may lie within the bandgap at energies close to the conduction band or valence band, respectively, making it easier for the respective carriers to make the transition due to the smaller amount of energy to be dissipated in the transition.

Rather interestingly, the results give no information about the energy location of the states involved in producing the measured surface recombination. States contributing to either of the two peaks might lie over a range of different energies but have something in common such as the electrostatic attraction or repulsion of the respective carriers.

The practical conclusion from Fig. 9.8 is that conditions near flat band are not particularly attractive in terms of minimizing surface recombination (flat band occurs at an n_s/p_s ratio of 0.55 in the present example). Instead, the more extreme conditions of either strong inversion or strong accumulation are desirable. Just how far recombination can be reduced by going to such extremes has also been investigated in the work previously cited. Figure 9.9 shows the measured contribution of surface recombination to the saturation current density of a device as a function of electron or hole surface concentration. This saturation current density contribution is more readily accessible experimentally than the surface recombination velocity, which depends on knowing minority carrier concentrations at the surface which are often difficult to determine experimentally.

The interesting point about Fig. 9.9 is that there is a limit to how low the saturation current density contribution from the surface can be reduced by this approach. Theoretically, this contribution should continue to decrease as the respective surface carrier concentration increases. Experimentally, there is a definite saturation, in this case, to current density values of about 8 fA/cm^2. The reason for this saturation has not been definitively identified. One possibility is that it is due to tunnelling through the very thin electrostatically induced

layers which correspond to the highest surface carrier concentrations. The values of Fig. 9.9 are probably the lowest current saturation density contribution that have been experimentally measured for silicon surfaces. The only option for reducing further would seem to be either to combine this electrostatic action with doping which may prevent the saturation observed in Fig. 9.9 or to reduce surface state densities by improved processing techniques.

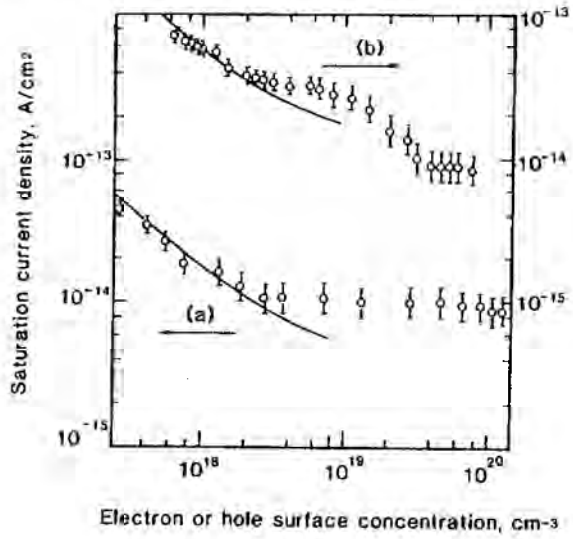


Figure 9.9: Measured values of the saturation current density associated with recombination at the p-type silicon-oxide interface as a function of the electrostatically induced (a) electron and (b) hole concentrations at this interface. The solid curves are theoretical curves, based upon a particular band-gap narrowing model (after Yablonovitch et al. [9.36]).

9.4 CONTACT RECOMBINATION

Metallic contacts to the cell are required to transfer the generated current to an external load. At the interface with silicon, it is known from experiment that metals induce a barrier to majority carriers, as shown in Fig. 9.10(a). Contrary to simple contact theories, this behaviour means that the contact potential between silicon and metals

is not given by the difference in work function between the metal and silicon. An overriding "pinning" effect is at work when the metal is in close proximity to silicon. Although a number of theories have been developed to explain this effect [9.37-9.39], there is still no universal agreement as to its physical origin.

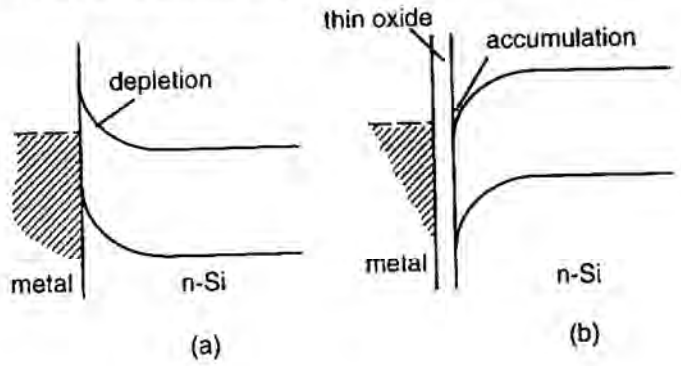


Figure 9.10: (a) Metal-silicon contact showing Schottky barrier formation; (b) metal-thin insulator-semiconductor (MIS) contact with metal work function chosen so as to cause accumulation of the semiconductor in the contact region.

The barrier to majority carrier flow gives rise to an undesirable contact resistance. To bring the contact resistance down to useable values, high doping levels are required in the semiconductor immediately under the contact. This decreases the width of the barrier region and allows majority carriers to flow across it in appreciable quantities via quantum-mechanical tunnelling. Since there is no barrier to minority carrier flow, such contacts represent regions of very high surface recombination velocity. In fact, at such contacts, minority carriers could be expected to recombine at a rate which was determined solely by their rate of arrival. This rate would be close to the scattering-limited velocity in silicon of about 10^7cm/s. Assigning this value to the recombination velocity of the contact would be consistent with this arrival-rate limited model.

Such high recombination velocities are, according to Chapter 7, not consistent with producing the maximum possible cell performance. For example, if the contacts are made to thin doped layers, as indicated

by Fig. 9.11(a), the corresponding contribution to the saturation current density of the cell can be calculated very generally as:

$$I_{oc} = qn_i^2 A_c / \int (N_e / D_B)\, dx \qquad (9.7)$$

where A_c is the contact area, N_e is the effective doping level at a distance, x, away from the contact, D_B is the corresponding minority carrier diffusion coefficient, and the integral is taken over the thin doped layer. This expression shows that, to minimize this saturation current contribution, doping levels should be high and the doped layer should be thick. Neither of these conditions is consistent with optimization of the passivation of non-contacted areas.

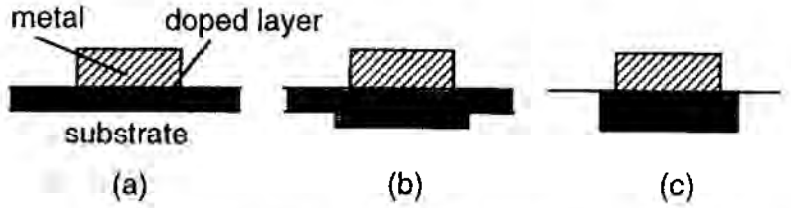


Figure 9.11: (a) Metal contact to a thin doped layer; (b) incorporation of a second, more substantially doped region into the contact area; (c) passivation of contact recombination by a heavily doped region where doped surface layers are not used for surface passivation.

It follows that the incorporation of a second, dedicated doped region under the contact, as shown by Fig. 9.11(b), leads to better performance. For cells in which undoped surface passivation is used, only the heavily doped region would be required, as shown by Fig. 9.11(c).

Tables 9.1 and 9.2 give an indication of desirable diffusion conditions in contacted and non-contacted areas [9.40]. To determine the saturation current densities shown, the diffused surface was initially passivated with a high quality oxide. After measurement in this condition, the oxide was removed, an aluminium contact deposited and the measurement repeated.

Table 9.1: Saturation current density of phosphorus-doped surface diffused regions (after Kane and Swanson [9.40]).

Sheet Resistivity	Junction Depth	Surface Doping	Saturation Current Density (pA/cm^2)	
(Ω/square)	(μm)	(/cm^3)	Passivated	Contacted
9.0	5.8	5.0×10^{19}	0.45	0.50
57.2	3.6	1.2×10^{19}	0.10	1.10
75.3	1.8	2.0×10^{19}	0.13	1.70
370	1.2	2.5×10^{18}	0.08	1.70
890	1.3	1.0×10^{18}	0.01	7.00

Table 9.2: Saturation current density of boron-doped surface diffused regions (after Kane & Swanson [9.40]).

Sheet Resistivity	Junction Depth	Surface Doping	Saturation Current Density (pA/cm^2)	
(Ω/square)	(μm)	(/cm^3)	Passivated	Contacted
5.3	4.8	7.0×10^{19}	0.35	0.42
37	2.1	3.6×10^{19}	0.07	0.57
63	3.0	1.3×10^{19}	0.09	1.10
240	1.1	5.4×10^{18}	0.13	1.00
463	1.2	1.3×10^{18}	0.06	1.10

These tables show that contact passivation as shown in Fig. 9.11(b) contributes a minimum saturation current density of about 0.5 pA/cm^2 [9.40]. This is about ten times higher than the Auger limit upon the contribution from such a region which is calculated, using Eq. (7.1) to be 0.06 pA/cm^2. For such contacts to have a negligible effect upon the Auger limiting performance, they must cover a fraction, f_c, of the surface of the cell which is given by:

$$f_c < C_B N_B W_B / \sqrt{C_{BC} D_{BC}} \qquad (9.8)$$

for a cell in low injection, and by:

$$f_c < \left[(J_L/q)(C_n + C_p)^2 W_B^2 \right]^{1/3} / (D_{BC} C_{BC})^{1/2} \qquad (9.9)$$

for a cell in high injection. Here, the subscript, BC, refers to values in the contact region, and the other terms are defined in Chapter 7. The other constraint on f_c is that it should be sufficiently high that contact resistance is not a problem. This can be expressed mathematically as:

$$f_c >> V_{oc} / (J_L \rho_c) \qquad (9.10)$$

where ρ_c is the specific contact resistance of the contact. It appears that the conflicting constraints on the contact area can be satisfied simultaneously in the Auger limit. However, if the bulk region performance approaches the Auger limit, while that of the contact region does not, some difficulty could arise in satisfying both criteria.

Another approach to reducing the effects of contacts is to use a contacting method which, unlike the normal metal-to-semiconductor contact, has a low recombination velocity at its interface with silicon. Although metals deplete the underlying silicon due to the anomalous "pinning" effects previously mentioned, the insertion of a thin layer between the metal and semiconductor removes these anomalous effects. The conditions in the semiconductor under the oxide then become sensitive to the work function of the metal, in agreement with simple contact theories. To make a low resistance contact, a metal can be chosen that accumulates majority carriers in the contact region, as shown by Fig. 9.10(b), rather than depleting them.

The normally insulating oxide layer can be made so thin that the current can flow across it via quantum-mechanical tunnelling. It is not necessary that this should be the only mechanism for current transport for this approach to work [9.41], although tunnelling is an efficient and reliable process for current transport across such thin oxides, and is likely to play an important role. Referring to Fig. 9.10(b), accumulating majority carriers under the contact means that minority carrier concentrations under the contact will be depleted. This greatly suppresses minority carrier recombination whether it occurs at surface states at the oxide-silicon interface in the same way as at the non-contacted surfaces of the previous section, or by tunnelling through the oxide to the metal. On the other hand, the accumulated majority

carrier concentration facilitates the transport of these carriers across the oxide. The effective contact resistance of this approach depends both upon this concentration and upon the thickness of the thin oxide layer. Although contact resistances as low as the intimate metal-semiconductor approach have not yet been demonstrated using this approach, this is offset by the lower contact recombination velocity, which makes larger contact areas feasible.

This approach was successfully used to produce the first solar cells having an open-circuit voltage higher than 675 mV [9.42]. A more recent development has been to replace the metallic layer by a layer of degenerately doped polysilicon [9.43-9.45] or semi-insulating polysilicon (SIPOS) [9.46]. The latter is polysilicon with an appreciable quantity of incorporated oxygen. Although frequently no deliberate oxide growth step is involved, the presence of a thin interfacial oxide is an important means of obtaining the optimum performance from these approaches [9.46, 9.47]. Hence, they can be regarded as variations upon the metallic layer approach previously described. Advantages include the ability to process at high temperatures after the "metallic" region is deposited, the ability to dope the underlying silicon from the "metallic" region, and the fact that the "metallic" layer is at least partially transparent to sunlight. The disadvantages include a more restricted range of work functions from which to choose and possibly more sophisticated processing requirements.

A more recent approach for contact passivation relies on heterojunctions formed between the bulk silicon and deposited layers of hydrogenated amorphous silicon or microcrystalline silicon [9.48]. The advantage of this approach is that quite reasonable levels of passivation can be obtained using very low processing temperatures. There are situations, such as in the case of thin film cells deposited onto a foreign substrate, where such low processing temperatures could be advantageous.

9.5 BULK RECOMBINATION

Intrinsic limits upon base recombination have been discussed in some detail in Chapter 7. However, in almost all of the silicon solar cells fabricated up to the present time, the bulk recombination rate is not determined by intrinsic processes, but by defect-assisted recombination. Defects are not only present in the "as-grown" bulk

material, but can be generated or introduced during subsequent processing.

Such defects are generally categorized as ***point, line, area*** or ***volume*** defects depending on their spatial characteristics. Some examples of each type are shown in Fig. 9.12.

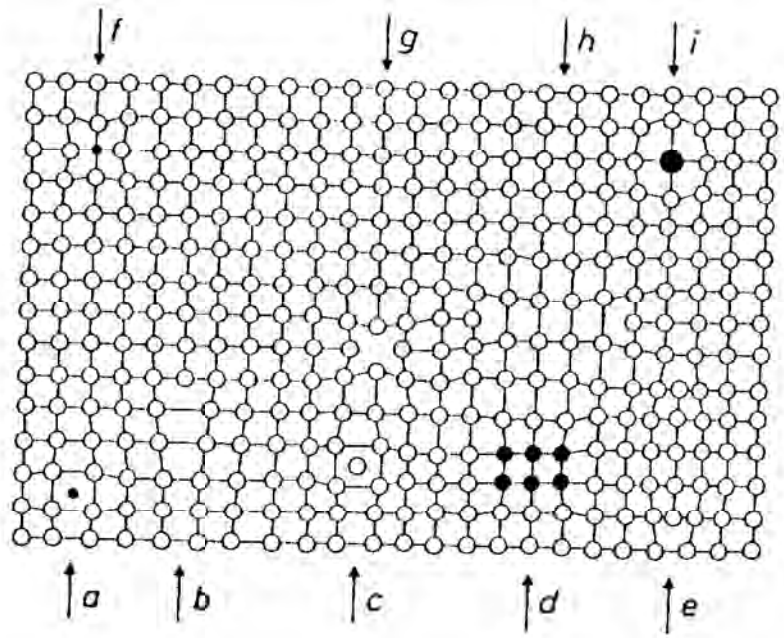


Figure 9.12: A pictorial representation of the various types of point, line, area and volume defects: (a) foreign interstitial; (b) dislocation; (c) self-interstitial; (d) precipitate; (e) extrinsic stacking fault and partial dislocation; (f) foreign substitutional; (g) vacancy; (h) intrinsic stacking fault surrounded by a partial dislocation; (i) foreign substitutional (after [9.49]).

Examples of ***point defects*** are self-interstitials, vacancies and foreign substitutional or interstitial atoms [(*c*), (*g*), (*i*), (*f*) and (*a*) above, respectively]. Dislocations are an example of ***line defects*** [(*b*) above]. As well as stacking faults [(*e*) and (*h*) above], grain boundaries and twin planes are examples of ***area defects*** (a twin plane is a plane about which atomic distributions appear as mirror reflections either side of the plane). Precipitates [(*d*) above] and impurity clusters are examples of ***volume defects***.

In principle, most of these defects can be avoided with sufficient care. However, some are unavoidable. An example of the latter is the group of intrinsic thermal point defects (self-interstitials, vacancies) which are present in silicon at increasing concentrations as the temperature increases [9.50]. During the growth of high-quality dislocation-free silicon from the melt, these thermal point defects supersaturate the silicon as it cools, and then condense to form microdefects. The latter take the form of small dislocation loops and related point defect clusters. They are generally referred to as swirl defects since they are spirally distributed about the longitudinal axes of the cylindrical crystals produced using the Czochralski or float-zone processes.

Swirl defect formation depends upon the impurity content of the crystal (particularly carbon) and upon growth conditions such as the growth and rotation rates, the crystal diameter, the cooling rate from the solidification temperature, and the crystal growth ambient [9.50].

In high quality wafers, contaminants other than oxygen and carbon can be kept to very low levels; levels below the detection capabilities of even very sensitive techniques such as neutron activation analysis [9.51]. In Czochralski-grown crystals, oxygen is generally present in concentrations of the order of $10^{18}/cm^3$. This oxygen originates from the quartz crucible which contains the molten silicon from which the crystal is grown. The oxygen concentration is highest in the regions which form first (the seed end of the crystal) and lowest in the final growth areas (tang end). The radial distribution of oxygen follows the spiral pattern found for swirl defects, as do many crystal properties. Carbon originating from the heating element, susceptor, and silicon feedstock is generally present in concentrations of the order of $10^{16}/cm^3$, with the highest concentration being found in the tang end of the crystal (i.e., the opposite distribution to that of oxygen). In float-zone silicon, both impurities are generally present in the latter concentration range.

Both oxygen and carbon are relatively inactive electrically, considering their high concentrations. In Czochralski crystals, oxygen can make its presence felt by forming donors in concentrations of up to $10^{16}/cm^3$ after prolonged heating at temperatures of between 300 and 500°C. Normally, oxygen occupies interstitial positions in the silicon lattice. Donor formation is attributed to a change in the location of the oxygen to a substitutional position, and several possible mechanisms have been suggested for this transformation [9.50]. There is some evidence that this thermal donor formation results in an increase in the minority carrier lifetimes in the crystal [9.51]. This is presumably due to the complexing of lifetime-reducing acceptors, such as Ca and Fe, with the thermal donors [9.50]. Heating to higher temperatures eliminates these donors. At temperatures greater than 1000°C, there are irreversible changes in the crystal, in that donors are not formed upon subsequent heating at 450°C. This is attributed to the precipitation of oxygen, in the form of SiO_2, within the bulk crystal [9.50].

These effects of oxygen are reasonably well characterized. Given the relatively large concentrations of oxygen and carbon, and the changes which occur depending upon the precise way in which they are incorporated into the silicon lattice, there is a potentially enormous range of subtle effects due to these elements, influenced by the thermal history of the crystal. Additional dimensions are added to the range of possibilities by their interaction with each other, with thermal point defects, with crystallographic defects, and with dopants, as well as by their interaction with other impurities and by the corresponding interactions of those other impurities. Some interactions of interest include evidence for the role of oxygen in the nucleation of swirl defects [9.50], and the formation of haze or saucer-pit defects [9.53] due to the interaction of silicon self-interstitials and metallic impurities.

Processing induces additional changes in the bulk properties. Oxidation of silicon surfaces is a very effective way of passivating those surfaces, as discussed in the previous section. Dislocations and stacking faults can be introduced into silicon wafers during oxidation [9.50]. Dislocations can arise from the thermal stresses generated during wafer heating to, and cooling from, the oxidation temperature. Slower heating and cooling can alleviate this problem.

Stacking faults arise from excess silicon self-interstitials generated during oxidation. These excess atoms can condense on a suitable

nucleation site to form extra planes of atoms in localized areas within the crystal structure. Scratches on the surface are common nucleation sites, as are swirl defects and impurity precipitates. Inert atmosphere annealing after oxidation, found to be of benefit in reducing surface state densities, is also effective in shrinking stacking faults. The concentration of silicon vacancies at the oxide-silicon interface can be increased by the addition of small amounts of halogens to the oxidizing ambient [9.50]. This counteracts the tendency to form the excess self-interstitials responsible for stacking faults.. Incorporating a small percentage of HCl or other halogen sources into the oxygen stream not only has beneficial effects in this respect but, as noted in the previous section, can reduce surface state densities. An additional benefit is that halogens in the oxygen stream react with transition metal impurities within the oxidation furnace and form volatile halides. These are carried out of the oxidation zone by the gas stream and are deposited in cooler parts of the oxidation furnace. This reduces the level of contamination of the wafer by such impurities during the high temperature oxidation step.

Dopant diffusion can also produce similar defects, not only due to the oxidation process which normally accompanies diffusion, but also due to the creation of additional silicon self-interstitials by the dopant diffusion process itself. Dislocations can also be formed at high doping levels due to stresses which arise from the mismatch of the dopant atom to the silicon lattice. Excess dopant atoms can also be precipitated in dopant-rich compounds in the surface region at high dopant concentrations.

During processing, contamination by metallic impurities is also possible. A detailed study of impurity incorporation into silicon during normal processing indicates that most contamination occurs during high temperature furnace treatments [9.51]. This contamination comes from impurities which diffuse through the quartz tubes, normally used in such furnaces, from other components of the diffusion system [9.53]. During oxidation for one hour at 1000°C in a conventional microelectronics furnace, it was found that Cr, Fu, Fe, Na, Ni, Ta, Zn and Zr were introduced at average concentrations ranging from 2×10^{13} to $3 \times 10^{14}/cm^3$ for each impurity [9.54]. One approach to minimizing such contamination is to clean the tube frequently by passing halogen-containing gas. This serves to deplete the above impurities temporarily. In one study, copper contamination increased tenfold over a 48 hour period following HCl cleaning [9.55].

This indicates that very frequent cleaning is necessary for this approach to be effective. The use of a double-walled tube with HCl continuously circulating in the outer zone has been shown to be very effective in reducing contamination of this type [9.54]. Furnace components of improved purity can also be expected to reduce contamination levels in the future [9.56].

Once within the crystal, impurities can act in isolation as recombination centres or can be precipitated at crystallographic defects, with the combined defect acting as an efficient recombination site. Once precipitated, it is generally considered more difficult to remove the impurity by using the gettering approaches described in the following section.

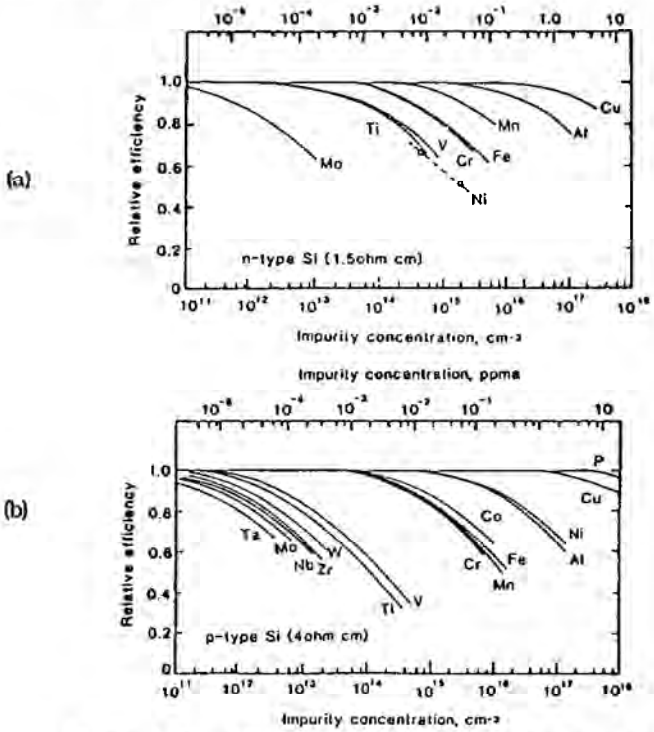


Figure 9.13: Effect of the deliberate inclusion of different concentrations of impurities upon the performance of solar cells fabricated on (a) n-type substrates (after Davis et al. [9.57]); and (b) p-type substrates (after Davis et al. [9.57])..

Figure 9.13 shows the effect of various metallic impurities upon the performance of cells fabricated, using conservative processing sequences, on n-type and p-type substrates [9.57]. While some impurities can be tolerated in quite large concentrations, others will decrease cell efficiency by a significant amount even when present in concentration levels of the order of parts per billion.

9.6 GETTERING

There are two conceptually different approaches to obtaining good bulk properties in completed devices. The first is to start with high quality material and to avoid defect formation and the introduction of contaminants during processing. As is apparent from the last section, this approach can present problems, particularly in the relatively rugged environment consistent with the high-volume production of inexpensive terrestrial cells. However, it may be consistent with the production of high quality concentrating and space cells. The second approach is to accept that cell substrates will be subjected to contamination and defect formation during processing, and therefore develop processing sequences which are capable of extracting or neutralizing contaminants and defects. Even in a high quality microelectronics processing environment, both of these approaches are usually pursued in parallel.

One approach of the second type, which is widely used in microelectronics, is ***intrinsic gettering*** [9.58]. Starting with an oxygen-rich wafer, oxygen is depleted from the surface regions by out-diffusion at high temperatures. The oxygen which remains in the central regions of the wafer is then precipitated out in the form of SiO_2. These precipitates in the wafer centre then act as gettering sites during subsequent device processing. This results in very high quality material in the surface layers, but poor quality material towards the centre of the wafer cross-section (Fig. 9.14). This approach is not suitable for photovoltaics, where high quality material is required throughout the entire volume.

The alternative is to use ***extrinsic gettering***. This involves the deliberate introduction of gettering sites on one surface of the wafer, generally the rear surface. During high temperature treatments, defects in the wafer which are affected by the gettering treatment will diffuse to the gettering sites, where they are held or subsequently

removed from the wafer. A third process is ***chemical gettering***. An example has already been given in the previous section where the use of halogens in the gas stream was mentioned. Metals near the wafer surface react during such treatments and form halides which are volatile at the temperatures involved. This leaves the surface depleted of the metallic impurities and causes it to act as a sink for the impurities which lie deeper within the wafer. A thin oxide (10-20 nm) should be present on the wafer surface during this treatment in order to prevent the pitting action of the HCl if this is the halide used.

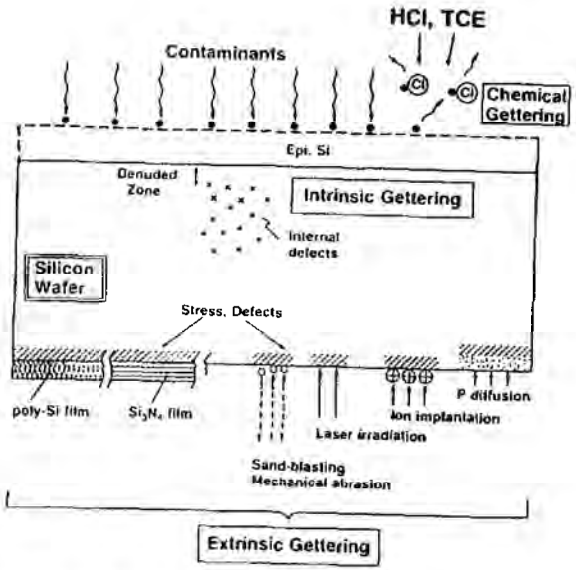


Figure 9.14: Schematic illustration showing various gettering techniques for a silicon wafer (after [9.59]).

The various processes shown in Fig. 9.14 have been reported to form the basis of effective gettering sequences. In practice, the performance of many of these techniques can be disappointing. There are several reasons for this. One reason is that not all defects are amenable to gettering. The defect has to be transportable through the wafer at the temperatures involved [9.59] and, once at the gettering site, should be held there rather than being released into the wafer during subsequent high temperature treatments. Another reason is that additional defects

may be introduced into the wafer during subsequent processing steps. The effectiveness of any given gettering step depends upon the particular starting material and upon the entire processing schedule to which the material is exposed.

Phosphorus diffusion is a well-established gettering step. Several suggestions have been made as to how this gettering action occurs. One is that the gettering involves dislocations which form in the phosphorus-doped layer when heavily-diffused [9.50]. These dislocations then act as sinks for gettered defects. Another suggestion is that phosphorus gettering occurs due to the enhanced solubility of the gettered species in the phosphorus-doped layer [9.60]. A third suggestion, which has been demonstrated to be likely in the case of the gettering of Ni, is that SiP precipitation is responsible for the gettering [9.61]. Each of the above suggestions is supported by the experimental observation that phosphorus gettering is most effective when the phosphorus is very heavily diffused.

A solar cell processing sequence which allows phosphorus gettering to be used very effectively is a p^+nn^+ cell sequence developed by Sandia [9.62]. The heavily phosphorus-diffused rear surface of these cells would be expected to getter defects to the rear, where they would have little influence upon cell performance. Another example is given in Chapter 13, where a processing sequence is described which uses top-surface phosphorus diffusion, followed by chemical removal of the diffused layer. When this approach is applied to polycrystalline substrates, an additional beneficial effect of phosphorus is its preferential diffusion at crystallographic defects near the cell surface. This would be expected to result in those defects being encased in phosphorus-doped material, thus suppressing their electronic effects by reducing the minority carrier concentrations and supply rates.

Deliberate surface damage, generally to the rear surface of the wafer, is another widely used gettering technique (Fig. 9.14). Such damage in the surface region creates dislocations which can act as sinks for bulk defects during subsequent high temperature treatments. Examples of the techniques which have been demonstrated to introduce suitable surface damage include mechanical abrasion, exposure to high laser power densities, ion implantation, impact sound stressing, and reactive ion etching [9.58, 9.63]. In Chapter 11, a sequence is described which advantageously uses laser grooving of the top surface of the cell not

only to promote a gettering action but also to reduce the metallization coverage of that surface.

A number of differing gettering techniques arise from deposited surface layers. Aluminium is such a layer which is commonly used in cells and is known to be an effective getterer of metallic impurities, even at relatively low temperatures [9.64]. Deposited polysilicon layers are also effective getterers, due to the presence of grain boundaries and a general lattice disorder, which act as effective sinks [9.57]. Other layers, such as silicon nitride and aluminium oxide, have also been reported to have an effective gettering effect, probably due to interfacial stresses at high temperatures. The growth of multilayer Si-(0.1 to 1%)Ge alloy on a Si substrate results in the controlled introduction of misfit dislocations which have been demonstrated to be effective in front-surface gettering [9.58]. Bending the substrate during high temperature treatments has also been shown to be effective in gettering crystallographic defects, due to the internal stresses involved [9.65].

9.7 DEFECT PASSIVATION

As opposed to the above gettering techniques, an alternative approach which has the same result is to introduce into the wafer a mobile species which can neutralize the electronic action of bulk defects. Atomic hydrogen is one species which is known to be effective in this respect, particularly for poor quality polycrystalline material [9.66]. Copper is reported to play a similar role [9.67]. Lithium has been investigated widely for passivation of radiation damage in space cells. A somewhat related idea is the deliberate introduction of extra oxygen into silicon ribbon, grown using the EFG technique (Chapter 13). The oxygen appears to neutralize the high carbon concentrations which result from the use of carbon dies in the ribbon forming process [9.68].

REFERENCES

9.1 Y.C. Cheng, "Electronic States at the Silicon-Silicon Interface", Progress in Surface Science, Vol. 8, pp. 181-218, 1977.

9.2 K.L. Nagi and C.T. White, "A Model of Interface States and Charges at the $SiSiO_2$ Interface: Its Predictions and Comparisons with Experiments", Journal of Applied Physics, Vol. 52, pp. 320-327, 1981.

9.3 M. Schulz, "Interface States at the SiO_2-Si Interface", Surface

Science, Vol. 132, pp. 422-455, 1983.

9.4 P. Balk (ed.), "The Si-SiO_2 System", Materials Science Monographs, No. 32, Elsevier, Amsterdam, 1988.

9.5 V.A. Yakovlev, Q. Liu and E.A. Irene, "Spectroscopic Immersion Ellipsometry Study of the Mechanism of Si/SiO_2 Interface Annealing", J. Vac. Sci. Technol. Vol. 10, p. 427, 1992.

9.6 W. Füssel, R. Könenkamp, M. Schmidt and H. Flietner, "Degradation Effects at Si/SiO_2 Interfaces Compared to Those in a-Si", Conf. Proceedings, 11th E.C. Photovoltaic Solar Energy Conference, October, 1992, p. 746.

9.7 S.M. Sze, "Physics of Semiconductor Devices", 2nd edition, Wiley, New York, 1981, pp. 50-51.

9.8 M. Schmidt and H. Köster, Jr., Proc. 7th Conf. on Insul. Films on Semiconductors 1991, ed. W. Eccleston (Adam Hilger, Bristol 1991), p. 135.

9.9 P. Balk, in Proc. Electrochem. Soc. Fall Meeting, 1965, p. 29.

9.10 M.L. Reed and J.D. Plummer, "Chemistry of Si-SiO_2 Interface Trap Annealing", J. Appl. Phys., Vol. 63, pp. 5776-5793, 1988.

9.11 W.D. Eades and R.M. Swanson, "Calculated of Surface Generation and Recombination Velocities at the Si-SiO_2 Interface", J. of Appl. Phys., Vol. 58, pp. 4267-4276, 1985.

9.12 R.K. Bhan, S.K. Lomash, P.K. Basu and K.C. Cahabra, "Interface Properties of Thermal SiO_2 Using 1,1,1 Trichloroethane (TCA)", J. Electrochem. Soc.: Solid State Science and Technology, pp. 2826-2828, 1987.

9.13 H. Fukuda, M. Yasuda and T. Iwabuchi, "Process Dependence of the SiO_2/Si(100) Interface Trap Density of Ultrathin SiO_2 Films", J. Appl. Phys. Vol. 72, pp. 1906-1911, 1992.

9.14 P.E. Gruenbaum, R.A. Sinton and R.M. Swanson, "Light-Induced Degradation at the Silicon/Silicon Dioxide Interface", Appl. Phys. Letters, Vol. 52, pp. 1407-1409, 1988.

9.15 C.H. Bjorkman, J.T. Fitch and G. Lucovsky, "Correlation Between Electronically-Active Trapping States at the Si/SiO_2 Interface and Intrinsic Growth Stress in MOS Structures Formed by Thermal Oxidation of Crystalline Si", Proc. 20th Conference on the Physics of Semiconductors, Thessoloniki, 1990.

9.16 T. Ohmi, M. Miyashita, M. Itano, T. Imaoka and I. Kawanabe, "Dependence of Thin-Oxide Films Quality on Surface Microroughness", IEEE Trans. on Electron Dev., Vol. 39, No. 3, pp. 537-544, 1992.

9.17 M. Niwa, M. Matsumoto, H. Iwasaki, M. Onada and R. Sinclair, "SiO_2/Si Interfaces Studied by Scanning Tunneling Microscopy and High Resolution Transmission Electron Microscopy", J. Electrochem. Soc., Vol. 139, pp. 901-906, 1992.

9.18 M. Nishida, "Distribution of Surface State Density Related to Diffusion Induced Dislocations near the Junction Formed by Diffusion of Phosphorus in Silicon", Jap. J. Appl. Phys. Vol. 11, pp. 673-677, 1972.

9.19 A. Correia, D. Ballutaud and J.L. Maurice, "Microstructure and Electrical Properties of the Silicon/Silicon Dioxide Interface: Effect of Copper Precipitation", 11th European Photovoltaic Solar Energy Conf., Montreux, October, 1992, p. 487.

9.20 J. Snel, "The Doped Si/SiO2 Interface", Solid State Electronics, Vol. 24, pp. 135-139, 1981.

9.21 R.R. King, R.A. Sinton, R.M. Swanson and T.F. Ciszek, "Low Surface Recombination Velocities on Doped Silicon and their Implications for Point Contact Solar Cells", Conf. Record, 19th IEEE Photovoltaic Specialists Conf., pp. 1168-1173, 1987.

9.22 C.T. Sah, "The Equivalent Circuit Model in Solid State Electronics. Part I - The Single Energy Level Defect Centres; Part II - The Multiple Energy Level Impurity Centers", Proc. Inst. Elec. Electron. Eng., Vol. 55, pp. 654-684, 1967.

9.23 W.M. Chen, B. Monemar and E. Janzen, "Direct Observation of Intercenter Charge Transfer in Dominant Nonradiative Recombination Channels in Silicon", Physics Review Letters, Vol. 67, pp. 1914-1917, 1991.

9.24 N.M. Johnson, W.B. Jackson and M.D. Moyer, "Optical Absorption by Electronic Defects at the Si-SiO_2 Interface", Proc. 13th Int. Conf. on Defects in Semiconductors, 1984, p. 499.

9.25 Martin A. Green, "Solar Cells: Operating Principles, Technology and System Applications", (Prentice-Hall, New Jersey, 1982). (Reprinted 1986, 1992, available from author).

9.26 A.G. Aberle, S. Glunz and W. Warta, "Impact of Illumination Level and Oxide Parameters on Shockley-Read-Hall-Recombination at the Si-SiO_2 Interface, J. Appl. Phys., Vol. 71, pp. 4422-4431, 1992.

9.27 W.D. Eades and R.M. Swanson, J. Appl. Phys., Vol. 58, p. 4267, 1985.

9.28 H. Deuling, E. Klausmann and A. Goetzberger, Solid State Electronics, Vol. 58, p. 559 (1972).

9.29 N.M. Johnson, Appl. Phys. Lett. Vol. 34, p. 802, 1979.

9.30 T. Katsube and K. Kakimoto, J. Appl. Phys. Vol. 52, p. 3504,

1981.
9.31 D.. Vuillaume, D. Goguenheim and G. Vincent, Appl. Phys. Lett., Vol. 57, p. 1206, 1990.
9.32 K. Yamasaki, M. Yoshida and T. Sugano, Jap. J. Appl. Phys. Vol. 18, p. 113, 1979.
9.33 T.J. Tredwell and C.R. Viswanathan, Appl. Phys. Lett., Vol. 36, p. 462, 1980.
9.34 E. Klausmann, Proc. Conf. on Insulating Films on Semiconductors (INFOS), Erlangen (Springer, Berlin, 1981), p. 169.
9.35 A.W. Stephens, A. Aberle and M.A. Green, "Surface Recombination Velocity Measurements at the Silicon-Silicon Dioxide Interface by Microwave-Detected Photoconductance Decay", J. Appl. Phys., Vol. 76, pp. 363-370, 1994.
9.36 E. Yablonovitch, R.M. Swanson, W.D. Eades and B.R. Weinberger, "Electron-Hole Recombination at the Si-SiO_2 Interface", Applied Physics Letters, Vol. 48, pp. 245-247, 1986.
9.37 C.A. Mead, "Metal-Semiconductor Surface Barriers", Solid State Electronics, Vol. 9, p. 1023-1032, 1966.
9.38 V. Heine, "Theory of Surface States", Physical Review A, Vol. 138, pp. 1689-1696, 1965.
9.39 B.L. Sharma (ed.)., "Metal-Semiconductor Schottky Barrier Junctions and their Applications", Plenum, New York, 1984.
9.40 D.E. Kane and R.M. Swanson, "Measurement of the Emitter Saturation Current by a Contactless Photoconductivity Decay Method", Conf. Record, 18th IEEE Photovoltaic Specialists Conference, Las Vegas, October, 1985, pp. 578-583.
9.41 M.A. Green and R.B. Godfrey, "MIS Solar Cell-General Theory and New Experimental Results for Silicon", Applied Physics Letters, Vol. 29, pp. 610-611, 1976.
9.42 M.A. Green, A.W. Blakers, M.R. Willison, T. Szpitalak, E.M. Keller, E. Gauja and P.J. Hart, "The MINP Solar Cell - A New High Voltage, High Efficiency Silicon Solar Cell", 15th IEEE Photovoltaic Specialists Conf., Orlando, May, 1981, p. 1405.
9.43 M.A. Green and A.W. Blakers, "Advantages of MIS Structures for Silicon Solar Cells", Solar Cells, Vol. 8, pp. 3-16, 1983.
9.44 N.G. Tarr, "A Polysilicon Emitter Solar Cell", IEEE Electron Device Letters, Vol. EDL-6, pp. 655-658, 1985.
9.45 F.A. Lindholm, A. Neugroshel, M. Arienzo and P.A. Iles, "Heavily Doped Polysilicon Contact Solar Cells", IEEE Electron Device Letters, Vol. EDL-6, pp. 363-365, 1985.
9.46 E. Yablonovitch, T. Gmitter, R.M. Swanson and Y.K. Kward, "A 720 mV Open-circuit voltage SiO_x:c-Si:SiO_x Double Heterostructure Solar Cell", App. Phys. Lett., Vol. 47, p. 1211, 1985.
9.47 P. Van Halen and D.L. Pulfrey, "High Gain Bipolar Transistors with Polysilicon Tunnel Junction Emitter Contacts", IEEE Transactions on Electron Devices, Vol. ED-32, p. 1307, 1985.
9.48 T. Sawada, N. Terada, S. Tsuge, T. Baba, T. Takahama, K. Wakisaka, S. Tsuda and S. Nakano, "High-Efficiency a/Si/c-Si Heterojunction Solar Cell", Conf. Record, 1st World Conf. on Photovoltaic Energy Conversion, Hawaii, 1994.
9.49 F. Shimura, Semiconductor Silicon Crystal Technology, (Academic Press, New York), 1989.
9.50 K.V. Ravi, "Imperfections and Impurities in Semiconductor Silicon", Wiley, New York, 1981.
9.51 P.F. Schmidt and C.W. Pearce, "A Neutron Activation Analysis Study of the Source of Transition Group Metal Contamination in the Silicon Device Manufacturing Process", Journal of the Electrochemical Society, Vol. 128, pp. 630-637, 1981.
9.52 K. Graff, H. Pieper and R. Goldback, in "Semiconductor Silicon 1973", H.R. Huff & R.R. Burgess (eds), Electrochemical Society, New Jersey, 1973, p. 170; K. Graff and H. Fischer, "Carrier Lifetime in Silicon and its Impact on Solar Cell Characteristics", in Topics in Applied Physics, Vol. 31, P.O. Seraplin (ed.), Springer-Verlag, Berlin, 1979, pp. 173-211.
9.53 H.R. Huff, "Chemical Impurities and Structural Imperfections in Semiconductor Silicon: Parts I and II", Solid State Technology, pp. 89-95, February, 1983 and pp. 211-222, April, 1983.
9.54 P.F. Schmidt, "Contamination-Free High Temperature Treatment of Silicon or Other Material", Journal of the Electrochemical Society, Vol. 130, pp. 196-199, 1983.
9.55 C.W. Pearce, L.E. Katz and T.E. Seidel, "Considerations Regarding Gettering in Integrated Circuits", in "Semiconductor Silicon 1981", H.R. Huff, R.J. Kriegler and Y. Takeishi (eds), Electrochemical Society, New Jersey, 1981, pp. 705-723.
9.56 P.F. Schmidt, "Furnace Contamination and its Remedies", Solid State Technology, pp. 147-151, June, 1983.
9.57 J.R. Davis, A. Rohatgi, R.H. Hopkins, P.D. Blais, P. Rai-Choudhury, J.R. McCormick and H.C. Mollenkopf, "Impurities in Silicon Solar Cells", IEEE Transactions on Electron Devices, Vol. ED-27, pp. 677-687, 1980.
9.58 D.K. Sardana, "Gettering in Processed Silicon", Semiconductor International, pp. 362-368, May, 1985.

9.59 F. Shimura, Semiconductor Silicon Crystal Technology, (Academic Press, New York), 1989.

9.60 L.E. Katz, P.F. Schmidt and C.W. Pearce, "Neutron Activation Study of a Gettering Treatment for Czochralski Silicon Substrates", J. Electrochem. Soc., Vol. 128, pp. 620-624, 1981.

9.61 A. Ourmazd and W. Schroter, "Phosphorus Gettering and Intrinsic Gettering of Nickel in Silicon", Applied Physics Letters, Vol. 45, pp. 781-783, 1984.

9.62 J.G. Fossum and E.L. Burgess, "High Efficiency p^+-n-n^+ Back-Surface-Field Silicon Solar Cells", Applied Physics Letters, Vol. 33, pp. 238-240, 1978.

9.63 R.B. Swaroop, "Advances in Silicon Technology for the Semiconductor Industry", Solid State Technology, pp. 97-101, July, 1983.

9.64 R.D. Thompson and K.N. Tu, "Low Temperature Gettering of Cu, Ag and Au Across a Wafer of Si by Al", Applied Physics Letters, Vol. 41, pp. 440-442, 1982.

9.65 R. Sawada, T. Karaki and J. Watanabe, "Gettering of Crystalline Defects in Si by Bending", Appl. Phys. Lett., Vol. 38, pp. 368-369, 1981.

9.66 B.L. Soporoi, X. Dang, J.P. Benner, A. Rohatgi, P. Sana, S.K. Estreicher, Y.K. Park and M.A. Roberson, "Hydrogen in Silicon: Current Understanding of Diffusion and Passivation Mechanisms", Conf. Record, 1st World Conf. on Photovoltaic Energy Conversion, Hawaii, 1994.

9.67 T. Daud and K.M. Koliwad, "Effect of Cooper Impurity on Polycrystalline Silicon Solar Cells", Conf. Record, 13th IEEE Photovoltaic Specialists Conf., Washington, 1978, pp. 503-506.

9.68 K.V. Ravi, "Silicon Ribbons for Low-Cost Photovoltaics - Current Status and Future Potential", 1st International Photovoltaic Science and Engineering Conf. Kobe, Nov., 1984, pp. 43-50.

Chapter
10

EVOLUTION OF SILICON SOLAR CELLS

10.1 INTRODUCTION

Although the history of silicon solar cells dates back over fifty years to the very beginning of the silicon bipolar device era, the last decade has seen enormous improvements in both the performance of experimental cells and cell theory. Over the last few years, cells have reached performance levels once thought not to be physically attainable. As shown in Fig. 1.1 (page 1), present laboratory cells convert over 24% of incident energy in sunlight into electricity, well above the value of 20% once thought to be a basic limit.

Silicon solar cells have different design and material requirements from most other silicon electronic devices. Not only is nearly ideal passivation of silicon surfaces required, but the bulk properties must also be of uniformly high quality for high energy conversion efficiency. This is because some wavelengths of light have to pass several hundred microns through the silicon before absorption, producing carriers that must still be collected by the cell.

This Chapter reviews the history of silicon solar cell development, discusses the features of modern cell design and outlines possible performance improvements which might be expected in the future.

10.2 EARLY SILICON CELLS

The first silicon cells resulted from interest in silicon for use in point contact rectifiers. The rectifying properties of sharp metal contacts to various crystals had been known since at least 1874 [10.1]. In the early days of radio, such crystal rectifiers were almost universally used as detectors in radio receivers [10.2]. However, with the development of thermionic tubes, these crystal rectifiers were displaced except for ultra-high frequency work. The most suitable for this work proved to be tungsten points to silicon surfaces. This provided the incentive for improving the purity of silicon and further understanding its properties.

In studies of recrystallized melts of pure silicon prepared for this purpose, Russell Ohl of Bell Laboratories discovered well defined barriers in polycrystalline ingots grown from some lots of commercial high purity silicon [10.3]. These "grown-in" junctions resulted from impurity segregation during the recrystallization process. Ohl found that one side of the junction reached a negative potential when samples were illuminated or heated. The same side had to be biased negatively to show low resistance to current flow across the barrier or across a point contact to this material. This led to the terminology of "negative-" or "n-type" silicon for the material on this side of the junction. The material of opposite type was named "positive-" or "p-type". It was apparently only after this initial experimental work that the role of donor and acceptor impurities in producing these properties was shown.

In 1941, the first photovoltaic devices based on these "grown-in" junctions were described [10.3]. Figure 10.1(a) shows the geometry of cells cut from the recrystallized material, in this case so that the junction was parallel to the illuminated surface. Contact was made at the periphery of the top of the device as shown, and over the entire rear surface. No energy conversion efficiency figures were reported for these cells, although an analysis of the data suggests efficiency well below 1%. The cells were obviously quite difficult to fabricate due to the lack of control over the junction location.

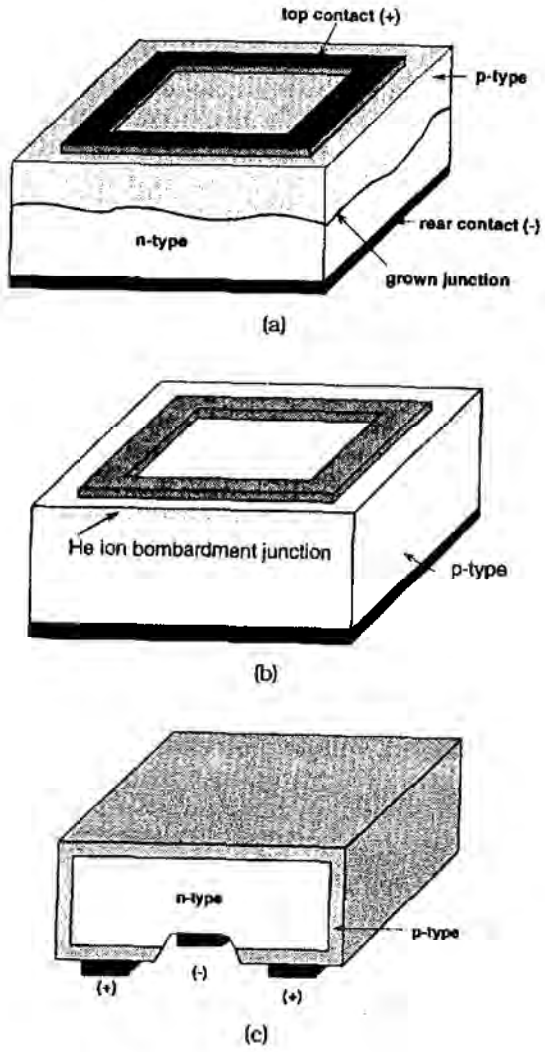


Figure 10.1(a): Silicon solar cell reported in 1941 relying on "grown-in" junctions formed by impurity segregation in recrystallized silicon melts; (b) helium-ion bombarded junction device of 1952; (c) first modern silicon cell, reported in 1954, fabricated on single-crystalline silicon wafers with the p-n junction formed by dopant diffusion.

A more controllable method of junction formation was reported by Kingsbury and Ohl in 1952 [10.4]. These cells used recrystallized silicon fabricated from pure source material to prevent "grown-in" junctions being formed. Helium ion bombardment of the surface was used to form the rectifying junction as shown in Fig. 10.1(b). A similar contacting scheme was used as for the earlier devices. These devices showed quite respectable spectral responsivity, although energy conversion efficiencies were again not reported. They are estimated to lie somewhere around 1%.

These early efforts were quickly overtaken by the rapid development of silicon technology, also at Bell Laboratories. Improved techniques for crystal growth producing single crystal wafers of silicon were developed, as were techniques for doping using high temperature diffusion of impurities. This led to the first report of a modern silicon cell in 1954 by Pearson, Fuller and Chapin of Bell Laboratories [10.5]. The first cells used lithium diffusion to form the junction and had an efficiency of about 4.5% [10.6]. The lithium diffusion was soon replaced by boron diffusion with the efficiency increasing to 6% [10.5,10.6].

These cells had the dual rear contact structure of Figure 10.1(c) and opened up the first real prospects for power generation using photovoltaics [10.7]. Improvement in the cell structure led to demonstration of 10% efficiency within 18 months of the initial report [10.7].

The wrap-around structure of Fig. 10.1(c) has the advantages of a zero obscuration of the top surface by contacts and the ease of interconnection which arises from having both contacts on one surface. However, it suffered from a high resistance due to the fact that these early cells were fabricated on complete wafers, with correspondingly large current paths required around the diffused skin. The idea re-surfaced in a commercial product, manufactured by the Sharp Corporation in the early 1970's, which used half of a small-diameter wafer (2-3 cm) for each cell [10.8]. More recently, schemes have been suggested which allow this approach to be extended to larger area wafers, as in the "polka-dot" solar cell where a large array of holes etched through the wafer provides shorter current paths to the rear [10.9]. Apart from the advantages already described, such an

approach could boost the performance of relatively low quality material. If diffusion lengths can be increased to about half the wafer thickness, in material such as ribbon and polycrystalline silicon, this approach could be used to make almost the entire substrate volume photovoltaically active (Chapter 12).

The next performance increase arose as a result of placing one contact on the top surface and finally extending this concept to contact fingers. By 1960, terrestrial energy conversion efficiencies as high as 14% had been reported [10.10] due to this improvement. An efficiency reported as 15% was measured for an n-type cell in terrestrial sunlight at 18°C [10.11]. At about the same time, there was a shift in emphasis from n-type to p-type substrates due to the increasing interest in using the cells in spacecraft, and to the better radiation resistance of the latter substrates. By the early 1960's [10.12], cell design had reached a stage which was to remain relatively stable for a decade.

10.3 CONVENTIONAL SPACE CELLS

The cell design which evolved [10.11,10.12] for space use is shown in Fig. 10.2(a). Key features include the use of 10 Ω cm p-type substrates to maximize radiation resistance, and the use of a nominally 40 Ω/square, 0.5 μm deep phosphorus diffusion. Although it was known that lighter diffusions gave better blue response, this value was chosen because it was found to be more resistant to shunting by the top contact metallization during processing [10.12]. The benefit of an intervening layer of Pd for improving the moisture resistance in the pre-flight environment was demonstrated later in the decade [10.13]. For the 2 cm x 2 cm cells which became standard for space use, a 1 mm wide busbar was normally located along one edge of the cell. Perpendicular to this ran the top contact fingers, which were usually six in number. These were defined by evaporation through a metal shadow mask. A silicon monoxide (SiO) antireflection (AR) coating was used to minimize reflection from the top surface of the cell. Such coatings become quite absorbing at wavelengths below 0.5 μm [10.14].

These cells remained the standard for space use for more than a decade and are even now still specified for some space missions. Energy conversion efficiency was 10-11% under space radiation, and 10-20% higher on a relative basis under terrestrial test conditions.

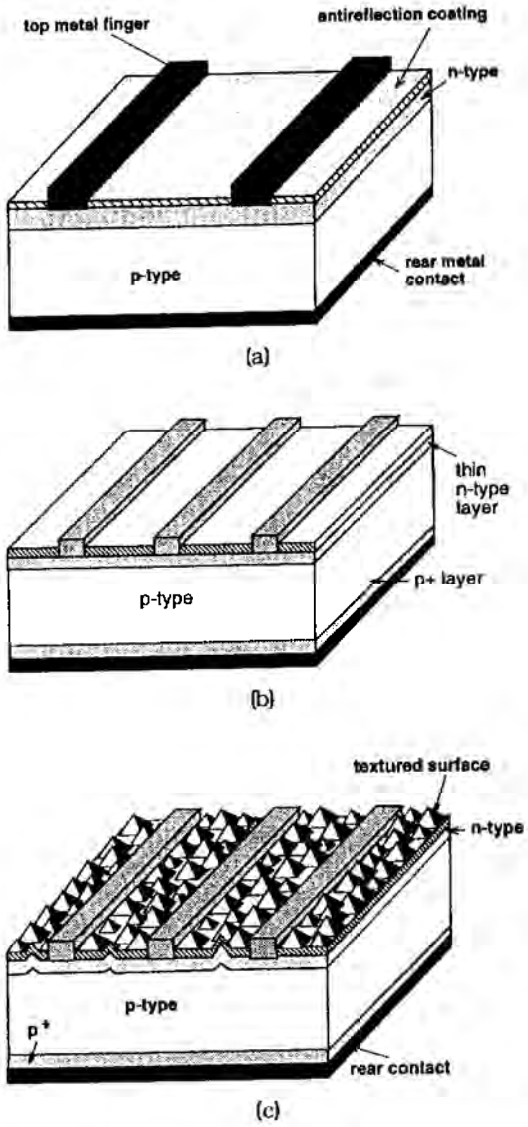


Figure 10.2: (a) Space silicon cell design developed in the early 1960's which became a standard design for over a decade; (b) shallow junction "violet" cell; (c) chemically textured non-reflecting "black" cell.

Towards the end of the decade, the benefits of a rear Al treatment were becoming apparent, particularly for cells which were thinner than normal [10.15,10.16]. The corresponding increase in space cell efficiency to 12.4% was attributed to the gettering action of the Al treatment [10.13].

10.4 BACK SURFACE FIELDS

In what appears to be the first application of Shockley's diffusion theory to photovoltaic energy conversion, Cummerow [10.17] discussed minority carrier reflecting boundary conditions and highlighted the importance of thin cells. Wolf [10.18] subsequently discussed the effect of bulk fields, such as produced by doping gradients, upon the current collecting capabilities of the cell. As mentioned in the previous section, the experimental benefits of rear surface Al treatments were known by the early 1970's [10.15,10.16]. These benefits were improved open-circuit voltage, short-circuit current density, and efficiency, attributed to the gettering action of the Al [10.13].

More detailed work showed that it was the presence of a heavily doped region beneath the rear contact which gave rise to these beneficial effects [10.19]. These benefits were postulated to arise from spillage of majority carriers from the rear doped region into the bulk region of the cell, thus increasing the effective bulk concentration and hence the open-circuit voltage [10.19]. Although the correct explanation, in terms of a reduction in the effective rear surface recombination velocity, was soon forthcoming [10.20], the effect is still rather inappropriately, but almost universally, referred to as the back surface field (BSF) effect [10.19].

This effect resulted in 5-10% improvement in the efficiency of cells fabricated on 10 Ω cm p-type substrates [10.13], taking them to the performance levels which had been demonstrated earlier for n-type substrates [10.11].

10.5 VIOLET CELLS

As noted earlier, conventional space cells had a relatively poor response to wavelengths which were shorter than 0.5 μm, due to the relatively heavy top junction diffusion and the use of an SiO AR coating

which absorbs light below this wavelength. A marked improvement in performance was demonstrated in the early 1970's by replacing such junctions with much shallower (0.25 μm), higher sheet resistivity junctions, and re-designing the entire cell to accommodate this change, as shown in Fig. 10.2(b).

Figure 10.3 shows the profile of electrically active phosphorus in silicon as a function of the diffusion conditions [10.21]. The flat part of the curve near to the surface corresponds to regions where phosphorus is present in concentrations higher than its solid solubility at the diffusion temperature. As noted in Chapter 9, precipitates of SiP have been observed at the surface under such conditions as have misfit dislocations. The electrical quality of such regions is very poor, so much so that the flat regions of Fig. 10.3 can be regarded as "dead layers" for the purposes of photovoltaic activity. In the violet cell, the aim was to have shallow diffusion, even shallower than the shallowest in Fig. 10.3, so that the "deal layer" was eliminated [10.22].

To accommodate the increased sheet resistivity of the diffused layer, much finer metal finger patterns were also incorporated using photolithography to define their geometry. As a consequence, the cell resistance was actually lower than in conventional cells. Improved antireflection coatings, based upon TiO_2 and later Ta_2O_5, were also incorporated. These were less absorbing than SiO, as well as providing a better optical match between the cells and the cover glass to which space cells are normally bonded. The thickness of these coatings was also selected so they would be effective at shorter wavelengths than were traditional coatings, thus giving the cells their characteristic violet appearance. (A subsequent development, made possible by the higher refractive index of the new AR coating materials, was the use of double layer AR coatings).

The final design change in the cells was the use of lower resistivity 2 Ω cm substrates. Since the improved output of the cells at blue wavelengths was quite tolerant to radiation exposure, the overall radiation tolerance remained at least equal to that of the conventional devices, while giving an improved voltage output. The combination of improved open-circuit voltage (due to the change in substrate resistivity), improved current output (due to the removal of "dead layers", better antireflection coatings, and lower top contact coverage), and improved fill factor (due to the improved open-circuit voltage and

decreased cell resistance) resulted in a massive increase of 30% in performance as compared to an average space cell of conventional design. Efficiencies of 13.5% were obtained under space radiation. The improvement over earlier cells fabricated on n-type substrates was not quite as dramatic, with terrestrial efficiencies close to 16% being demonstrated [10.22] as compared to the 14-15% values for n-type substrates [10.11].

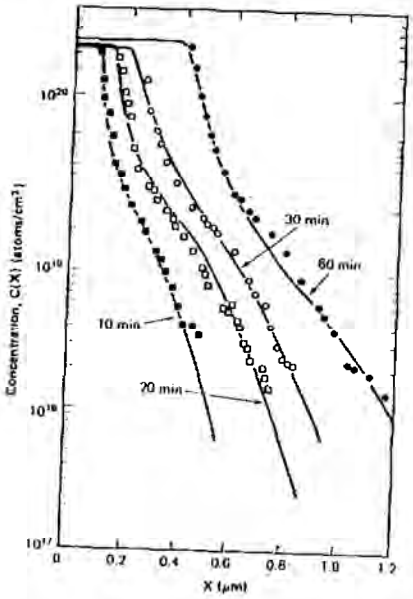


Figure 10.3: Profiles of electrically active phosphorus in silicon as a function of diffusion time at 1000°C (after Tsai [10.21], © 1969 IEEE).

10.6 BLACK CELLS

Not long after the superior performance of the violet cell had been established, a further boost in performance was obtained by texturing the top surface of the cell [10.23]. The idea of mechanically forming pyramids on the top surface of the cell to reduce reflection had been suggested some time earlier [10.24]. In the black cell, a simpler approach was used which relied upon the random nucleation of

selective etches to expose (111) crystallographic planes in a substrate originally of (100) surface orientation. The intersecting (111) planes so exposed formed square-based pyramids of random size which were distributed randomly over the cell surface, as indicated in Fig. 10.4(a).

This has two advantages for cell performance. One is that light striking the sides of the pyramids is reflected downwards and hence has at least one more chance of being coupled into the cell, as indicated in Fig. 10.4(b). A second advantage is that light coupled into the cell enters obliquely as also indicated by this figure. Most light will be coupled in at the first point of incidence on the pyramids. This light is refracted in at an angle of about 48° to the original surface, resulting in an increase in the pathlength of weakly absorbed light by a factor of 1.35 compared to a non-textured cell. The effect is similar to that of an increase in the silicon absorption coefficient or in the bulk diffusion length by the same factor. A third feature of the texturing approach is the high degree of light trapping possible, as discussed in Chapter 6. For terrestrial cells, this is an advantage since it improves the long wavelength response of cells. However, for space cells, it is a disadvantage since it increases the absorption of sub-bandgap photons in the rear contact of the cell. Due to the decreased number of options available for dissipating the heat so generated, this causes the cells to operate at a higher temperature in the space environment, largely negating the previous advantages. Combined with a greater potential for mechanical damage during array assembly by knocking peaks from pyramids, this has meant that textured cells have not been as widely used in space as their apparent performance advantage initially seemed to warrant.

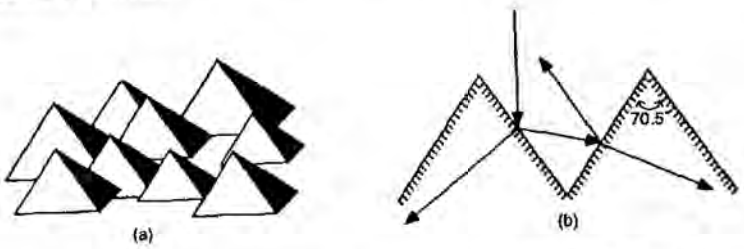
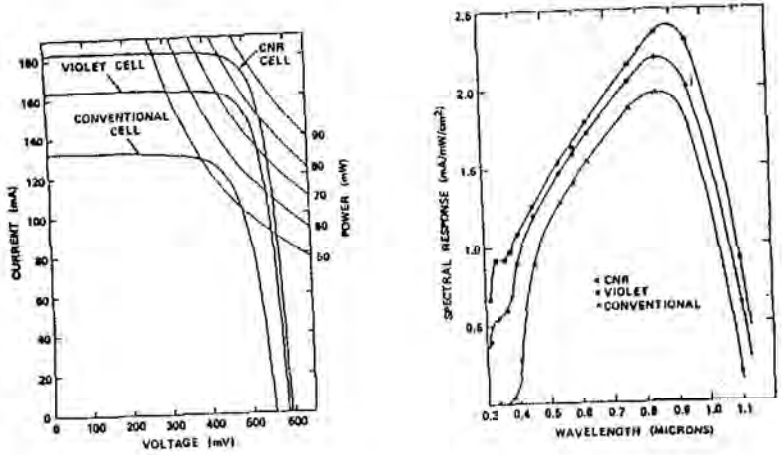


Figure 10.4: (a) Schematic diagram showing the square-based pyramids formed by exposed (111) crystallographic planes when (100)-oriented silicon wafers are anisotropically etched; (b) ray diagram showing paths of reflected and transmitted light.

Hydrazine hydrate was used initially as the selective etch for texturing. This was followed by the development of sequences which were based upon more benign potassium hydroxide or sodium hydroxide solutions. The selectivity of these etches is a sensitive function of solution concentration and temperature [10.25]. A commonly used texturing etch is a weak NaOH solution (2% weight/volume) mixed with isopropanol and heated to 90°C.

Figures 10.5(a) and (b) quantify the performance advantage of violet and black cells over conventional space cells. The improved open-circuit voltage arises from the use of lower resistivity substrates (2 Ω cm) than the 10 Ω cm substrate resistivities previously used. A similar improvement could also have been obtained by using higher resistivity substrates and a back surface field. For both advanced cells the major area of improvement lay in the short-circuit current density. This arises from the removal of the "dead layer" in the conventional cells, from the reduced reflection losses, and from the oblique coupling of the light for the black cells. Figure 10.5(b) shows the effect of these improvements upon the cell spectral response. At a wavelength of 0.6 μm, the black and violet cells have similar responses. Their superiority over a conventional cell arises from the absence of the inactive surface layer. This superiority becomes even more pronounced at shorter wavelengths. The advantage of the black cell over the violet cell at such wavelengths arises from reduced reflection losses. At long wavelengths, this advantage is augmented by the oblique coupling provided by the textured surfaces.

The parameters of the black cell shown in Figure 10.5(a) correspond to an energy conversion efficiency of 15.5% under AM0 radiation. Terrestrial efficiencies were appreciably higher [10.23,10.26]. Under the current terrestrial standard (Global AM1.5, 100 mW/cm^2, 25°C), an energy conversion efficiency of 17.2% is estimated. Such were the strengths of the texturing concept, when combined with the technological improvements incorporated into the violet cell, that it was almost a decade before any significant improvement in cell performance was demonstrated. These improvements ultimately came about as a result of an increased open-circuit voltage due to the development of improved surface and contact passivation approaches.



(a) (b)

Figure 10.5: (a) Output current-voltage characteristics of a black (Comsat Non-Reflecting/CNR), a violet and a conventional solar cell under AM0 radiation; (b) spectral response of a black (CNR), a violet and a conventional cell, all of 2 cm x 2 cm dimensions (after Haynos et al [10.23]).

10.7 OXIDE SURFACE PASSIVATION

The simplicity of the surface passivation afforded by its thermal oxide is one of the key features of silicon technology which explains its present dominance in microelectronics. Unfortunately for photovoltaics, the refractive index of silicon dioxide is too low for its use as an effective antireflection coating in high performance cells. In fact, if present in any reasonable thickness (greater than 20 nm) on the top surface of the cell, it will limit the ability to reduce reflection by the subsequent deposition of any number of compensating layers [10.,27]. Hence, if oxide passivation is to be used on exposed cell surfaces, the oxide layer has to be very thin. Around 1978, two results convincingly demonstrated the benefits of the passivation of surfaces by thin oxides. One set of results arose from work on the application of metal-insulator-semiconductor (MIS) tunnel diodes to energy conversion

[10.28]. In this approach, a thin oxide was grown over the top surface of an undoped substrate, the top metal contact was deposited in a grid pattern on top of this oxide, and an antireflection coating with a high fixed charge density was deposited over both [10.28]. The oxide in this case had to be very thin (less than 2 nm) to allow tunnelling between the contact and the substrate. By using high-quality, low resistivity substrates to reduce bulk recombination, it was shown that the open circuit voltage of cells fabricated in this way was limited by recombination at the interface of the thin oxide with the silicon [10.28]. The remarkable feature of these devices was their high open-circuit voltages, with values above 650 mV being demonstrated for the first time in silicon. The cells also had a creditable blue response also due to the surface passivation provided by the thin oxide. Similar cells have since been commercialized [10.29].

The benefits were also convincingly demonstrated for more conventional cells developed by Sandia Laboratories [10.30]. These had a p^+-n-n^+ structure, and used 300 μm thick, 10 Ω cm n-type substrates. The rear n^+ region was formed by heavy phosphorus diffusion. The gettering provided by this region helped to give post-processing carrier lifetimes of the order of a millisecond [10.30]. A shallow (about 0.25 μm) boron diffusion of approximately 200 Ω/square sheet resistivity was used for the top layer, with plasma-deposited silicon nitride used as the antireflection coating. Without a passivating oxide layer, such cells displayed creditable terrestrial efficiencies of between 15-16%. With a passivating layer of 5 nm of oxide grown at 800°C in dry oxygen, there was a marked increased in both the short-circuit current density and the open-circuit voltages of the cells, with efficiencies of up to 16.8% demonstrated [10.30]. Although lower than demonstrated by black cells, this was an exceptionally high performance level, considering that the cells had a non-optimized contact covering about 10% of the top surface of the cell and that only a single layer AR coating was used for reflection control.

All subsequent high efficiency silicon cells have taken advantage of the passivation provided by thin thermal oxide layers to maximize their open-circuit voltage and short-wavelength response.

10.8 CONTACT PASSIVATION

Contacts made to the surface are generally regions of high recombination velocity. Best cell performance will be obtained when

the electronic activity at such contacts is "passified". Three techniques have been demonstrated, as discussed in Chapter 9.

The earliest approach was to passivate by isolating the contact from minority carriers by interposing a heavily doped region. It was shown in Section 10.4 how rear-contact passivation via the "back surface field" effect resulted in significant gains in cell performance. Heavily doped regions, localized to those areas where the top contact is made to the cell, are used in most recent high efficiency cell designs.

A second approach to reducing contact effects is to minimize the contact area [10.31,10.32]. The benefits were demonstrated by increased open-circuit voltages on low resistivity substrates [10.33]. Most recent high-efficiency cells employ this low contact area approach. A third approach is to employ a contacting scheme in which the contact itself has an inherently low recombination velocity. The MINP (metal-insulator-NP junction) cell of Fig. 10.6 was the first successfully to exploit this approach [10.34]. The thin surface passifying oxide is continued under the metal, thus reducing its effective recombination velocity. Polysilicon [10.35] and semi-insulating polysilicon (SIPOS) [10.36] contact passivation have also been demonstrated. It appears that a thin interfacial oxide layer may play an important role in both of these schemes [10.36,10.37].

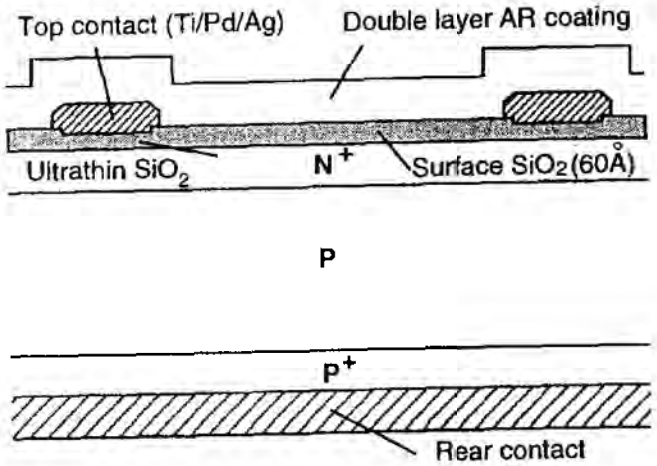


Figure 10.6: Metal-Insulator-NP junction (MINP) solar cell.

10.9 TOP SURFACE PASSIVATED CELLS

As seen in Fig. 1.1, the performance levels established by "violet" and "black" cells in the mid-1970's remained unchallenged for close to a decade. Cells successfully incorporating the oxide and contact passivation approaches of the previous section, along the top surface, were the first to exceed these levels.

The MINP cell, the first silicon cell to demonstrate 18% efficiency, arose from earlier work with the MIS cell [10.28], briefly mentioned in Section 10.7. The MINP cell structure (Fig. 10.6) employs top contact passivation by the use of a thin oxide layer underlying this contact, as well as top surface passivation by a slightly thicker oxide layer. This difference in thickness complicates processing but was found necessary to achieve maximum device performance. The top contact metallization is a Ti/Pd/Ag multilayer. The use of a low work function metal such as Ti as the contact layer is essential with this approach. This is to produce an electrostatically induced accumulation layer in the underlying silicon, an important factor in reducing contact recombination. The cells used alloyed aluminium to give a heavily doped region near the rear contact and were fabricated on polished (100)-oriented 0.2 Ω cm substrates. Surface passivation is easier to achieve on polished rather than textured or "as-lapped" surfaces. To minimize reflection losses, a double layer antireflection coating was used which consisted of approximately a quarter-wavelength of ZnS on top of the thin oxide, followed by a quarter-wavelength of MgF_2.

The PESC (Passivated Emitter Solar Cell) structure, shown in Fig. 10.7, further improved cell efficiency. It is similar to the MINP cell structure, except that electrical contact is made directly through narrow slots in the thin oxide. In this case, contact passivation is obtained by minimizing the contact area.

Processing in both cases involved the shallow diffusion of the top phosphorus layer, the growth of the passivating oxide, and the etching of the contact regions. For the MINP cells, the thin tunnel oxide is subsequently grown in these contact regions, prior to the deposition of the top contact. Aligned photolithography is used in this case to align the top contact with the contact areas. The PESC cells can take advantage of a simpler sequence, in which the photoresist used to define the contact areas also defines the top contact metal. This metal

is subsequently silver plated in both cases to increase its current handling capability. The processing includes a rear Al alloying step which gives a low rear contact resistance, gives rise to light trapping in the cell by randomizing the direction of reflected light [10.38] and getters impurities from the bulk.

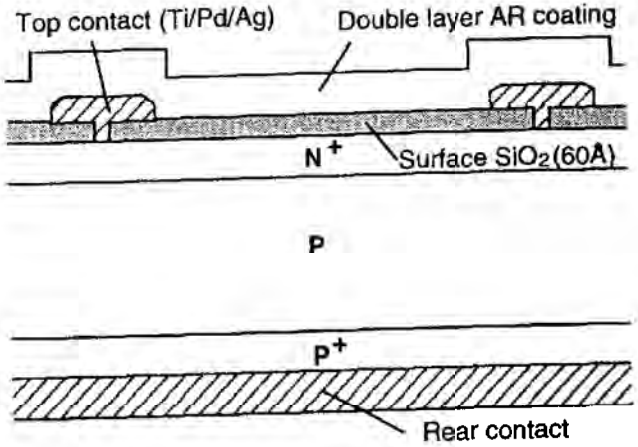


Figure 10.7: Schematic diagram of the Passivated Emitter Solar Cell (PESC cell).

For both MINP and PESC cells, a simple top contact design was adopted which consisted of parallel fingers spaced 0.8 mm apart. The cross-sectional areas of the fingers in both cases were about 150 square microns, with the PESC cell having a slightly narrower finger width of 20 μm compared to 30 μm for the MINP cell. A more detailed characterization of these devices is given elsewhere [10.38]. Key features include the demonstration of substantial light trapping in these cells for the first time for silicon and identification of the role of edge junction isolation in producing non-ideal dark current components.

By combining the benefits of surface texture with the strengths of the PESC approach, the first non-concentrating silicon cells with an efficiency greater than 20% were fabricated in 1985 [10.40]. The structure of the "microgrooved" PESC cells used to achieve this performance milestone is shown in Fig. 10.8.

Rather than using pyramidal texturing, the cells used microgrooving to

achieve the same effect. The microgrooves were defined by using selective etches to expose crystal planes. Photolithographically designed oxide patterns were used to protect the surface against etching where this was not required, and so determine the final pattern of microgrooves. This approach was found to be easier to combine with fine line photolithography than was the normal pyramidal texturing. It had the additional benefit of reduced series resistance losses associated with the top layer, since the cross sectional area for a given diffusion depth is increased by a factor of $\sqrt{3}$.

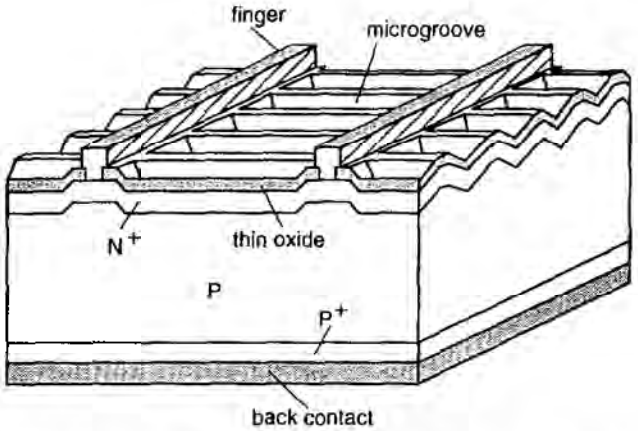


Figure 10.8: The microgrooved PESC cell, the first silicon cell to exceed 20% efficiency in 1985.

The main advantage over the normal PESC cell lies in the current output, with an approximately 5% improvement over similarly processed cells with polished surface being demonstrated. Incremental improvement in the surface passivation also allowed surface recombination to be reduced, despite the larger surface area and the less favourable orientation of the exposed (111) surfaces. The improved voltage and reduced resistance losses also allowed the fill factor to be increased, resulting in close to 10% relative improvement in performance relative to the standard PESC cells.

The key characteristics of the PESC sequence are oxide surface passivation, self-aligned contacts through this oxide, high sheet resistivity top junction diffusion, alloyed aluminium rear surface passivation and antireflection control by texturing or double layer

antireflection coating.

The PESC sequence has proved to be very rugged and repeatable. Within one year of the initial 20% results, two groups had reported results approaching this figure (when referred to present calibrations) using almost identical structures [10.41, 10.42]. The sequence has since been reproduced in many laboratories, with commercial product now available for space and concentrator cells [10.43] or for high value-added applications such as solar car racing [10.44].

10.10 TOP AND REAR PASSIVATED CELLS

The next major advance in cell performance came as a result of applying surface and contact passivation approaches to both top and rear surfaces.

The rear point contract solar cell of Fig. 10.9 achieved this landmark in cell design. Since both contacts are on the rear of the cell, the design places enormous pressure both upon the quality of surface passivation along both top and rear surfaces and upon post-processing carrier lifetimes. To achieve design objectives in these areas, full advantage had to be taken of developments in microelectronics.

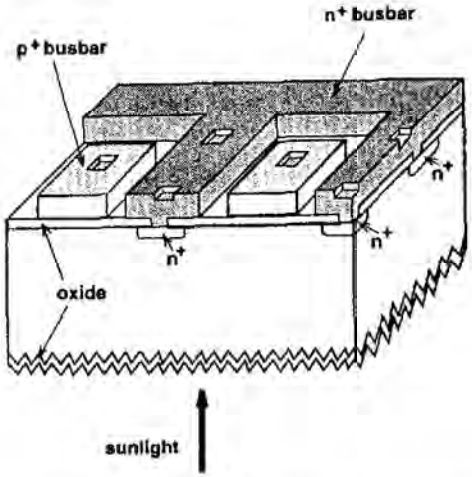


Figure 10.9: Rear point contact solar cell which demonstrated 22% efficiency in 1988 (cell rear shown uppermost).

Although originally developed for concentrator cells [10.45], the device design was modified for one-sun use by adding a phosphorus diffusion along the illuminated surface [10.46]. This produced the first silicon cells of efficiency above 22%. These cells will be discussed further in Chapter 12 dealing with concentrator cells, since this is the application where they have their greatest strengths.

Combining the earlier PESC sequence with similar double-sided surface passivation and chlorine based processing [10.47] produced an improved device, the PERL cell (Passivated Emitter, Rear Locally-diffused cell) shown in Fig. 10.10. This took silicon cell efficiency to 23% by the end of the 1980's [10.48], an enormous improvement over the figure of 17%, the highest value only 7 years earlier [10.49]. The PERL cell shares many features in common with the rear point contact cell, including almost complete enshroudment in a passivating oxide layer and small area contacts passified by local heavy diffusions. However, it is a more robust design, being more tolerant of poor surface passivation and poor bulk lifetimes.

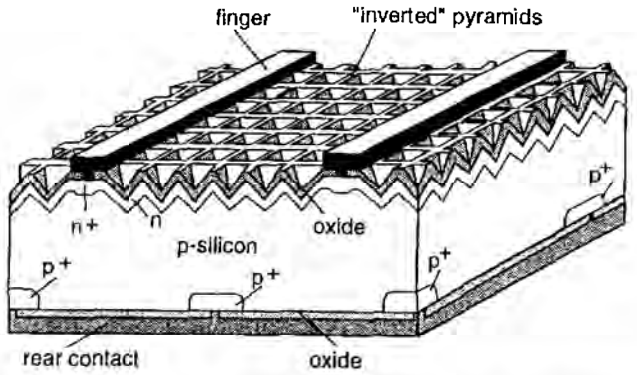


Figure 10.10: The PERL cell which took efficiency above 24% in the early 1990's.

Although both cells require several stages of photolithography making them unsuited for low cost terrestrial use, there has been some production experience with both designs for solar car racing. In 1993, the SunPower Corporation fabricated 7,000 rear contact cells using a

simplified stripe contact design [10.50]. This produced a good yield of 18 cm^2 cells of efficiency above 20% with a peak efficiency of 21.5% independently confirmed [10.50]. At the same time, the University of New South Wales produced over 1,000 cells, each 2.6 times larger (46 cm^2), with good yield of cells above 21% and a confirmed peak of 21.6% [10.51]. (These cells had finger lengths much longer than optimal to make them compatible with a lower cost, buried contact cell design). Early during the latter production, 16 cells were encapsulated to produce a nominally 30 cm x 30 cm module of a confirmed efficiency of 20.8%, the first non-concentrating photovoltaic module to exceed 20% efficiency. The rear contact cells were used to produce a nominally 20% efficient array for the Honda Dream, the solar car which won the 1993 World Solar Challenge, a demanding 3,000 km solar car race across Australia from Darwin to Adelaide [10.52]. Subsequently, an improved module efficiency of 21.6% was confirmed.

Since then, further improvements in PERL cells has taken their efficiency beyond 24%. Major improvements include: the growth of much thinner oxide for top surface passivation which allows the direct application of a double layer antireflection coating to increase short-circuit current [10.27]; the use of an alnealing sequence for this top oxide and localized top contact points to increase open-circuit voltage; and improved rear surface passivation and reduced metallization resistance to improve fill factor.

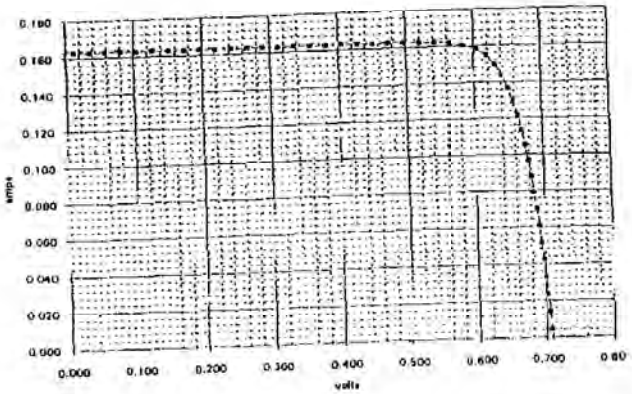


Figure 10.11: Output characteristics of a 24% efficient PERL cell.

The output characteristics of a 24% PERL cell are shown in Fig. 10.11. The cells display short-circuit current densities of 41 mA/cm^2, open-circuit voltages of 710 mV and fill factors of 83%. Incremental improvements in these parameters are expected to produce 25% cell efficiency without major changes in cell design. One obvious area for attention is the metallization shadowing. Several approaches have been suggested for steering light reflected from top surface metallization onto active cell area [10.53-10.56].

10.11 PERL CELL DESIGN

10.11.1 Optical features

To maximize cell performance, as much light as possible of useful wavelengths should be coupled into and absorbed by the cell. Modern cell designs such as the PERL cell of Fig. 10.10 incorporate several features of a primarily optical nature to achieve this result.

The inverted pyramids along the top surface serve primarily in such an optical role. Most light incident on this structure will hit one of the side walls of the pyramids at the first point of incidence with the majority of this light coupled into the cell. That reflected will be reflected downwards, ensuring that it has at least a second chance of entering into the cell. Some of the light incident near the bottom of the pyramids has three such chances. The pyramids are covered by an oxide layer of appropriate thickness to act as a quarter-wavelength antireflection coating. In more recent designs, this oxide is grown thin and a double layer antireflection coating applied [10.27].

Light coupled into the cell moves obliquely across the cell towards the rear surface with most absorbed on the way. Weakly absorbed light reaching the rear is reflected by the very efficient reflector formed by the combination of the rear oxide layer covered by an aluminium layer (Chapter 6). The reflectance from this combination depends upon the angle of incidence of the light and the thickness of the oxide layer, but is typically above 95% for angles of incidence close to the normal, decreasing to below 90% as the incidence angle approaches that for total internal reflection at the silicon/oxide interface (24.7°), and increasing to close to 100% once this angle is exceeded.

Light reflected from the rear then moves towards the top surface. Some reaching this surface strikes a face of a pyramid of opposite orientation to that which coupled it into the cell. Most of this immediately escapes from the cell. Light striking other faces of the pyramid is totally internally reflected. This results in about half the light striking the top surface internally at this stage being reflected back across the cell towards the rear contact. The amount of light escaping after the first double pass depends on the precise geometry involved. It can be reduced by destroying some of the symmetries involved, for example by using tilted inverted pyramids or by using the 'tiler's pattern' approach of Fig. 6.8. The latter approach is currently used in PERL cell designs.

The combination of the inverted pyramids and the rear reflector therefore forms a very efficient light-trapping scheme, increasing the pathlength of weakly absorbed light within the cell. Effective pathlength enhancement factors (Appendix G) above 40 are measured. The light trapping boosts the infrared response of the cell. The external responsivity (amps per watt of incident light) of PERL cells peaks at longer wavelengths at higher values than previous silicon cells with values of 0.75 A/W measured at 1.02 μm wavelength. Energy conversion efficiency under monochromatic light peaks at the same wavelength with values above 45% measured [10.57]. Further improvements could push this figure to above 50% at 1.06 μm.

Other optical losses are due to reflection from, and absorption in, the top metal fingers of the cell. This can be minimized by making these lines as fine as possible with, ideally, as large an aspect ratio (height to width ratio) as possible. Alternatively, optical approaches can be used to steer incoming light away from these lines or to ensure that light reflected from them eventually finds its way to the cell surface [10.53,10.56].

Present PERL cells lose about 5% of incoming light due to absorption or reflection loss associated with these metal fingers, when combined with reflection from the unmetallized top surface of the cell. They also lose 1-2% in performance from the use of a less than optimum light-trapping scheme and from less than 100% reflection of light from the rear surface of the cell. There is therefore some scope for small to moderate gains in performance by further improving the optical properties of these cells.

10.11.2 Electronic Features

10.11.2.1 Bulk Recombination

To obtain high cell performance, recombination throughout the cell has to be kept to a minimum. The advantages in producing increased output current are obvious. It makes no sense to waste photogenerated carriers by allowing them to recombine before being collected. Decreased recombination also increases the cell's voltage output. Any voltage across the cell produces increased internal carrier concentrations increasing internal recombination rates. On open circuit, the nett generation rate of carriers throughout the cell is balanced by the recombination rate due to this voltage bias effect. The cell open-circuit voltage is often a better indicator of recombination rates in the cell than the short-circuit current.

As apparent in Fig. 10.10 most of the PERL cell volume consists of uniformly doped bulk material, with surface regions divided into contacted and non-contacted areas. Recombination in bulk regions can be minimized by choosing as high a quality starting material as possible. Material quality is generally characterized by the minority carrier lifetime. The lower the dopant concentration in the substrate, generally the higher this lifetime will be. This is offset by a compensating effect of doping upon recombination rates. This compensation is due to the fact that the higher the dopant density, the lower the minority carrier concentration for any given voltage across the cell. The recombination rate is determined by the product of this concentration and the inverse of the carrier lifetime. For ideal silicon material, low dopant density is undoubtedly the best choice to minimize this product (Chapter 7). For actual material, several other issues are involved and the optimum dopant density depends upon the particulars of cell design. Obviously, the thinner the bulk region, the lower the bulk recombination will be. The trade-off here is a reduction in the mechanical strength and the light-absorbing capability of the cell. The light-trapping schemes previously mentioned push the optimum thickness to lower values than would otherwise prevail.

10.11.2.2 Surface Recombination

Recombination in non-contacted areas of the surface can be minimized by the growth of a high-quality thermal oxide. Conditions for producing low interface state densities have been well documented for microelectronics [10.58]. (Interface states are referred to, in that area, as "interface traps"). However, other properties simultaneously required for microelectronics, such as high oxide breakdown strength, would not appear as important for photovoltaics, giving scope for "customizing" growth conditions. Particularly interesting is the effect of surface doping type and doping level upon the recombination rate at the oxide interface.

The present consensus is that, for the highest-quality oxides, the capture cross-section of interface states for electrons is very much higher than the capture cross-section for holes [10.59]. This may be a fundamental physical property of these states. The large asymmetry implies that the states active in recombination may be electrostatically attractive to electrons but unattractive to holes, e.g., have donor-like properties with a positive charge state when unoccupied.

Regardless of the physical origin of the asymmetry, it produces different recombination properties for n-type and p-type surfaces. For n-type surfaces, there will usually be a small hole concentration at the surface. The capture of holes will therefore be the rate-limiting process determining surface recombination. The recombination rate will be very small due to the combination of small hole concentration and small hole capture cross-sections, as shown in Fig. 10.12(a).

The situation for p-type surfaces is more complex. Here, hole concentrations will tend to be large, although electron concentrations can be small. The latter will increase as the voltage output of the cell increases. At low voltages, the capture of electrons will be the rate-limiting process as suggested by Fig. 10.12(b). Recombination processes will be much more effective than in n-type material at these voltages due to the larger electron capture cross section. However, as the voltage across the cell builds up, a transition will eventually occur when hole capture becomes the rate-limiting process. Since the hole concentration at the surface will not increase as rapidly, in relative terms, as that of electrons in the bulk of the cell, the result is a rapid reduction in the effective surface recombination velocity with

increasing cell voltage. Eventually, recombination rates will become similar to those of n-type material at any given large voltage.

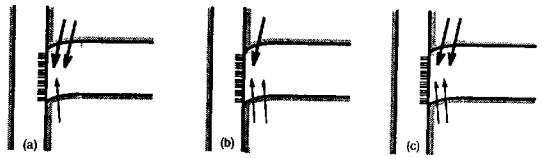


Figure 10.12: Surface recombination resulting from asymmetrical capture cross sections for electrons and holes. The probability of capture depends on both the capture cross section of the interface states and the interface concentrations of the respective carriers. The widths of the arrows represent the probability contribution from the former, while the number of arrows indicates that from the latter. The overall surface recombination rate is determined by the weakest link in terms of the weight of arrows: (a) n-type silicon at low cell voltages, where hole capture is the rate-limiting process; (b) p-type silicon a low cell voltages, where electron capture can be rate limiting; (c) n-type and p-type silicon at high cell voltages, where hole capture is rate limiting.

This effect was first analysed by Eades and Swanson [10.60], assuming "flat-band" (zero-field) conditions at the cell surfaces. The tendency for p-type surfaces to be depleted either by the nett positive charge in the oxide or by work function differences between p-type silicon and metals such as aluminium and titanium which may overlie oxides, will help make this effect apparent at lower cell voltage than predicted by such a flat-band treatment.

For the present PERL cells, this effect is particularly important for the non-contacted regions of the rear surface. The effective recombination velocity in these regions decreases from very large values of the order of 10^4 cm/s to low values below 30 cm/s as the voltage across the cell increases from the short-circuit to the open-circuit voltage point. A major consequence can be a lower cell fill factor than would otherwise be the case [10.61]. Examination of the dark current-voltage characteristics of PERL cells has allowed the change in this recombination velocity to be determined as a function of voltage across the cell [10.61]. Similar measurements confirming a steadily reducing

surface recombination velocity with injection level have also been reported upon unmetallized p-type silicon surfaces [10.59].

The full implications of such asymmetrical capture cross-sections for cell design have not yet been determined. Further work is required to gain confidence that the effects described will not be overridden by additional effects not identified in the work mentioned above. For example, earlier results by Yablonovitch et al. [10.62], investigating the effect of surface electrostatic conditions on surface recombination, also confirmed the existence of a set of states with large electron to hole capture cross-section ratios. However, in this case, a second set of states was found with much larger hole capture cross-sections than electron capture cross-sections. This would be the property expected from acceptor-type states (negatively charged when occupied). A mitigating factor may be that the substrate doping was higher than in the other work mentioned. Also, fabrication details may be important in determining the situation prevailing at any given interface (for example, there was no "alnealing" step in the cited work [10.62]).

Assuming larger electron capture cross-sections than those for holes, the design rule for non-diffused surfaces is to keep hole concentrations at the surface to a minimum. This can be effected by using n-type surfaces or by depleting hole concentrations at p-type surfaces, either electrostatically, by positive oxide charge or low work function metallic capping layers as at the rear of PERL cells, or by dopant depletion as occurs during silicon oxidation [10.58].

10.11.2.3 Contact Area Recombination

The regions where metal contact to the cell is made are regions of potentially very high recombination. Two strategies are used in the PERL cell of Fig. 10.10 to minimize such recombination. One is simply to keep the contact area small. For example, the top metal contact to the PERL cell is made at narrow stripes through the top surface oxide of only 3 μm width, or through discrete contact holes, while the rear metal contact is made through 10 μm x 10 μm contact holes normally spaced 250 μm apart. This means that metal contact is made to only 0.4% or less of the top surface area of the cell and 0.2% of the rear surface cell. The second strategy is to heavily diffuse these contact areas. Such heavy diffusion suppresses the minority carrier concentration in the contact areas, reducing contact recombination rates. This is the same effect as the "back surface field effect" discussed

in connection with Fig. 10.2(b).

As previously noted, (Chapter 9), other techniques have also proved effective in reducing contact recombination, although not frequently used in present cell design. One is based on the use of tunnelling metal-insulator-semiconductor contacts [10.28]. The others are somewhat related in that tunnelling processes may also be involved in transport across the contact. These are based on the use of semi-insulating polysilicon (SIPOS) contacts [10.39] or doped polycrystalline or amorphous silicon contacts to the silicon substrate [10.35].

10.11.2.4 Present Recombination Relativities

The author's assessment of the recombination balance in present PERL cells is along the following lines. Bulk recombination can be made small in present designs with appropriate choice of substrate and processing conditions, but is a reasonably sized component at all cell voltages. Rear surface recombination in non-contacted areas is not important at open circuit but is important at the maximum power point voltage, due to the dependencies on cell voltage previously mentioned. This recombination can become apparent in the cell characteristics as reduced fill factor. At the open-circuit voltage, recombination at the surface of the top diffused layer including its contact region appears the most important.

On-going improvement in cell design and fabrication technologies should see bulk recombination eventually become the dominant recombination component.

10.12 SUMMARY

The progress outlined in this Chapter is summarized in Table 10.1. On-going improvements are expected to see efficiency above 25% reached without major structural changes. Further progress depends upon the generation of new ideas, such as outlined in Chapter 8.

Device performance is entering the regime where Auger recombination constraints are starting to make their presence felt. Improvements in post-processing bulk material quality and in surface passivation should allow the Auger limiting performance to be approached quite closely. Coincidentally, an improvement of about 4% in each of the three key parameters, the open-circuit voltage, the short-circuit current density and the fill factor, appears feasible. Once these

fundamental limits are more closely approached, it may be possible to incrementally engineer material properties to extract further efficiency improvements. For example, directional strain can remove the valence band degeneracies near the Brillouin zone centre previously noted, as well as shifting the six equivalent conduction band minima of Fig. 2.6 with respect to one another. This would modify the density of allowed states, hence n_i, the Auger coefficients and the absorption coefficient.

Table 10.1: Evolution of silicon solar cell efficiency (> 1 cm^2 area) nominally under the IEC 904 global or ASTM E892-87 global AM1.5 spectrum at 25°C and 1000 W m^{-2} illumination intensity.

DATE*	EFFIC. (%)	CELL STRUCTURE	ORGANIZATION	REF.
3/41	<1%	Melt grown junction	Bell Labs.	10.3
3/52	~1%	He bombardment	Bell Labs.	10.4
~12/53	~4.5%	Li diffused wraparound	Bell Labs.	10.6
1/54	~6%	B diffused wraparound	Bell Labs.	10.5
11/54	~8%	B diffused wraparound	Bell Labs.	10.7
5/55	~11%	B diffused wraparound	Bell Labs.	10.7
~12/57	12.5%	0.5 x 2 cm B diffused	Hoffman Elec.	10.61
8/59	14%	Grid-contact B diffused	Hoffman Elec.	10.61
8/61	14.5%	B diff. AR coat, gridded	Commercial, USASRDL	10.11
1/73	15.2%	Violet cell	Comsat Labs.	10.22
9/74	17.2%	Textured non-reflecting	Comsat Labs.	10.23
9/83	18.0%	MINP cell	UNSW	10.49
12/83	18.3%	PESC cell	UNSW	10.49
5/85	19.0%	PESC cell	UNSW	10.49
10/85	20.0%	Microgrooved PESC	UNSW	10.49
7/86	20.6%	Microgrooved PESC	UNSW	10.49
4/88	20.8%	Microgrooved PESC	UNSW	10.49
9/88	22.3%	Rear point contact cell	Stanford Uni.	10.49
12/89	23.0%	PERL cell	UNSW	10.49
2/90	23.1%	PERL cell	UNSW	10.49
2/94	23.5%	PERL cell	UNSW	10.63
9/94	24.0%	DLAR PERL cell	UNSW	10.64

* Date of submission or presentation of paper reporting result of independent efficiency confirmation (month/year).

REFERENCES

10.1 F. Braun, "On conductance in metal sulphides", Ann. Phys. Lpz, Vol. 153, p. 556, 1874.

10.2 H.C. Torrey and C.A. Whitmer, "Crystal Rectifiers", (New York: McGraw-Hill), 1948, pp. 5-11.

10.3 R.S. Ohl, "Light sensitive electric device", US Patent 240252, filed 27 March 1941, "Light-sensitive electric device including silicon", US Patent 2443542, filed 27 May 1941.

10.4 E.F. Kingsbury and R.S. Ohl, "Photoelectric properties of ionically bombarded silicon", Bell Syst. Tech. J., Vol. 31, p. 8092, 1952.

10.5 D.M. Chapin, C.S. Fuller and G.L. Pearson, "A new silicon p-n junction photocell for converting solar radiation into electrical power", J. Appl. Phys., Vol. 8, p. 676, 1954.

10.6 G.L. Pearson, 1985, PV founders award luncheon, Conf. Record, 18th IEEE Photovoltaic Specialists Conf., Las Vegas, 1985 (New York: IEEE).

10.7 Bell Labs. Record, November, 1954, p. 436: Bell Labs. Record, May, 1955, p. 166.

10.8 Sharp Solar Battery S-224, Sharp Corporation, Osaka, Japan.

10.9 R.N. Hall and T.J. Soltys, "Polka-dot Solar Cell", Conference Record, 14th IEEE Photovoltaic Specialists Conference, San Diego, 1980, p. 550.

10.10 M. Wolf, "Limitations and Possibilities for Improvement of Photovoltaic Solar Energy Converters", Proceedings of the IRE, Vol. 48, pp. 1246-1263, 1960.

10.11 J. Mandelkorn, C. McAfee, J. Kesperis, L. Schwartz and W. Pharo, "Fabrication and Characteristics of Phosphorus-Diffused Silicon Solar Cells", Journal of the Electrochemical Society, pp. 313-318, 1962.

10.12 K.D. Smith, H.K. Gummel, J.D. Bode, D.B. Cuttriss, R.J. Nielson and W. Rosenzweig, "The Solar Cells and their Mounting", Bell Sys. Tech. J., Vol. 41, pp. 1765-1816, 1963.

10.13 R. Gereth, H. Fischer, E. Link, S. Mattes and W. Pschunder, "Contribution to the Solar Cell Technology", Energy Conversion, Vol. 12, pp. 103-107, 1972.

10.14 H.R. Phillip, Journal of the Physics and Chemistry of Solids, Vol. 342, p. 1935, 1971.

10.15 P.A. Iles, "Increased Output from Silicon Solar Cells", Conference Record, 8th IEEE Photovoltaic Specialists Conference, Seattle, 1970, pp. 345-352.

10.16 R., Gereth, H. Fischer, E. Link, S. Mattes and W. Pschunder, "Silicon Solar Technology of the Seventies", Conf. Record, 8th IEEE Photovoltaic Specialists Conf., Seattle, 1970, p. 353.

10.17 R.L. Cummerow, "Use of p-n Junctions for Converting Solar Energy to Electrical Energy", Phys. Rev., Vol. 95, p. 561, 1954.

10.18 M. Wolf, "Drift Fields in Photovoltaic Solar Energy Conversion", Proceedings of the IEEE, Vol. 51, pp. 674-593, 1963.

10.19 J. Mandelkorn, and J.H. Lamneck, "A New Electric Field Effect in Silicon Solar Cells", J. Appl. Phys., Vol. 44, p. 4785, 1973.

10.20 M.P. Godlewski, C.R. Baraona and H.W. Brandhorst, "Low-High Junction Theory Applied to Solar Cells", 10th IEEE Photovoltaic Specialists Conf., Palo Alto, 1973, pp. 40-49.

10.21 J.C.C. Tsai, "Shallow Phosphorus Diffusion Profiles in Silicon", Proceedings of the IEEE, Vol. 57, pp. 1499-1506, 1969.

10.22 J. Lindmayer, and J. Allison, "The Violet Cell: An Improved Silicon Solar Cell", COMSAT Tech. Rev., Vol. 3, pp. 1-22, 1973.

10.23 J. Haynos, J. Allison, R. Arndt and A. Meulenberg, "The Comsat Non-Reflective Silicon Solar Cell: A Second Generation Improved Cell", Int. Conference on Photovoltaic Power Generation, Hamburg, September, 1974, p. 487.

10.24 H.G. Rudenberg and B. Dale, "Radiant Energy Transducer", US Patent 3,150,999 (filed 17 February, 1961).

10.25 D. King and M.E. Buck, "Experimental Optimization of an Anisotropic Etching Process for Random Texturization of Silicon Solar Cells", Conf. Record, 22nd IEEE Photovoltaic Specialists Conf., Las Vegas, 1991, pp. 303-308.

10.26 E.S. Rittner and R.A. Arndt, "Comparison of Silicon Solar Cell Efficiency for Space and Terrestrial Use", Journal of Applied Physics, Vol. 47, pp. 2999-3002, 1976.

10.27 J. Zhao and M.A. Green, "Optimized Antireflection Coatings for High Efficiency Silicon Solar Cells", IEEE Trans. Electron Devices, Vol. 38, pp. 1925-1934, 1991.

10.28 R.B. Godfrey and M.A. Green, "655 mV Open Circuit Voltage, 17.6% Efficient Silicon MIS Solar Cells", Applied Physics Letters, Vol. 34, pp. 790-793, 1979.

10.29 R. Hezel, W. Hoffmann and K. Jaeger, "Recent Advances in Silicon Inversion Layer Solar Cells and Their Transfer to Industrial Pilot Production", 10th European Photovoltaic Solar Energy Conf., Lisbon, April, 1991, pp. 511-514.

10.30 J.G. Fossum and E.L. Burgess, "High Efficiency p^+ n n^+ Back-Surface-Field Silicon Solar Cells", Applied Physics Letters, Vol. 33, pp. 238-240, 1978.

10.31 M.A. Green, "Enhancement of Schottky Solar Cell Efficiency above its Semiempirical Limit", Applied Physics Letters, Vol. 28, pp. 287-268, 1975.

10.32 J. Lindmayer and J.F. Allison, "Dotted Contact Fine Geometry Solar Cell", U.S. Patent 3,982,964, Sept. 1976.

10.33 R.A. Arndt, A.. Meulenberg and J.F. Allison, "Advances in High Output Voltage Silicon Solar Cells", Conf. Record, 15th IEEE Photovoltaic Specialists Conf., Orlando, 1981, pp. 92-96.

10.34 M.A. Green, A.W. Blakers, J. Shi, E.M. Keller and S.R. Wenham, "High-Efficiency Silicon Solar Cells", IEEE Trans. on Electron Devices, Vol. ED-31, pp. 671-678, 1984.

10.35 F.A. Lindholm, A. Neugroschel, M. Arienze and P.A. Iles, "Heavily Doped Polysilicon - Contact Solar Cells", Electron Device Letters, Vol. EDL-6, pp. 363-365, 1985.

10.36 E. Yablonovitch, T. Gmitter, R.M. Swanson and Y.H. Kwark, "A 7209 mV Open Circuit Voltage, SiO_X:c-Si:SiO_X Double Heterostructure Solar Cell", Applied Physics Letters, Vol. 47, pp. 1211-1213, 1985.

10.37 P. Van Halen, P and D.L. Pulfrey, "High-Gain Bipolar Transistors with Polysilicon Tunnel Junction Emitter Contacts", IEEE Trans. on Electron Devices, Vol. ED-32, p. 1307, 1985.

10.38 M.A. Green, A.W. Blakers and C.R. Osterwald, "Characterization of High-Efficiency Silicon Solar Cells", Journal of Applied Physics, Vol. 58, pp. 4402-4408, 1985.

10.39 R.D. Thompson, and K.N. Tu, "Low Temperature Gettering of Cu, Ag and Au Across a Wafer of Si by Al", Applied Physics Letters, Vol. 41, pp. 440-442, 1982.

10.40 A.W. Blakers and M.A. Green, "20% Efficiency Silicon Solar Cells", Applied Physics Letters, Vol. 48, pp. 215-217, 1986.

10.41 T. Saitoh, T. Uematsu, T. Kida, K. Matsukuma and K. Morita, "Design and Fabrication of 20% Efficiency, Medium-Resistivity Silicon Solar Cells, Conf. Record, 19th IEEE Photovoltaic Specialists Conf., New Orleans, 1987, pp. 1518-1519.

10.42 W.T. Callaghan, Evening presentation on Jet Propulsion Lab. Photovoltaic activities, Seventh E.C. Photovoltaic Solar Energy Conf., Sevilla, Oc., 1986.

10.43 S. Khemthong, S. Cabaniss, J. Zhao and A. Wang, "Low Cost Silicon Solar Cells with High Efficiency at High Concentrations", Conf. Record, 22nd IEEE Photovoltaic Specialists Conf., Las Vegas, 1991, pp. 268-272.

10.44 K. Fukui, Y. Fukawa, H. Takahashi, K. Okada, M. Takayama, K. Shirasawa and H. Watanabe, "Large Area High Efficiency

Single Crystalline Silicon Solar Cell", Tech. Digest, Int. PVSEC--7, Nagoya, Japan, 1993, pp. 87-88.

10.45 R.A. Sinton, Y. Kwark, J.Y. Gan and R.M. Swanson, "27.5% Si Concentrator Solar Cells", Electron Device Letters, Vol. EDL-7, p. 567, 1986.

10.46 R.R. King, R.A. Sinton and R.M. Swanson, "Front and Back Surface Fields for Point-Contact Solar Cells", Conf. Record, 20th IEEE Photovoltaic Specialists Conf., Las Vegas, September, 1988, pp. 538-544..

10.47 A.W. Blakers, A. Wang, A.M. Milne, J. Zhao, X. Dai and M.A. Green, "22.6% Efficient Silicon Solar Cells", Proceedings, 4th International Photovoltaic Science and Engineering Conference, Sydney, February, 1989, pp. 801-806.

10.48 J. Zhao, A. Wang and M.A. Green, "24% Efficient PERL Structure Silicon Solar Cells", 21st IEEE Photovoltaic Specialists Conf., Orlando, May, 1990, pp. 333-335.

10.49 M.A. Green, "Recent Advances in Silicon Solar Cell Performance", Proc. 10th European Communities Photovoltaic Solar Energy Conf., Lisbon, April, 1991 (Kluwer Academic Publishers, Dordrecht), pp. 250-253.

10.50 P.J. Verlinden, R.M. Swanson and R.A. Crane, "7000 High-Efficiency Cells for a Dream", Progress in Photovoltaics, Vol. 2, pp. 143-152, 1994.

10.51 J. Zhao, A. Wang, M. Taouk, S.R. Wenham and M.A. Green, "20% Efficient Photovoltaic Module", Electron Device Letters, Vol. EDL-14, pp. 539-541, 1993.

10.52 M.A. Green, "World Solar Challenge 1993: The Trans-Australian Solar Car Race", Progress in Photovoltaics, Vol. 2, pp. 73-79, 1994.

10.53 M.A. Green, J. Zhao, A.W. Blakers, M. Taouk and S. Narayanan, "25-Percent Efficient Low-Resistivity Silicon Concentrator Solar Cells", IEEE Electron Device Letters, Vol. EDL-7, pp. 583-585, 1986.

10.54 A.W. Blakers, P.B. Kosel, M.R. Willison and M.A. Green, "Fabrication of Thick Narrow Electrodes on Concentrator Solar Cells", J. Vac. Sci. Tech., Vol. 20, pp. 13-15, 1982.

10.55 P.A. Iles, "A Survey of Grid Technology", Conf. Record, 16th IEEE Photovoltaic Specialists Conf., San Diego, 1982, p. 340.

10.56 A. Cuevas, R.A. Sinton and R.M. Swanson, "Point- and Planar-Junction P-I-N Silicon Solar Cells for Concentration Applications, Fabrication, Performance and Stability", Conf. Record, 21st IEEE Photovoltaic Specialists Conf., Kissimimee, May, 1990, pp. 327-332.

10.57 M.A. Green, J. Zhao, A. Wang and S.R. Wenham, "45% Efficient Silicon Photovoltaic Cell Under Monochromatic Light", IEEE Electron Device Letters, Vol. 13, pp. 317-318, 1992.

10.58 P. Balk (ed.), "The Si-SiO_2 System", (Elsevier, Amsterdam), 1988.

10.59 A. Aberle, S. Glunz and W. Warta, "Impact of Illumination Level and Oxide Parameters of Shockley-Read-Hall Recombination at the Si-SiO_2 Interface", J. Appl. Phys., Vol. 71, p. 4422, 1992.

10.60 W. Eades and R. Swanson, "Calculation of the Surface Generation and Recombination Velocities at the Si-SiO_2 Interface", J. Appl. Phys. Vol. 58, p. 4267, 1985.

10.61 M.A. Green, S.R. Wenham, J. Zhao, A. Wang, X. Dai, A. Milne, M. Taouk, J. Shi, F. Yun, B. Chan, A.B. Sproul and A. Stevens, "One-Sun Silicon Solar Cell Research", Final Report, Sandia Contract 66-5863, 1992.

10.62 E. Yablonovitch, R.M. Swanson, W.D. Eades and B.R. Weinberger, "Electron-Hole Recombination at the Si-SiO_2 Interface", Appl. Phys. Lett., Vol. 48, p. 245, 1986.

10.63 J. Zhao, A. Wang and M.A. Green, "23.5% Efficient Silicon Solar Cell", Progress in Photovoltaics, Vol. 2, pp. 227-230, 1994.

10.64 M.A. Green, K. Emery, K. Bücher and D.L. King, "Solar Cell Efficiency Tables (Version 5), Progress in Photovoltaics, Vol. 3, pp. 51-55, 1995.

Chapter
11

SCREEN-PRINTED AND BURIED CONTACT CELLS

11.1 INTRODUCTION

The evolution of cell design for commercial flat plate product has followed a different course than that for laboratory cells. Prior to the mid-1970's, there was virtually no market for terrestrial photovoltaic cells. Product that was available generally used space cell technology for cell fabrication.

With the oil embargo of the early 1970's, interest in terrestrial cells increased. The driving force for the evolution of commercial product was the US Government's photovoltaic program [11.1]. In particular, a series of bulk or "block" purchases of cells stimulated the development of commercial manufacturing and the standardization of product. Between 1975 and 1983, the US government purchased Blocks I-V of photovoltaic product with increasingly stringent acceptance criteria. This, combined with targeted research and development activities, was very effective in moulding the development of the photovoltaic industry.

The first "Block I" purchase of modules reflects the diversity of product and design approaches investigated in the early 1970's. One company supplied cells fabricated on 7.5 cm diameter wafers using essentially space cell technology. A second company used metal contacts formed by plating nickel followed by solder dipping. A third company,

Spectrolab Inc., used a new technique based on screen printing of metal pastes onto the cell surface [11.2].

A variety of module encapsulation approaches were also used. In the Block II purchase in 1976, Spectrolab combined the screen printing approach of their Block I cells with a laminated module design similar to the lamination process used in automobile windscreen glass. Over the next decade, this approach became the standard for all volume manufacturers of cells [11.3].

The strength of this approach was the simplicity of the cell processing sequence and the availability of suitable equipment from the thick film microelectronics industry for screen printing and firing operations. However, despite attempts to decrease the linewidth obtained with this approach, achievable linewidth remains a major limitation of the approach. In the mid-1980's, a new approach, the buried contact approach, based on defining the metal contact shape by burying it in grooves located in the cell surface was developed [11.4]. This technology is presently either being used in production or under development by most major cell manufacturers, and due to the substantial performance margin over the screen printed approach, may eventually displace screen printing.

In this Chapter, both of these contending technologies are described as is likely evolution over the coming years.

11.2 SCREEN-PRINTED CELLS

11.2.1 Structure

Figure 11.1 shows the structure of a typical crystalline screen-printed cell. The normal cell processing sequence would consist of [11.5]: saw damage removal from the starting wafer by etching; chemical texturing of the top surface, if a (100) crystalline wafer were the starting material; top surface diffusion to about 40 Ω/square; edge junction isolation normally by "coin stacking" the cells and etching the edges in a plasma; etching to remove diffusion oxides; screening of front metal paste through a suitably patterned screen; drying and firing of the front surface metallization; screening of the rear surface metal paste; drying and firing of rear metal contact; cell testing and sorting.

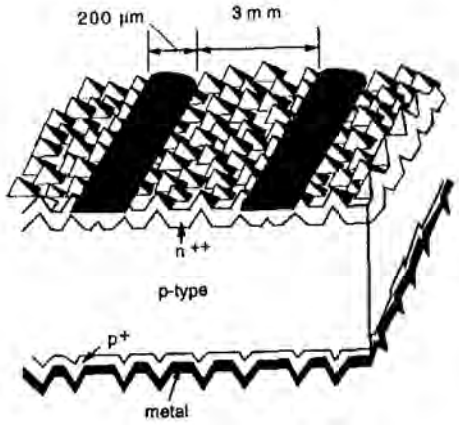


Figure 11.1: Screen printed crystalline silicon solar cell (not to scale).

Using the normal boron doped, "solar grade" Czochralski silicon wafers of 0.5-5 Ω cm resistivity, the resulting cell efficiency is typically 12-14%. Application of a antireflection coating (usually TiO_2 or Si_3N_4) gives about 4% relative improvement.

For multicrystalline substrates, the use of an antireflection coating is mandatory due to the inability to reduce reflection substantially by texturing the multicrystalline wafer surface. This is due to the random orientations of the grains in the multicrystalline material which results in only a fraction being suitable for texturing.

The major disadvantages of the approach relate to the cost of the metal pastes used in the process and the relatively low cell efficiency which results. The latter is due most fundamentally to the restricted linewidth possible by screen printing. The relatively high contact resistance between the paste and the silicon is another constraint. The low aspect ratio (height/width) of the final lines due to paste thickness shrinkage during firing is another problem compounded by the low conductivity of the fired paste (about 3 times lower than that of pure silver).

There have been several investigations of the feasibility of screening pastes other than those based on silver. Nickel and copper have been investigated without success [11.6].

To reduce the linewidth, special fine screens can be used. However, the screens have been too frail for use in commercial production, although often used to produce a good research result [11.7].

The contact resistance between the paste and silicon can be a sensitive function of the precise firing environment and temperature. The glass frit (dispersed glass particles used in the paste as a binder) forms an oxide precipitate along the interface between the screened paste and the silicon surface. This contributes to the high contact resistance, although often, phosphorus is added to the paste to decrease the contact resistance to n-type material. Etching of the top surface with HF after firing is known to decrease the contact resistance, presumably by etching away some of the interfacial frit in this area. However, this is also considered to reduce the reliability of the cell in a moist environment.

The rear surface contact resistance is generally less of a problem. Even though contact is being made to more lightly doped material, a much larger contact area is available. Furthermore, the addition of aluminium to the silver paste or the use of an aluminium paste precursor can increase the doping level in the surface region by alloying. Under appropriate firing conditions, a significant "back surface field" effect can be obtained by the use of such aluminium.

11.2.2 Typical Performance

Typically, the screen printing approach will produce cell open circuit voltages in the 580-620 mV range, depending on substrate resistivity, short circuit current densities in the 28-32 mA/cm^2 range, and fill factors for large area cells in the 70-75% range. For a large area cell, typically 10-15% of the top surface of the cell will be shaded by the screened metallization which, as indicated in Figure 11.1, typically consists of metal fingers of about 200 microns width, spaced about 2-3 mm apart. Due to the low conductivity of the paste, an interconnect busbar design, as indicated in Figure 11.2, is mandatory for large area cells. Although contributing to the large shading loss of this approach, this design also has the advantage of improving the cell tolerance to cracks. If scaling to large area cells, the number of busbar interconnections would have to be increased.

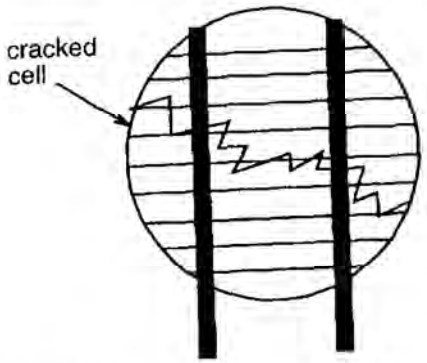


Figure 11.2: Cell design using the strip metal cell interconnects as busbars to reduce finger resistive losses and to improve tolerance to cracks.

To maintain reasonable contact resistance, quite low sheet resistivities for the top surface diffusion are required. The 40 Ω/square typically used results in a significant loss in blue response of the cells due to dead layers along the surface as discussed in Section 10.5. Higher sheet resistivities will improve the blue response but at the expense of cell fill factor (see Fig. 13.3). The heavy diffusion also limits the open-circuit voltage output of the cells. Oxide surface passivation is not of much benefit in improving performance due to this limitation. Using improved quality substrates such as floatzone silicon also generally does not result in any substantial performance improvement again due to this limitation.

11.2.3 Improved Technology

The limitations of the screen printing approach may not be fundamental to this approach but may be able to be overcome by introducing new ideas.

To reduce the linewidth, finer screens can be used although these require weaker material in their construction and have not been sufficiently durable for volume manufacturing. There are frequently alternative claims in this area [11.7], but commercial practice is a telling indicator of what is feasible here. Approaches for defining metal contacts, similar to ink jet printing approaches, have also been used in commercial production.

Some recent progress has been reported in improving the contact resistance obtainable by screen printing, although details are not available [11.7,11.8]. Different paste formulations and/or firing conditions are most likely responsible. Approaches similar to those shown in Fig. 11.3 have also been suggested which rely on having different top layer sheet resistivities in contacted and non-contacted areas [11.9,11.10]. A conductive antireflection coating such as formed by conducting metal oxides could be used in conjunction with this scheme to allow reasonable metal spacing [11.11].

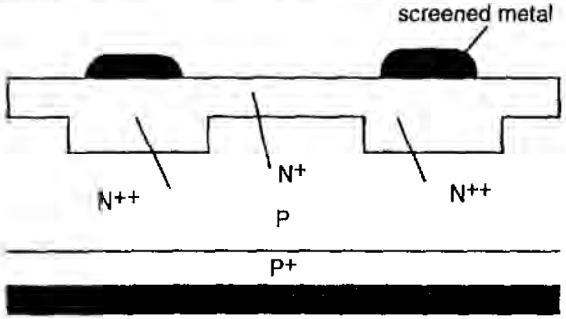


Figure 11.3: Ideal situation for fine linewidth screen printed metallization with contact being made to selectively doped areas.

However, it is doubtful that a high efficiency cell can ever be produced using the screen printed approach, with good screen printed laboratory cells only giving about 16.7% efficiency [11.7]. Even if both the linewidth and the contact resistance problems are successfully solved in production, there is still the problem with relatively poor paste conductivity and small aspect ratio.

11.3 BURIED CONTACT SOLAR CELLS

11.3.1 Structure

The buried contact solar cell of Figure 11.4 was developed to overcome the efficiency limitations of the screen printed cell approach previously described. The most distinctive feature of the cell design is the use of grooves in the top surface to locate the cell metallization. Although originally investigated using screen printed metallization sequences (where the metal was forced into the groove during the screening operation), the most successful designs have used electrolessly plated

metal contacts [11.12].

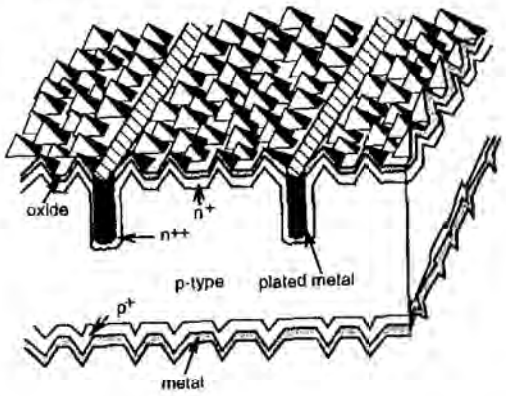


Figure 11.4: Buried contact solar cell.

Cell processing bears some resemblance to the screen printing sequence previously described. After saw damage removal and texturing, the surface is lightly diffused and an oxide grown over the entire surface. This oxide serves multiple purposes during cell processing and is the key to the relative simplicity of the processing. Note that there is no need to remove the diffusion oxide as in the screen printed approach. Grooves are then cut into the top cell surface either using a laser scribing machine, mechanical cutting wheels, or other mechanical or chemical approaches.

After cleaning of the grooves by chemical etching, these are subject to a second phosphorus diffusion, much heavier than the first. This produces selective doping in the contact areas (previously discussed as desirable in connection with screen printed cells and as used in high efficiency silicon PERL cells). Aluminium is then deposited on the rear surface by evaporation, sputtering, screen printing or plasma deposition.

After firing of the aluminium and etching to remove oxides, cell metallization is then completed by electroless plating of a nickel/copper/silver layer. A thin layer of nickel is first deposited. This is then fired and a substantial thickness of copper then deposited. Finally, the thin layer of silver is formed on the top surface by displacement plating. All these processes are electroless meaning that canisters containing the wafers are simply immersed in the plating

solution.

An improved sequence uses Si_3N_4 in lieu of the oxide during the processing [11.13]. This layer withstands high temperature steps while giving better antireflection properties in the final cell. BP Solar have reported excellent results with this approach [11.13-11.15].

11.3.2 Performance Analysis

The buried contact cell gives substantial performance advantage over screen printed cells. Figure 11.5 shows the comparison reported by BP Solar, using identical starting substrate material. Approximately 30% performance advantage is reported. At the same time, BP Solar report that processing costs ***per unit area*** are virtually identical, within 4% of that of the screen printed cell [11.14]. This gives a much lower cost/Watt, given the higher power output per unit area. Although capital costs are higher, the lower material costs compensate.

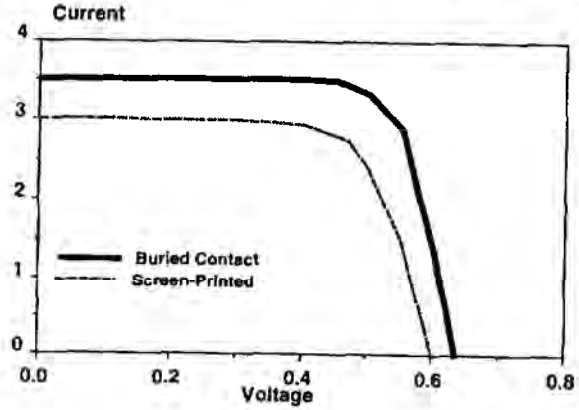


Figure 11.5: Output characteristics of buried contact cells compared to screen printed cells [after 11.15].

There are several reasons for this improved performance. The higher fill factor is due to the better conductance of the metallization fingers and the lower contact resistance between these and the heavily doped grooved regions. The higher voltage is due to the high sheet resistivity of the diffusion over the top surface, combined with the excellent surface passivation by the overlying oxide in these areas, and with the contact passivation provided by the heavy doping in the grooved areas.

An open-circuit voltage approaching 700 mV has been demonstrated for this combination, close to the highest ever demonstrated for laboratory silicon cells [11.16].

The high current output is due to the relatively low top surface shading feasible with this approach even in large area cells. This is a result, most fundamentally, of the high aspect ratio possible with buried contacts. Aspect ratios as high as 5:1 have been demonstrated, although not essential in some metallization design approaches. Low metallization linewidths of 15-20 μm are feasible with laser grooving and linewidths of 40 μm are feasible with mechanical approaches. The other contributor to the improved output current is the improved blue response resulting from the almost ideal surface properties in non-contacted areas.

The processing sequence has also shown itself capable of producing considerable gettering benefits during processing. The damage during the grooving process appears to be beneficial. As noted in Chapter 9, laser damage can produce effective gettering when applied to the rear of the wafers. Similarly, the laser grooves on the top surface might be expected to be effective gettering sites. One of the advantages of the buried contact sequence is that after grooving, the top surface is subjected to a heavy diffusion in the grooved areas. The phosphorus will diffuse preferentially in damaged areas and automatically passivate damage introduced by the grooves. Direct evidence for this effect has been observed [11.17]. Aluminium on these cells provides another well established gettering strategy as does heavy phosphorus diffusion as used in the grooved areas [11.18].

11.3.3 Production Experience

Buried contact solar cell technology has been licensed to several major cell manufacturers, with pilot production experience reported by some. A high efficiency array was fabricated by Telefunken [11.19] for the Swiss car "Spirit of Biel", which convincingly won the 1990 World Solar Challenge, the solar car race from Darwin to Adelaide. Array efficiency was 17%, then, the highest ever for silicon. The array gave 25% more power than that of the second placed car, which used enhanced screen printing technology [11.20].

BP Solar has reported on both manufacturing yields and process economics [11.13]. Using the same "solar grade" CZ substrates as in

their screen printing process, BP reports substantial efficiency improvement for the technology (circa 30%) and cell efficiencies of 17.5-18%. Economic analysis shows that the approach, as developed by BP with nitride antireflection coating, is well suited for polycrystalline material giving module manufacturing costs below US$3/peak Watt [11.13]. BP Solar supplied modules for the first reasonably sized installation using buried contact technology, a 20 kW system powering the Marzili furnicular railway in Berne. This was the most efficient flat-plate system of this size installed up to this time [11.21]. BP Solar also supplied 550 kW of these modules for the 1 MW Union Fenosa system near Toledo in Spain [11.22]. When it began operation in 1994, this was Europe's largest PV installation. In 1994, BP Solar launched the Saturn 585 module, an 85 W module based on 123 mm square buried contact solar cells as its "top-of-the-line" commercial product [11.23].

Solarex has reported preliminary work using mechanical dicing wheels to form the grooves [11.24]. Experiments at UNSW with 35 ganged dicing blades have produced grooves of 2% depth uniformity over the wafer surface with a processing time of 3 s/cell. The attraction of this approach is lower equipment costs, although consumable costs are higher than with laser grooving. A small pilot production line operated by Unisearch Ltd. in conjunction with UNSW has also given good yields of laser grooved cells with efficiencies of 19-20% demonstrated in production volumes of 10,000 cells per year [11.25].

The consensus of these pilot line and production studies is that the buried contact process, when transferred into production, can give efficiency margins of 25-40% over screen printing. Although more processing steps are involved than in the simplest screen printing approach, expensive silver pastes are eliminated so that processing costs per unit area are not greatly different, with costs per watt of product lower [11.26]. Marketing experience has shown that higher selling prices are feasible for this product due to the lower balance of systems costs in installed systems and the perceived higher quality due to the superior performance.

11.3.4 Future Improvement

A further advantage of the buried contact sequence over the screen printed is that it offers scope for transferring recent laboratory cell developments of Chapter 10 into low cost commercial production.

While the standard or first generation device of Fig. 11.4 is equivalent to a PESC cell, the double-sided grooved or bifacial buried contact cell shown in Fig. 11.6 is the equivalent of the subsequent PERL cell. It holds the promise of further simplifying buried contact cell processing while increasing efficiencies to around 21% for large cells. Both Al deposition and alloying steps and the need for edge junction isolation are eliminated, but an additional boron diffusion is introduced. The cell also responds to light from both directions. This allows use in modules with transparent rear backings with about 20% additional power expected in some applications [11.27].

As well as incorporating the front surface passivation of the standard approach, it also includes a similar quality of rear surface passivation by use of a "floating" rear junction. On good quality material, it should eventually be possible to demonstrate similar performance to laboratory PERL cells. On poorer quality material, thinner substrates are required to take advantage of the improved rear passivation. This is fortunate since there is a trend to thinner substrates purely on economic grounds (more efficient material utilization). Large area (10 cm x 10 cm) substrates as thin as 180 μm have been used in low-cost production [11.28].

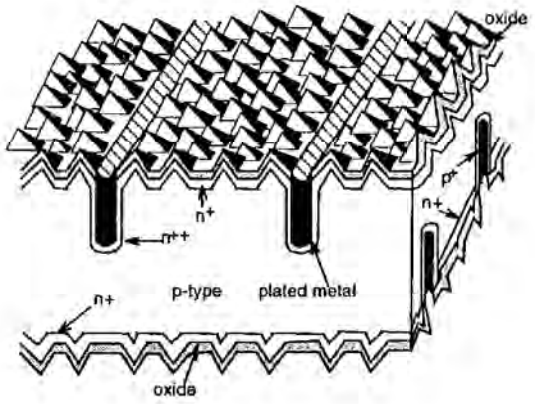


Figure 11.6: Double-sided or bifacial buried contact solar cell.

A useful approach for analyzing multiple junction cells such as the present is to use the modified Ebers-Moll equivalent circuit [11.29] of Fig. 11.7. This circuit is widely used in microelectronic device analysis but requires modification by the addition of the photogeneration

current sources shown.

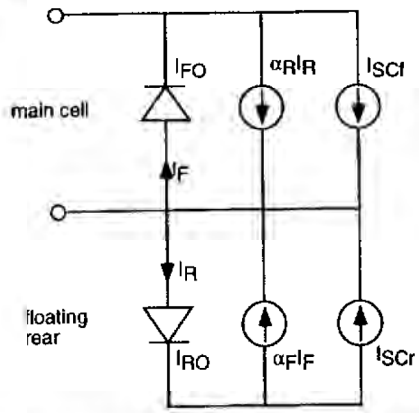


Figure 11.7: Ebers-Moll equivalent circuit for a floating junction solar cell.

The value of the saturation current density of the junction diodes and the photogeneration sources are those calculated (or experimentally determined) with the other junctions short-circuited. The injection terms, α_F and α_R, are the respective proportions of the total current flowing across the junctions which reach the other junction as minority carrier current. For example, for a simple one dimensional case with the two junctions separated by a distance, W, α is given by:

$$\alpha = \frac{I_{bo}}{I_{eo} + I_{bo}} \frac{1}{\cosh (W/L)} \qquad (11.1)$$

where I_{eo} and I_{bo} are the emitter and base components of the junction saturation current (with the other junction short-circuited) and L is the diffusion length.

Analysis of this equivalent circuit for the floating junction case gives the cell saturation current as:

$$I_O = I_{FO} (1 - \alpha_R \alpha_F) \qquad (11.2)$$

When α_F and α_R approach unity, I_O is much smaller than I_{FO}, which is

the value corresponding to infinite rear surface recombination velocity. The cell short circuit current density is given by:

$$I_{SC} = I_{SCf} + \alpha_R I_{SCr} \qquad (11.3)$$

This is always higher than that available with infinite rear recombination velocity and approaches the maximum possible from the cell as α_R approaches unity.

Extending this analysis shows that the rear floating junction is more sensitive to shunting effects than the top junction [11.30]. Additional components of I_{RO} are introduced by current flow laterally from the floating layer to the p^+ grooves. These act to decrease α_R by introducing another component into the denominator of Eq. (11.1). However, these problems would appear solvable.

Solving them would turn the liability of the "wrap-around" of dopant to the rear during the initial top junction diffusion into a surface passivation asset. Alternatively, rear surface passivation could be achieved more conventionally by an additional p^+ diffusion. Whatever the final approach implemented, the double-sided buried contact cell offers the real possibility of producing large area cells of efficiency above 20% upon thin, moderate quality wafers.

REFERENCES

11.1 Final Report, Flat Plate Solar Array Project, Jet Propulsion Laboratory, E. Christensen (ed.,), October, 1985.

11.2 E.L. Ralph, "Recent Advancements in Low Cost Solar Cell Processing", Conf. Proceedings, 11th IEEE Photovoltaic Specialists Conference, Scottsdale, 1975, p. 315-316

11.3 Final Report, Flat Plate Solar Array Project, Vol. X, Jet Propulsion Laboratory, Publication 86-31, pp. 5101-5289, October, 1986.

11.4 C.M. Chong, S.R. Wenham and M.A. Green, "High Efficiency Laser Grooved, Buried Contact Solar Cell", Appl. Phys. Lett., Vol. 52, pp. 107-109, 1988.

11.5 M.A. Green and S.R. Wenham, "Silicon Cells: Single Junction, One Sun, Terrestrial, Single- & Multi-Crystalline", in *Solar Cells and Their Applications*, L. Partain (ed.), (Wiley, New York, 1995).

11.6 Final Report, Flat Plate Solar Array Project, Vol. V, Jet Propulsion Laboratory, Publication 86-31, October, 1986.

11.7 R. Mertens, "Silicon Solar Cells", 12th European Photovoltaic Solar Energy Conf., Amsterdam, 1994, pp. 1-6.

11.8 R.R. King, K.W. Mitchell and J.M. Gee, "Back Surface Cell Structures for Reducing Recombination in CZ Silicon Solar Cells", Conf. Record, 1st World Conf. on Photovoltaic Energy Conversion, Hawaii, Dec., 1994.

11.9 S.R. Wenham, M.R. Willison, S. Narayanan and M.A. Green, "Efficiency Improvement in Screen Printed Polycrystalline Silicon Solar Cells by Plasma Treatments", 18th IEEE Photovoltaic Specialists Conf., Las Vegas, Oct., 1985, p. 1008.

11.10 J. Szlufcik, H.E. Elgamel, M. Ghannam, J. Nijs and R. Mertens, "Simple Integral Screenprinting Process for Selective Emitter Polycrystalline Silicon Solar Cells", Appl. Phys. Lett., Vol. 59, pp. 1583-1584, 1991.

11.11 N. Mardesich, "Solar Cell Efficiency Enhancement by Junction Etching and Conductive AR Coating Processes, Conf. Record, 15th IEEE Photovoltaic Specialists Conf., Kissimmee, May, 1981, pp. 446-449

11.12 S.R. Wenham, "Buried-Contact Silicon Solar Cells", Progress in Photovoltaics, Vol. 1, pp. 3-10, 1993.

11.13 T.M. Bruton, A. Mitchell and L. Teale, "Maximizing Minority Carrier Lifetime in High Efficiency Screen Printed Silicon BSF Cells", Conf. Proceedings, 10th E.C. Photovoltaic Solar Energy Conference, Lisbon, April, 1991, pp. 667-669.

11.14 T.M. Bruton, N.B. Mason and J.G. Summers, "Towards Production of High Efficiency Terrestrial Solar Cells", Conf. Proc., 6th International Photovoltaic Science and Engineering Conference, New Delhi, February, 1992, pp. 21-24.

11.15 From data sheet, BP Saturn Solar Cells, 1991.

11.16 C.B. Honsberg, F. Yun, A. Ebong, M. Taouk, S.R. Wenham and M.A. Green, "685 mV Open Circuit Voltage Laser Grooved Silicon Solar Cell", Solar Energy Materials and Solar Cells, Vol. 34, pp. 117-124, 1994.

11.17 B.O. Chan, "Defects in Silicon Solar Cell Materials", PhD Thesis, University of New South Wales, 1993.

11.18 B.L. Sopori, L. Jastrzebski, T.Y. Tan and S. Narayanan, "Gettering Effects in Polycrystalline Silicon", Conf. Proceedings, 12th European Photovoltaic Solar Energy Conference, Amsterdam, April, 1994, pp. 1003-1006.

Conference, Las Vegas, 1985, pp. 604-610.

12.25 R.M. Swanson, S.K. Beckwith, R.A. Crane, W.D. Eades, Y.K. Kwark, R.A. Sinton and S.E. Swirhun, "Point Contact Silicon Solar Cell", IEEE Trans. Electron Devices, Vol. ED-31, pp. 661-664, 1984.

12.26 P.J. Verlinden, R.M. Swanson, R.A. Sinton, R.A. Crane, C. Tilford, J. Perkins and K. Garrison, "High-Efficiency, Point-Contact Silicon Solar Cells for Fresnel Lens Concentrator Modules", Conf. Record, 23rd IEEE Photovoltaic Specialists Conf., Louisville, May, 1993, pp. 58-64.

12.27 C.L. Tilford, R.A. Sinton, R.M.Swanson, R.A. Crane and P. Verlinden, "Development of a 10 kW Reflective Dish PV System, Conf. Record, 23rd IEEE Photovoltaic Specialists Conf., Louisville, May, 1993, pp. 1222-1227.

Chapter
13

MULTICRYSTALLINE AND RIBBON SILICON

13.1 INTRODUCTION

For non-concentrating solar cells, cell efficiency is a very important parameter, but high efficiency must be obtained at low cost. A major contributor to the cost of crystalline silicon solar cell modules is the cost of the cell substrate. Several different approaches have been developed in attempts to reduce the substrate cost.

The first to be used commercially was an approach based upon multicrystalline ingots. Slow solidification in an appropriate mould results in ingots with large columnar grains [13.1, 13.2]. The grains in a sliced wafer have to be at least 1 mm in diameter on average to obtain a reasonable cell efficiency using established techniques. The term "multicrystalline" is used to distinguish such large grain material from the finer grain "polycrystalline" material of Chapter 14 [13.3].

A second type of approach to the lowering of substrate costs is to solidify molten silicon directly in large area sheet form using one of several ribbon growth processes. The edge-defined film-fed growth method [13.4] was the first to be used commercially. In its present

form, ribbons are grown in the form of a hollow, flat-sided tube, as shown in Fig. 13.1. Substrates are then cut from the faces of the tube. Another ribbon approach which has reached an advanced stage of development is the dendritic web approach [13.5]. A good review of these and other ribbon approaches is given elsewhere [13.6].

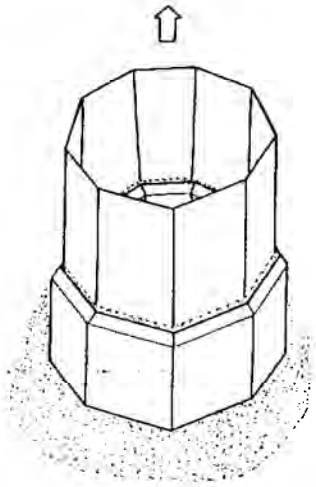


Figure 13.1: Growth of a nonagonal ribbon of silicon using the edge-defined film-fed growth (EFG) method [13.4].

These potentially low cost approaches invariably produce material of poorer crystallographic quality than does the normal Czochralski process used in microelectronics. Most of them produce multicrystalline material. Additionally, there is more scope for impurity incorporation during growth. As a result, the energy conversion efficiency of cells fabricated on such substrates is invariably lower than that which can be obtained on Czochralski substrates.

From the point of view of cell fabrication, the most important differences arise from: (i) the presence of grain boundaries which can act as very efficient recombination sites for minority carriers as discussed in more detail in Chapter 14; (ii) the presence of less severe crystallographic defects such as dislocations and twinning planes in the intragrain region as well as impurities in these regions which often decorate the crystallographic defects and render them more active

electronically; and (iii) the lack of a simple technique for texturing cell surfaces since only small fractions of the areas of these surfaces are of the (100) orientation required for the anisotropic etching approach to be effective. These differences restrict cell efficiencies to about 80% of those obtained with Czochralski material. Differences at the module level tend to be smaller due to the higher packing density arising from the ease with which square or rectangular substrates are produced.

13.2 HYDROGEN PASSIVATION

A technique generally accepted to be of benefit in improving the performance of a wide range of low cost silicon substrate materials is that based upon the passivation of defects by atomic hydrogen [13.7].

Atomic hydrogen is relatively mobile in silicon, even at low temperatures, and is particularly so at dislocations and grain boundaries [13.8,13.9]. During its diffusion through bulk and grain regions, the atomic hydrogen neutralizes a large fraction of the electronically active defects which it encounters. Techniques for introducing hydrogen include exposure to plasma discharges in a hydrogen-rich ambient and exposure to hydrogen ion beams [13.7].

There is general agreement that the hydrogenation process is more effective the poorer the quality of the starting material [13.7]. As a consequence, hydrogenation serves to lighten the production yield of cells fabricated on low cost substrates, rather than increasing the performance of the best cells. The most significant improvements from hydrogenation generally occur in the short-circuit current of the cell, with smaller improvements generally seen in the open-circuit voltage [13.10-13.13]. The fill factor behaviour is less predictable.

Two examples of how hydrogenation can be incorporated into cell fabrication sequences will now be described. In the first sequence [13.14], hydrogenation occurs during plasma deposition of a silicon nitride AR coating in a hydrogen-rich ambient. This occurs at an intermediate state of cell processing prior to metallization. The hydrogen is apparently trapped in the cell during subsequent high temperature processing steps by surface layers. In the second sequence [13.15,13.16], hydrogen is implanted using a hydrogen ion beam later in the processing sequence, after metallization. With this sequence, a marked increase in the performance of cells fabricated on the EFG ribbon of Fig. 13.1 was obtained. The median efficiency of

cells fabricated on 50 cm^2 substrates using this approach was reported to increase from 11.3 to 13.0% as a result of such treatment.

A final question concerns the stability of the hydrogenation treatment, in view of the low temperatures at which the treatment is used. The results obtained to date [13.15] indicate that it is many orders of magnitude more stable than a comparable hydrogenation process in thin film amorphous silicon solar cells.

13.3 PHOSPHORUS TREATMENT

Phosphorus diffusion is one of the more established gettering processes discussed in Chapter 9. Such processes are likely to be particularly important in less expensive substrate materials, due to the higher impurity concentrations. Additionally, diffusion at grain boundaries and dislocations occurs at a much higher rate than in bulk regions, as indicated in Fig. 13.2. Therefore, phosphorus diffusion can convert such defects from liabilities, due to the associated high recombination rates, to assets, due to the vertical junction type of action arising from the extension of the collecting junction into the substrate bulk as shown in Fig. 13.2. This is a more positive effect than that of hydrogenation, which merely neutralizes such defects.

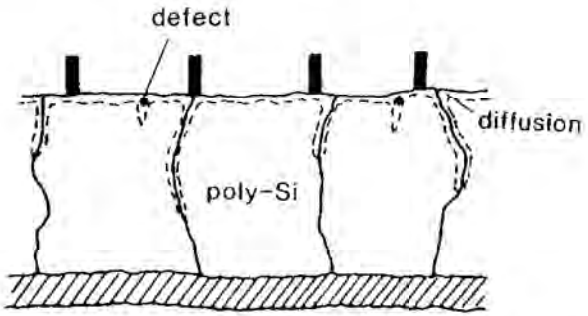


Figure 13.2: Cross-section of a multicrystalline silicon solar cell showing preferential diffusion of dopants down the grain boundaries and at crystallographic defects.

Two-step diffusion processes have shown the gains possible from this approach. Prolonged low temperature diffusion is used to dope the grain boundaries followed by the normal junction diffusion [13.17]. In

our laboratory, a different approach has been developed. This is based upon combining a single heavy diffusion with a subsequent etching step which removes most of the diffused layer, together with gettered impurities.

Figures 13.3(a) and (b) show some particularly interesting results in this area [13.18]. The dashed lines show the performance of cells fabricated using a standard screen-printing sequence [13.19] on nominally 5 Ω cm multicrystalline substrates. The variable is the sheet resistivity of the phosphorus layer diffused into the p-type substrate.

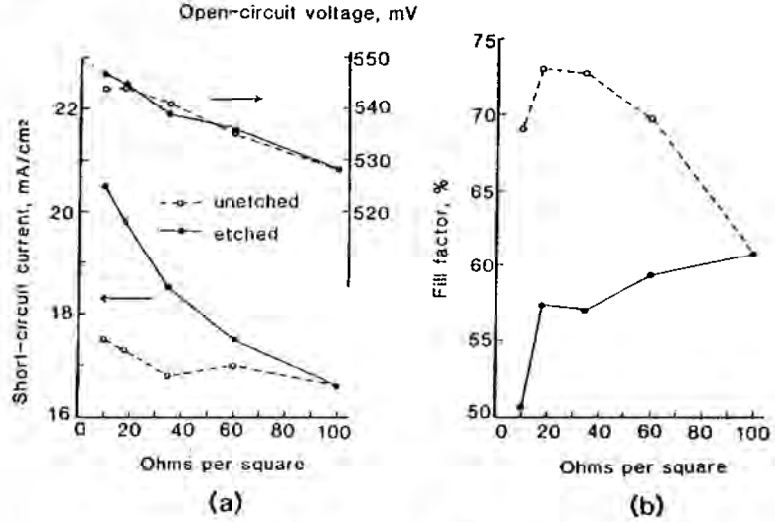


Figure 13.3: Effect of etching after diffusion upon the characteristics of multicrystalline cells. The dashed lines show the cell performance without etching, while the solid curves show the effect of etching to a sheet resistivity of 100 Ω/square after diffusion (after Wenham [13.18]).

An important feature of the set of results shown by the dashed lines is the peak in the fill factor obtained for sheet resistivities of around 30 Ω/square. At higher sheet resistivities, the fill factor is lower due to an increased contact resistance between the screened silver top contact and the increasingly more lightly doped diffused layer. At lower sheet resistivities, the loss in fill factor is attributed to a shunting effect due to the phosphorus dopant diffusing through to the rear contact at an

increasing number of grain boundaries.

Another feature is the much higher open-circuit voltage obtained at low sheet resistivity values. This is attributed to a higher effective bulk lifetime, as discussed later. The short-circuit current density is low, due to the lack of an AR coating and to a high (12%) top contact shading loss, but is relatively insensitive to the top layer sheet resistivity. This is a surprising result. For crystalline cells, this current would fall markedly at low sheet resistivity, due to a "dead layer" along the cell surface which decreases the blue response. In the present devices, this detrimental effect is more than offset by the favourable effects of the diffusion upon red response. These include its effect upon the effective bulk lifetime, via its gettering action, as well as the defect passivation and vertical junction effects of Fig. 13.2.

To demonstrate this more convincingly, the surface was chemically etched back to a uniform sheet resistivity of 100 Ω/square, prior to applying the top contact, for samples diffused over the same range as before. The results are shown by the solid lines in Fig. 13.3. The short-circuit current density was found to increase by more than 20% at lower sheet resistivities. This is due to the increased ***blue*** response as a result of the removal of the "dead layer". The similar advantage over substrates diffused directly to 100 Ω/square is due to an increased ***red*** response. A small increase in the open-circuit voltage was generally observed as a result of this treatment, as was a marked decrease in fill factor due to the increased contact resistance.

The effects of phosphorus pre-treatment have also been explored by applying the high efficiency PESC sequence of Chapter 10 to multicrystalline wafers [13.20].

The open circles in Fig. 13.4 show the experimental results obtained by applying the PESC sequence directly to multicrystalline substrates with resistivities in the 0.1-1 Ω cm range, all from the same supplier. Creditable efficiencies of between 15.0-15.5% were obtained over the whole range. The lower resistivity substrates gave a higher open-circuit voltage, with values above 630 mV being obtained at the lower end of the range. The short-circuit current showed the opposite dependence upon resistivity, due to a decrease in diffusion length as the resistivity decreased. The former decreased from 125 to 45 μm as the resistivity decreased from 1 Ω cm to 0.1 Ω cm [13.20]. The closed circles show the effect of the phosphorus pre-treatment.

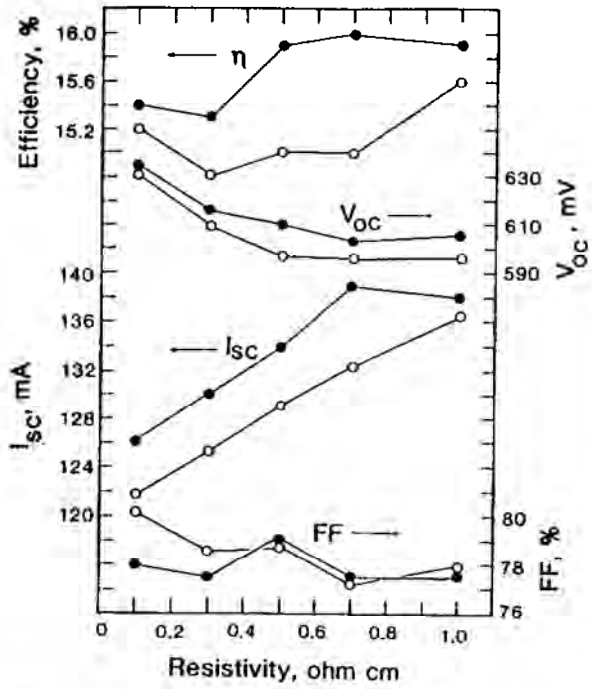


Figure 13.4: Effect of phosphorus pre-treatment upon the performance of cells fabricated on multicrystalline silicon (nominal cell area: 4.06 cm^2). The open circles show the results for cells fabricated with a standard PESC sequence, while the closed circles show the benefits of heavy phosphorus diffusion followed by a chemical etch-back [13.20].

After using a chemical etch to remove saw damage, these substrates were heavily diffused with phosphorus at 900°C to give sheet resistivities within the range of 20-50 Ω/square. Using a weak silicon etch, the surface of the diffused region was etched until the sheet resistivity increased to the 100-150 Ω/square range, standard for the PESC sequence. The cells were then processed in the normal way for this sequence [13.20].

This treatment produced a very consistent increase in open-circuit voltage, short-circuit current, and efficiency, as is apparent upon

comparing the closed and open circles of Fig. 13.4. There was more scatter in the fill factor, attributed to the simple "laser scribe and cleave" method used for edge junction isolation. This isolation approach has been found to introduce an extra recombination component into the cell characteristics [13.21]. The improvements in the other parameters were correlated with an improved effective diffusion length in the completed cells, which increased by up to 50% for cells in the intermediate resistivity range which showed the largest efficiency increase. The increase in the effective diffusion length is attributed to the gettering action of the phosphorus diffusion, combined with the passivation of crystallographically poor regions of the substrate by preferential diffusion in these areas.

The highest diffusion length reported after this treatment was 145 μm [13.20]. This is lower than that obtained in Czochralski grown substrates where post-processing values about twice this magnitude can be routinely obtained, even on the lower grades of commercial material. Whereas it is possible for diffusion lengths to be comparable to the substrate thickness of Czochralski material, this is not likely for the lower cost wafering approaches. This suggests that different cell designs might be appropriate in the latter case, as discussed in more detail in Section 13.6.

Applying the phosphorus etch-back/PESC technique to wafers from a different supplier subsequently gave efficiencies above 17% [13.22]. More recently, the same approach has given efficiencies approaching 18% for small area devices [13.23], the best to date for multicrystalline or ribbon substrates. By comparing to the 24% figure obtained on crystalline substrates, it is noted that the highest performance obtained to date using low cost ribbon and multicrystalline substrates is only 75% of that obtained using the highest quality silicon available.

Most of this short-fall can be attributed to the smaller diffusion lengths in this material, as previously mentioned. A sizeable amount can also be attributed to the inability to date to take advantage of the benefits of surface texturing in the best performance devices. Not only does such texturing reduce reflection, it also provides an effective diffusion length enhancement due to the way in which it obliquely couples light into the cell. Such an enhancement is particularly beneficial for short diffusion length material. This is discussed in more detail in Section 13.5.

13.4 OTHER PASSIVATION APPROACHES

Other approaches which have shown some potential for passivating defects in multicrystalline material include treatment with aluminium [13.24], lithium [13.25], and copper [13.26].

A rear aluminium alloying step forms part of the normal PESC processing sequence used in both sets of cells of Fig. 13.4. This indicates that the benefits of the phosphorus treatment may be complementary to those of aluminium treatment.

Subsequent work has specifically addressed this issue and shown this to be the case [13.27]. Not only is rear surface aluminium reported to have a gettering effect (Chapter 9), aluminium also acts as a p-type dopant in silicon and thus could preferentially dope the grains and thereby neutralize their electronic action.

Lithium is a fast diffuser in silicon and acts as an n-type dopant. Its beneficial effect in passivating radiation-induced defects in n-type substrates was the subject of a great deal of developmental activity in the late 1960's for space use. Its action in low cost substrates would be expected to be similar to that of phosphorus, except for its lower solubility and higher diffusivity. There are reports of instability in the beneficial effects of lithium in low cost substrates [13.7], probably due to the latter property. Copper is also a fast diffuser in silicon and is normally incorporated into silicon during high quality microelectronics processing, despite efforts to avoid this (Chapter 9). In crystalline cells, copper is one of the more benign impurities (Fig. 9.10), eventually degrading cell performance by precipitation in the junction depletion region. Its beneficial action may therefore arise from its ability to diffuse quickly through the silicon and reach relatively high concentration levels. This would be achieved without introducing undue detrimental effects and presumably some beneficial effects, due to the copper complexing with electronically active defects.

13.5 TEXTURING

In Section 13.3, a major contributor to the performance gap between the best single crystal cells and the best cells prepared on ribbon and multicrystalline substrates, was attributed to the inability to texture the latter using the normal approach. For multicrystalline substrates, only a fraction of the grains are close to the (100) orientation required

for the normal approach to be effective. For ribbon substrates, such as EFG ribbon and dendritic web, the natural orientation of the surface is (110) and (111) respectively, preventing normal texturing.

In the historical development of silicon cells outlined in Chapter 10, texturing accounted for the more than 10% relative performance advantage of black cells over violet cells. The performance margin for multicrystalline or ribbon cells with single layer antireflection coatings would be even larger, due to the shorter diffusion lengths in the latter case. This large margin makes the development of a texturing approach or its equivalent an important area of activity for such cells.

In the early development of multicrystalline cast ingots, seeding the ingot was used to encourage the grains to have the correct orientation [13.28]. A relative performance margin of 20% was reported for cells on such substrates [13.28], due mainly to the benefits of texturing. Clearly, this approach is not suitable for all ribbon and multicrystalline substrates, and innovative approaches are required.

A range of techniques based on chemical, plasma and mechanical texturing have been explored [13.28]. Mechanical texturing appears the most suitable for low cost, high throughput production, although special cutting tools need to be developed. Some very interesting devices have been proposed using such a mechanical approach [13.29]. High performance, large area laboratory cells of efficiency above 17% have also been fabricated using mechanical texturing [13.30].

13.6 ADVANCED CELL STRUCTURES

The best results for ribbon and multicrystalline substrates have employed largely the same cell design approaches as those used with crystalline silicon. However, the short diffusion lengths make some approaches more attractive than they would be on crystalline silicon.

One such structure is the double-sided cell of Fig. 13.5. This structure looks most promising for cells in which the carrier diffusion lengths are equal to about half the substrate thickness. Normally, the bottom half of such a cell would be ineffective for carrier collection. By having a second collecting junction over most of the rear surface, this loss can be largely avoided, making most of the cell volume active for carrier collection. There would be some loss in open-circuit voltage for short diffusion lengths, due to the increased junction area, although this loss

decreases once the diffusion length exceeds half the cell thickness. High performance, large area cells have been reported using this approach [13.31], although processing was undoubtedly too complicated for low cost production.

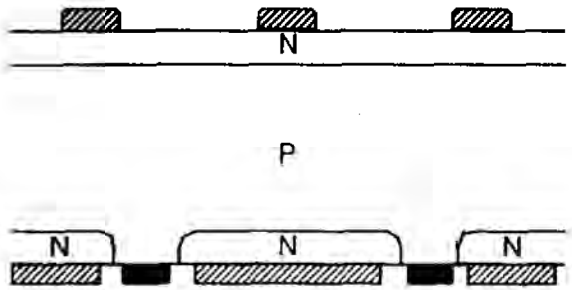


Figure 13.5: Schematic diagram of a double-sided cell structure particularly appropriate to intermediate quality material (carrier diffusion lengths equal to about half the substrate thickness).

The complication introduced by the third contact could be avoided by joining the two n-type regions through the substrate, as in the polka-dot cell of Fig. 12.8(b), also referred to as an "emitter-wrap-through" cell [13.32]. Unfortunately, it is probably not possible to use preferential diffusion down grain boundaries to provide this connection, since this may result in some grains being completely isolated from the p-type contact by being encased by an n-type diffusion. The buried contact approach has been applied to this structure to produce the mechanically or laser textured device of Fig. 13.6. The front and rear n-type grooves are sufficiently deep to overlap providing the connection between top and rear diffusions. A similar structure using overlapping textured features has also been described [13.29]. These approaches may prove too complicated for production.

A second structure, which is well suited to low diffusion length material, is the ***macrogrooved*** cell structure of Fig. 13.7 [13.18]. This structure has two strong points. One is that reflection can be kept low. The second is that, if the groove size is slightly larger than one minority carrier diffusion length, the whole volume of the groove region will have a high collection efficiency. A ray of light coupled into the cell can have a pathlength in this high collection region which is much larger than one diffusion length, as shown. In this regard, this structure performs better than the normally textured cell. Again, the increased junction

area can cause some loss in open-circuit voltage, although the effect upon short-circuit current more than compensates for this loss.

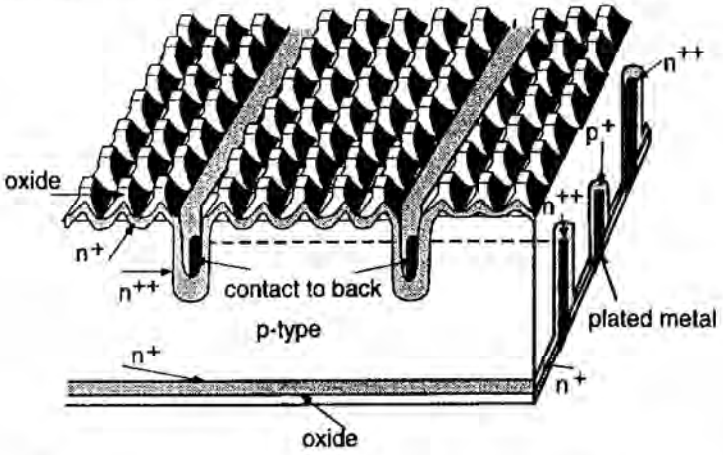


Figure 13.6: Emitter wrap through cell based on the buried contact approach. Both contacts are on the cell rear.

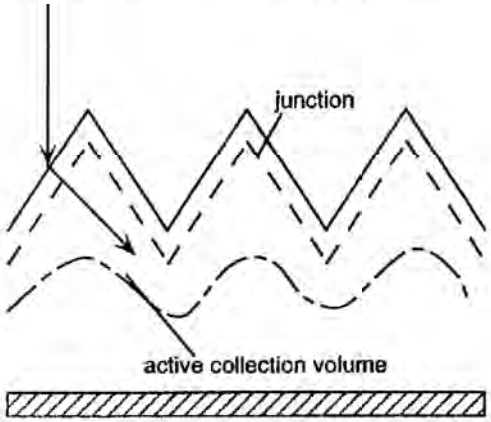


Figure 13.7: Macrogrooved cell structure which combines good reflection properties with the ability to steer light into the active collecting areas of the cell. By choosing an appropriate size for the geometrical features, this approach can significantly boost the performance of even very low quality material [13.18].

REFERENCES

13.1 H. Fisher and W. Pschunder, "Low Cost Solar Cells Based on Large Area Unconventional Silicon", Conf. Record, 12th IEEE Photovoltaic Specialists Conf., Baton Rouge, 1976, pp. 86-92; .H. Fischer and W. Pschunder, "Low Cost Solar Cells Based on Large-Area Unconventional Silicon", IEEE Trans. Electron Devices, Vol. ED-24, pp. 438-441, 1977.

13.2 J. Lindmayer and Z.C. Putney, "Semicrystalline Versus Single Crystalline Silicon", Conf. Record, 14th IEEE Photovoltaic Specialists Conference, San Diego, 1980, pp. 1096-1100.

13.3 B. Basore, "Short Communication: Defining Terms for Crystalline Silicon Solar Cells", Progress in Photovoltaics, Vol. 2, pp. 177-180, April, 1994.

13.4 F.V. Wald, "Crystal Growth of Silicon Ribbons for Terrestrial Solar Cells by the EFG Method", in "Crystals: Growth, Properties and Applications", Vol. 5, J. Grabmaier (ed.), Springer, Berlin, 1981, pp. 147-198.

13.5 C.S. Duncan, R.G. Seidensticker, J.P. McHugh, R.H. Hopkins, M.E. Skutch, J.M. Driggers and F.E. Hull, "Development of Processes for the Production of Low Cost Silicon Dendritic Web for Solar Cells", Conf. Record, 14th IEEE Photovoltaic Specialists Conference, San Diego, 1980, pp. 25-30.

13.6 T.F. Ciszek, "Techniques for the Crystal Growth of Silicon Ingots and Ribbon", J. Crystal Growth, Vol. 66, p. 655, 1984.

13.7 R.F. Van Overstraeten and R.P. Mertens, "Physics, Technology and Use of Photovoltaics", Adam Hilger, Bristol, 1986, p. 148.

13.8 S.J. Pearton, "The Properties of Hydrogen in Crystalline Silicon", Proc. 13th International Conf. on Defects in Semiconductors, Colorado, August, 1984, pp. 737-743.

13.9 D.S. Ginley and R.P. Hellmer, "Kinetic Modelling for Hydrogen Passivation of Polycrystalline Silicon", Journal of Applied Physics, Vol. 58, pp. 871-879, 1985.

13.10 W. Schmidt, K.D. Rasch and K. Roy, "Improved Efficiencies of Semiconductor and Metallurgical Grade Cast Silicon Solar Cells by Hydrogen Plasma Treatments", Conf. Record, 16th IEEE Photovoltaic Specialists Conf., San Diego, 1982, p. 537.

13.11 J.I. Hanoka, C.H. Seager, D.J. Sharp and J.K.G. Panitz, "Hydrogen Passivation of Defects in Silicon Ribbon Grown by the Edge-Defined Film-Fed Growth Process", Applied Physics Letters, Vol. 42, pp. 618-620, 1983.

13.12 Y.S. Tsuo and J.B. Milstein, "Hydrogen Passivation of Silicon

Sheet Solar Cells", Appl. Phys. Lett., Vol. 45, p. 971, 1984.

13.13 S.R. Wenham, M.R. Willison, S. Narayanan and M.A. Green, "Efficiency Improvement in Screen Printed Polycrystalline Silicon Solar Cells by Plasma Treatments", Conf. Record, 18th IEEE Photovoltaic Specialists Conf., Las Vegas, 1985, p. 1008.

13.14 K. Kimura, "Recent Developments in Polycrystalline Silicon Solar Cell", Technical Digest, 1st International Photovoltaic Science and Engineering Conf., Kobe, Nov., 1984, pp. 37-42.

13.15 K.V. Ravi, R.C. Gonstorawski and A.R. Chaudhuri, "Progress in EFG Technology for Low Cost Photovoltaics", 18th IEEE Photovoltaic Specialists Conf., Las Vegas, 1985, p. 1222.

13.16 J.E. Johnson, J.I. Hanoka and J.A. Gregory, "Continuous Mode Hydrogen Passivation", Conf. Record, 18th IEEE Photovoltaic Specialists Conf., Las Vegas, 1985, p. 1112.

13.17 F. Ferraris, F.C. Matacotta, S. Pidatella and L. Sardi, "Optimized Diffusion Parameters for Cells made by Columnar Silicon", Proceedings of 3rd International Photovoltaic Solar Energy Conference, Reidel, Dordrecht, 1980, pp. 625-629.

13.18 S.R. Wenham, "Laser Grooved Silicon Solar Cells", PhD Thesis, University of New South Wales, 1986.

13.19 R.B. Godfrey, S.R. Wenham, M.C. Pitt and C.L Kotila, "An Advanced Solar Cell Production Line Based on LSSA Funded Processes", Conf. Record, 16th IEEE Photovoltaic Specialists Conference, San Diego, 1982, pp. 892-894.

13.20 S. Narayanan, S.R. Wenham and M.A. Green, "High Efficiency Polycrystalline Silicon Solar Cells using Phosphorus Pretreatment", Appl. Phys. Lett., Vol. 48, pp. 873-875, 1986.

13.21 M.A. Green, A.W. Blakers and C. Osterwald, "Characterization of High Efficiency Silicon Solar Cells", J. Applied Physics, Vol. 58, pp. 4402-4408, 1985.

13.22 S. Narayanan, S.R. Wenham and M.A. Green, "17.8% Efficiency Polycrystalline Silicon Solar Cells", IEEE Trans. Electron Devices, Vol. ED-37, pp. 382-384, 1990.

13.23 A. Rohatgi, Z. Chen, G. Crotty, P. Sana and D.S. Ruby, "High Efficiency Multicrystalline Silicon Solar Cells", Proc., 1st European Int. Workshop on Crystalline Silicon Solar Cells, Spain, April, 1994.

13.24 R. Sandaresan, D.E. Burk and J.G. Fossum, "Potential Improvement of Polysilicon Solar Cells by Grain Boundary and Intragrain Diffusion of Aluminium", J. Applied Physics, Vol. 55, pp. 1162-1167, 1984.

13.25 G.L. Miller and W.A. Orr, Appl. Phys. Lett., Vol. 37, p. 100, 1980.

13.26 T. Daud and K.M. Koliwad, "Effect of Copper Impurity on Polycrystalline Silicon Solar Cells", Conf. Record, 13th IEEE Photovoltaic Specialists Conf., Washington, 1978, pp. 503-506.

13.27 I. Perichaud, F. Floret and S. Martinuzzi, "Limiting Factors of Phosphorus External Gettering Efficiency in Multicrystalline Silicon", Conf. Record, 23rd IEEE Photovoltaic Specialists Conf., Louisville, May, 1993, pp. 243-247

13.28 S. Narayanan, "High Efficiency Polycrystalline Silicon Solar Cells", PhD Thesis, University of New South Wales, May, 1989.

13.29 P. Fath and G. Willeke, "Mechanical Wafer Engineering for High Efficiency Polycrystalline Silicon Solar Cells", Conf. Record, 12th European Photovoltaic Solar Energy Conf., Amsterdam, April, 1994, pp. 1037-1040.

13.30 H. Nakaya, M. Nishida, Y. Takeda, S. Moriuchi, T. Tonegawa, T. Machida and T. Nunoi, "Polycrystalline Silicon Solar Cells with V-Groove Surface", Tech. Digest, International PVSEC-7, Nagoya, November, 1993, pp. 91-92.

13.31 T. Warabisako, K. Matsukuma, S. Kokunai, Y. Kida, T. Uematsu and H. Yagi, "Bifacial Multicrystalline Silicon Solar Cells", Conf. Record, 23rd IEEE Photovoltaic Specialists Conf., Louisville, May, 1993, pp. 248-251

13.32 J.M. Gee, M.E. Buck, W.K. Shubert and P.A. Basore, "Progress on the Emitter Wrap-Through Silicon Solar Cell", Conf. Record, 12th European Photovoltaic Solar Energy Conf., Amsterdam, April, 1994, pp. 743-748.